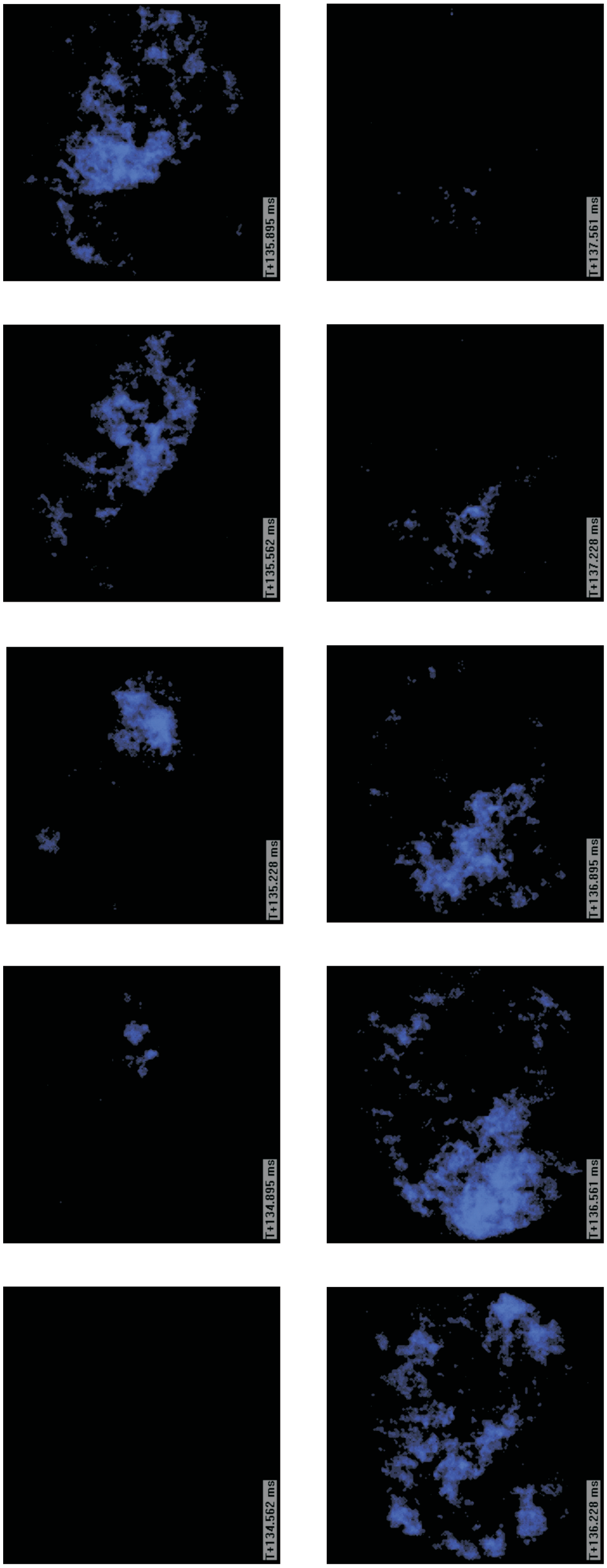

Figure 3.15: Image sequence for gasoline at $\phi = 0.37$.

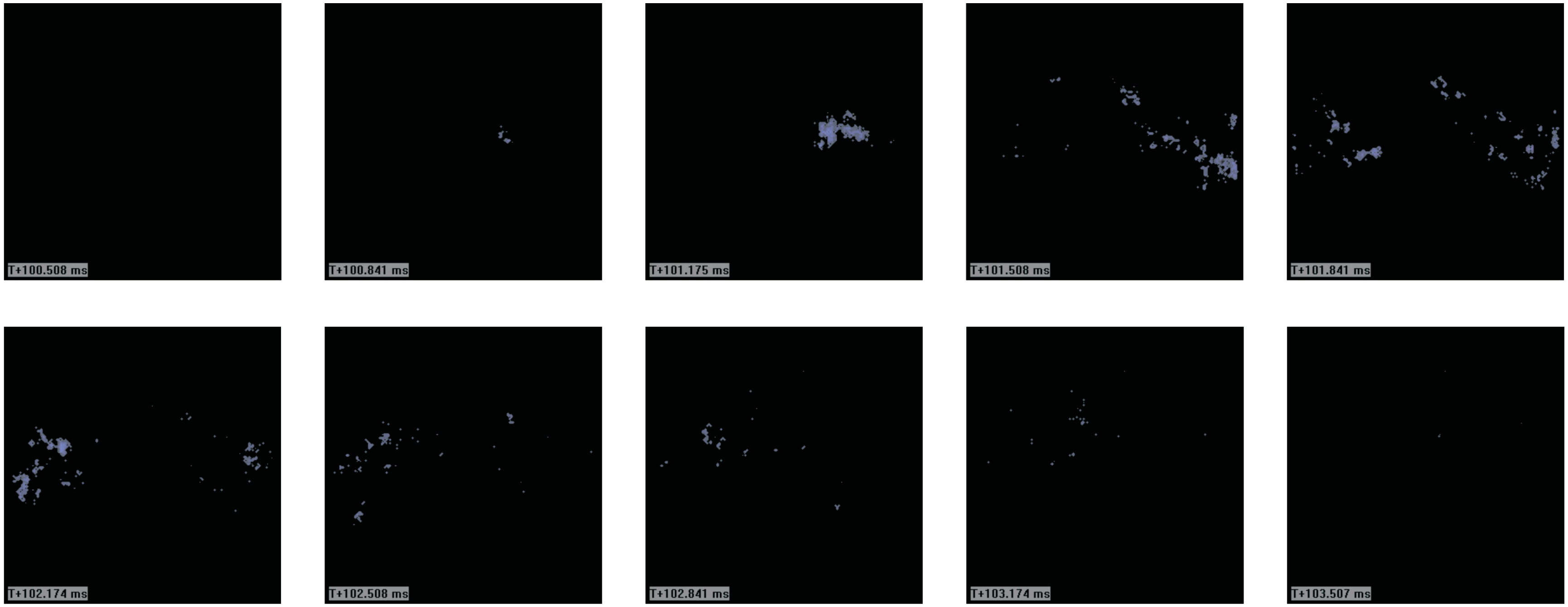

Figure 3.16: Image sequence for gasoline at $\phi = 0.27$.

473.7 nm, 516.5 nm, 563.5 nm; CH: 431.2 nm [24]). In numerous flame studies, CH is used to as a marker of the flame zone (e.g.[26, 27]). Consequently, the blue emission observed here is considered indicative of the combustion reaction front.

A separate series of experiments was conducted to determine if the white regions recorded in some of the imaging sequences were an indication of high-temperature radiation from soot or the result of sensor saturation. For these experiments, the engine was operated in HCCI mode with intake air preheated to approximately 320 °C with indolene at an equivalence ratio of $\phi = 0.69$. The engine exhibits strong, consistent HCCI combustion at these conditions. Axial image sequences were then acquired while increasing the frame rate and decreasing the exposure time. The following settings were used:

- 3000 fps, with 309 μs exposure
- 9000 fps, with 100 μs exposure
- 18000 fps, with 50 μs exposure

The resulting images (see Fig. 3.17) showed only blue emission for the faster frame rates and lower exposure times, indicating the white regions are due to sensor saturation from the high-intensity blue emission, not due to thermal emission from soot. Although such studies of the effects of the camera settings were not conducted for all fuels in this work, the engine operating conditions are sufficiently similar that we attribute the white regions observed in this work to sensor saturation, not soot.

In this study, gasoline supported the leanest stable HCCI operation (with net positive indicated mean effective pressure) and exhibited a gradual transition towards more spatially resolved, slower, weaker ignition behavior as the equivalence ratio was decreased. Indolene did not exhibit the same range of lean HCCI operation as gasoline, but followed the same general ignition behavior as mixtures became

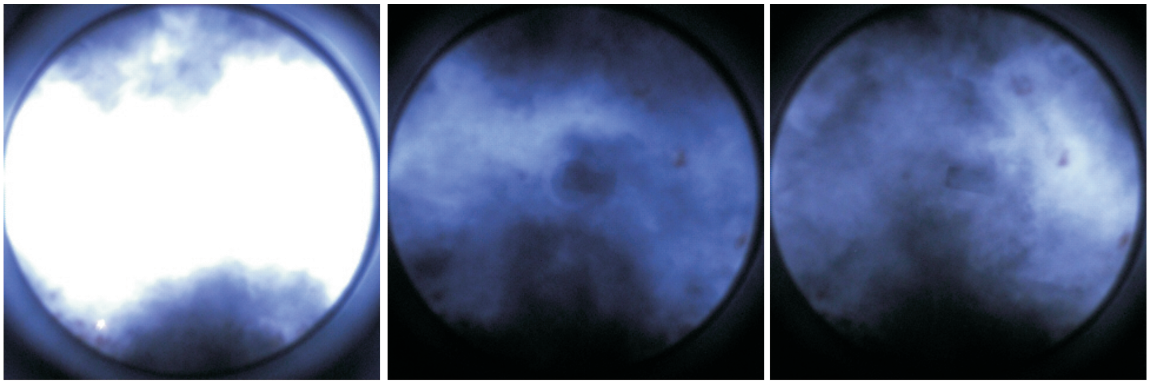

3000 fps **9000 fps** **18000 fps**

Figure 3.17: Images of separate, identical HCCI firing conditions (T_{int} = 320 °C, indolene fuel at $\phi = 0.69$) taken at peak cylinder pressure with camera speeds at 3000 fps, 9000 fps, and 18000 fps. All images have been color balanced equally for clarity.

leaner. Iso-octane did not support a stable transition through leaner mixtures. The ignition imaging for iso-octane at leaner mixtures show the ignition event to be much more spatially discretized (Figs. 3.8 - 3.10) than either indolene (Figs. 3.3 - 3.5) or gasoline (Figs. 3.13 - 3.16) for these equivalent air/fuel ratio conditions. Because lower equivalence ratios were not considered for indolene and gasoline in this study, it is not clear whether these fuels will also transition to discretized ignition as observed for iso-octane. Discretized ignition sites may be symptomatic of all of these fuels at lean, low-load limit HCCI conditions.

When comparing the results for the different fuels, it is important to consider the effects of changes in fueling on the in-cylinder charge temperature, as temperature is the single most important parameter controlling ignition. Although the intake air was always preheated to the same target temperature in the fuel studies, both the equivalence ratio and fuel type can impact the fuel/air charge temperature in a number of ways, including through changes in the ratio of specific heats of the fuel/air mixture and evaporative cooling of the intake air. The effects of the initial charge conditions on the end of compression temperatures were investigated in this work primarily through analytical studies. The results of these studies are presented in Figs. 3.18 - 3.20. Figure 3.18 presents the effects of changes the ratio of specific heats, γ, for iso-octane and two reference gasolines. Values for 100% air are included for comparison purposes. The effects of changing equivalence ratio are also considered in Fig. 3.18. As seen in the plot, the most significant impact on γ is due to the equivalence ratio of the mixture. Changes in the fuel properties have little effect on γ.

Figure 3.19 presents the end of compression (EOC) temperatures that result from isentropic compression of iso-octane and the two reference gasolines considered in Fig. 3.18. The EOC temperatures have been calculated for two equivalence ratios using the temperature-dependent values for γ presented in Fig. 3.18. Note the EOC temperatures vary by a virtually negligible amount for the three fuels for equivalent values of ϕ.

The effects of changes in the EOC pressure are presented in Figure 3.20. As expected, increasing EOC pressure increases the EOC temperature (by approximately 20 K for the pressure differential considered here of 2 bar). Note these data indicate how important accurate cylinder pressure data are for defining the initial charge conditions. Recall, that the intake pressure does not drift during the course of the experiments presented here, and that the intake manifold pressure is used to correct for any dynamic shift in the cylinder pressure transducer that occurs due to thermal drift (see Chapter II).

A primary conclusion of this analysis is that comparison of the HCCI data between fuels is not significantly convolved with changes in the fuel/air charge temperature for similar values of ϕ. However, comparisons within a data set for one fuel that vary in equivalence ratio should consider the changes induced in the thermal conditions of the mixture. In particular, the range of values for ϕ considered in this work ($\phi =$ 0.27 0.69), correspond to approximately a 40 K difference in EOC temperatures.

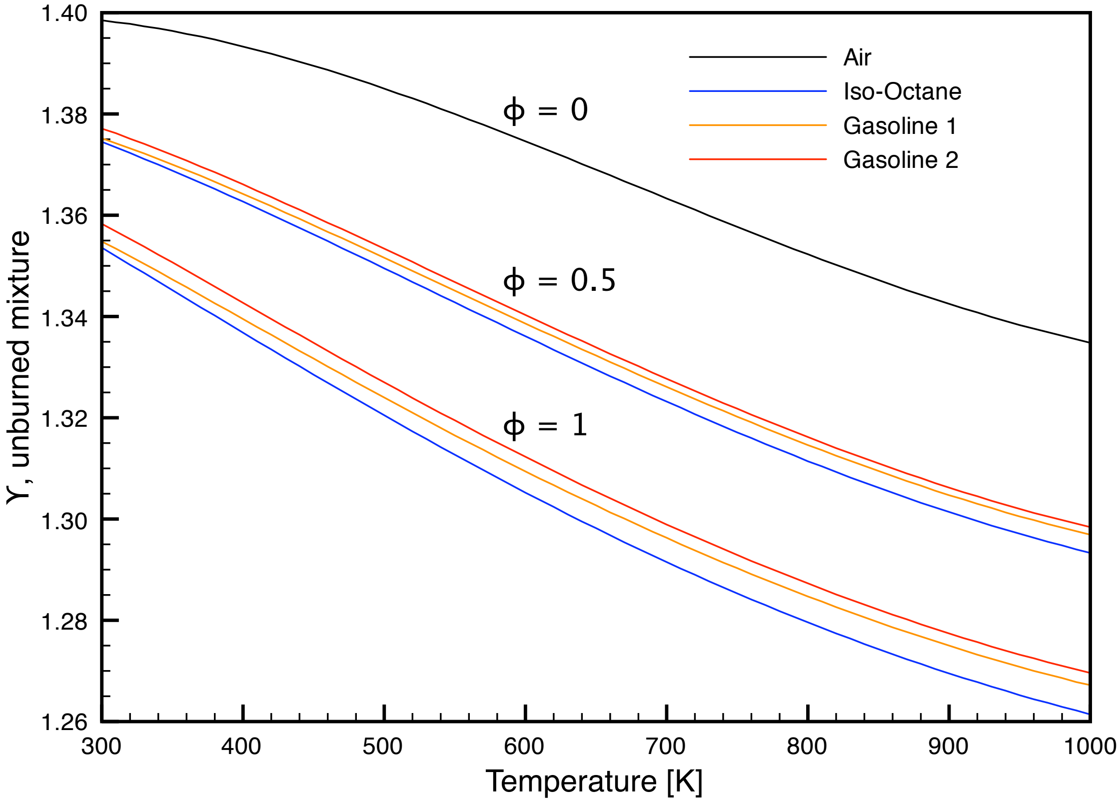

Figure 3.18: Ratio of specific heats, $\gamma_u = \frac{c_{p,u}}{c_{v,u}}$, for unburned mixtures of three fuels (iso-octane and two gasoline references) as a function of temperature and equivalence ratio.

The University of Michigan rapid compression facility has been used to extensively characterize the ignition delay time, τ, associated with numerous reference fuels, including iso-octane [33, 8]. The correlation developed by He et al. [33] for ignition delay time for iso-octane can be used as a basis for estimating the temperature in the cylinder at the start of compression. He et al. proposed the following expression for τ for iso-octane[33]:

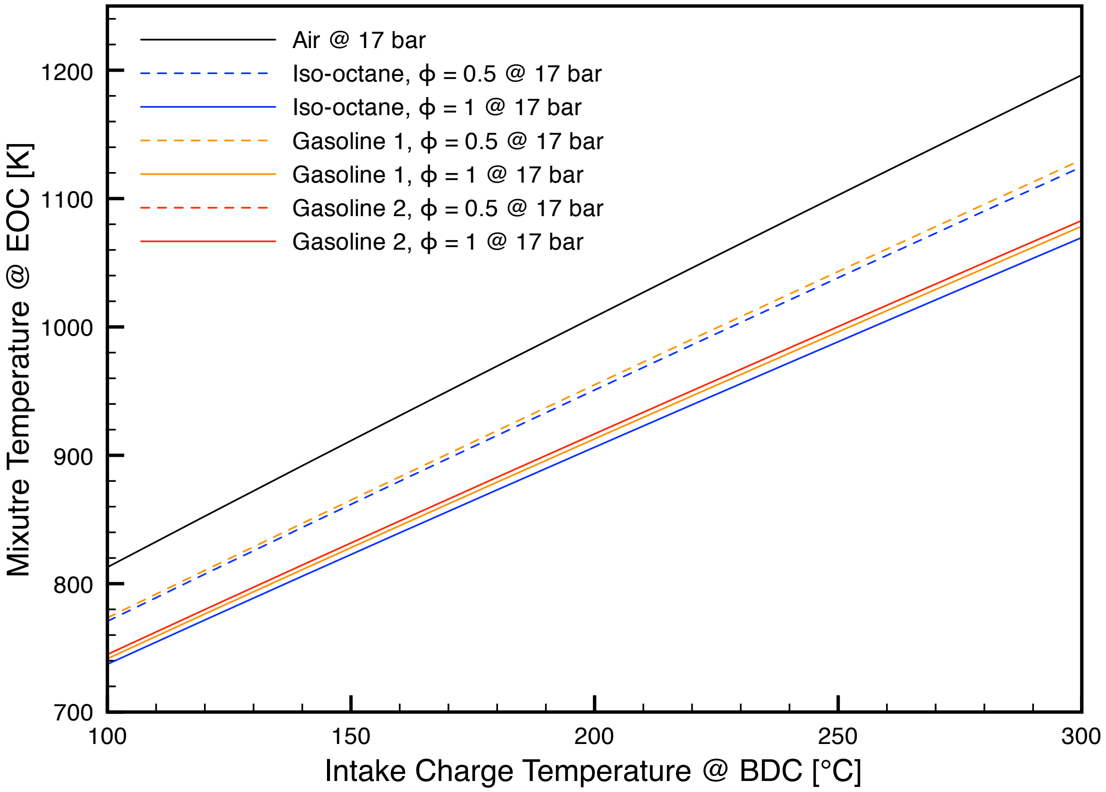

Figure 3.19: Calculated end of compression (EOC) temperatures for mixtures with iso-octane and two reference gasolines with EOC of 17 bar, given as a function of equivalence ratio and intake mixture temperature at Bottom-Dead-Center (BDC).

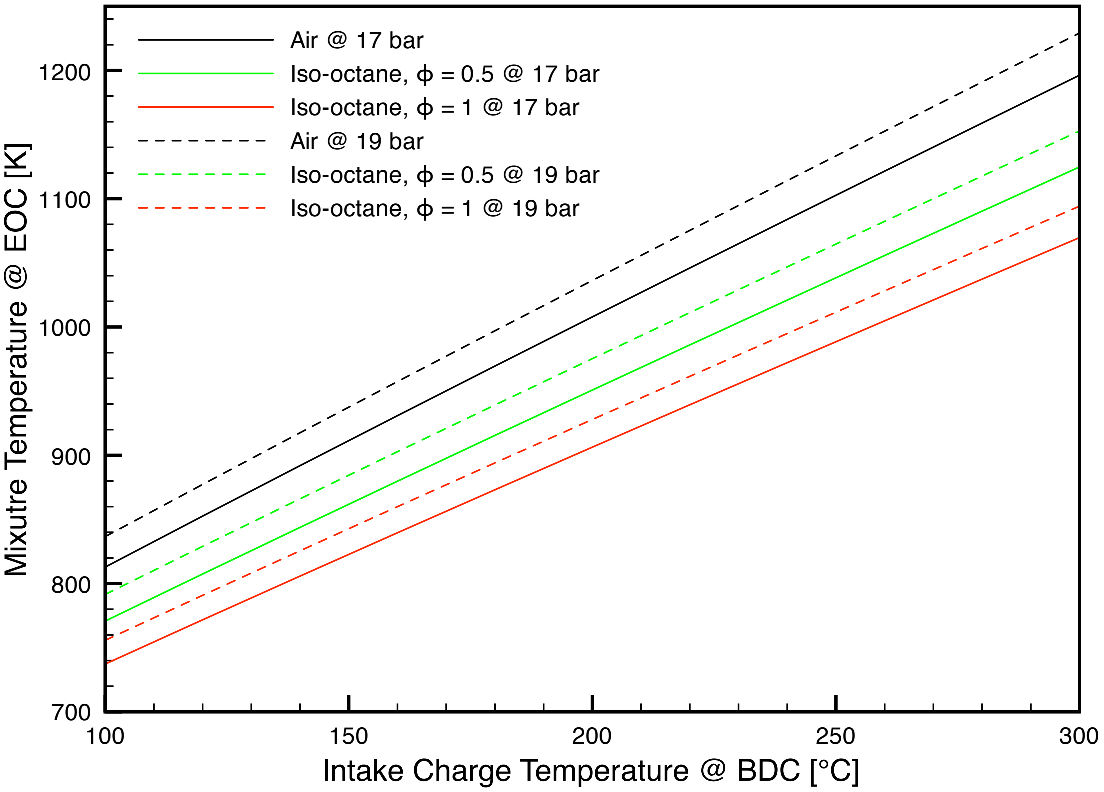

Figure 3.20: Calculated end of compression (EOC) temperatures for iso-octane mixtures for two different EOC pressures, given as a function of equivalence ratio and intake mixture temperature at Bottom-Dead-Center (BDC).

$$\tau_{ign} = 1.3x10^{-4}P^{-1.05}\phi^{-0.77}{\chi_{O2}}^{-1.41}exp(33700/R_{[cal/mol/K]}T) \tag{3.1}$$

where P is pressure [atm], T is temperature [K], ϕ is the equivalence ratio, χ_{O2} is the oxygen mole percent, and τ_{ign} is the ignition delay time [ms]. As noted earlier, the intake air temperature is measured upstream of the intake valves, before the fuel is injected. If the measured air temperature is considered the temperature at the start of compression (TSOC), then TSOC = 318 °C which can be used with pressure at start of compression (PSOC) = 1 atm. Assuming isentropic compression where γ is fixed at a value of 1.33 (from Fig. 3.18 for iso-octane with $\phi = 0.68$, T = 591 K) with a compression ratio of 10, the end of compression conditions are TEOC = 1264 K and PEOC = 21 atm. Using the end of compression temperature and pressure with Eqn. 3.1, with a reasonable estimate for the oxygen mole fraction (assuming negligible oxygen in the residual gases, then $\chi_{O2} = 21\%$), yields an ignition delay time of 60 μs (or 0.3 CAD at 700 rpm). This value for τ is clearly too fast and is unrealistic. Heat losses (e.g. due to convection to the intake manifold walls and due to evaporative cooling by the fuel) must significantly reduce the charge temperature below 318 °C. The imaging and pressure data for strong HCCI conditions can be used to make a coarse estimate of the cylinder charge temperature at the start of compression, TSOC. For example, if the ignition delay time is considered the time from departure of the HCCI pressure data from the motoring condition to the peak pressure for the conditions presented in Figs. 3.11 − 3.7, for iso-octane where $\phi = 0.68$, $\tau = 6$ CAD or 1.4 ms. Assuming the pressure at the start of compression is fixed at 1 atm (so PEOC = 21 atm), the isentropic compression relation for temperature and Eqn. 3.2 can be used to estimate TSOC, and a value of TSOC = 207 °C (corresponding to TEOC of 1027 K) is determined. Note this TSOC is a conservatively low estimate, as blow-by past the piston rings will reduce the effective compression ratio of the engine below 10.

A study was conducted to determine the spatial origin of ignition emission in-cylinder. Image sequences from multiple cycles (a minimum of 10 per fuel and equivalence ratio condition) were evaluated in terms of where ignition occurred. Approximately 150 image sequences were considered in total. Plotting these ignition sites revealed a pattern, which existed for all fuels and equivalence ratios studied, where ignition began approximately 50% of the time in a pair of zones located at the edges of the cylinders between the intake and exhaust valves, as shown in Fig. 3.21. The remaining ignition sites appeared randomly distributed. The preferential ignition zones likely indicate the existence of hotter regions within the combustion chamber. While the size, location, and strength of such a temperature gradient would depend on many engine-specific factors, all real engines would exhibit temperature gradients to some extent.

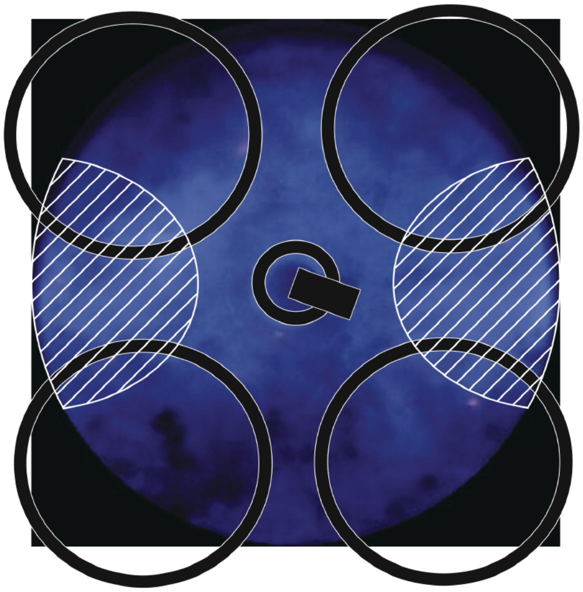

Figure 3.21: Image of cylinder end view showing area of preferential ignition sites as crosshatch.

Heat release data provide additional information on the ignition and combustion behavior of the fuels during HCCI operation. Since the heat release rate is difficult to measure, a net apparent heat release rate is defined from the experimentally measured pressure time histories and the piston displacement profile:

$$\frac{dQ_n}{dt} = \frac{\gamma}{\gamma - 1} p \frac{dV}{dt} + \frac{1}{\gamma - 1} V \frac{dp}{dt} \tag{3.2}$$

where Q_n is the net apparent heat release rate, p is the cylinder pressure, V is the cylinder volume and γ is the specific heat ratio. Equation 3.2 is taken from Heywood [31] in which $\gamma = 1.35$ was recommended as an appropriate value at the end of the compression stroke, and $\gamma = 1.26 - 1.3$ was recommended for the burned gas. In this study, $\gamma = 1.35$ was used. Apparent heat release for a moderate HCCI ignition event is shown in Fig. 3.22. Consistent with observations on HCCI in other imaging literature [34, 15, 35], peak chemiluminescence is coincident with peak heat release.

3.5 Summary and Conclusions

The results of this research study demonstrate that high-speed imaging provides direct time-resolved data on ignition and reaction phenomena important during HCCI operation of a single-cylinder research engine for a range of benchmarking fuels. HCCI combustion was initiated and maintained over a range of lean conditions for the three fuels considered, with equivalence ratios varying from $\phi = 0.69$ to 0.27. Air preheating was required to achieve ignition for the engine geometry and operating conditions considered.

The time-resolved imaging and pressure data clearly show that high heat release rates in HCCI combustion correlate to intense blue emission which occurs simultaneously throughout the volume of the combustion chamber. Lower rates of heat release

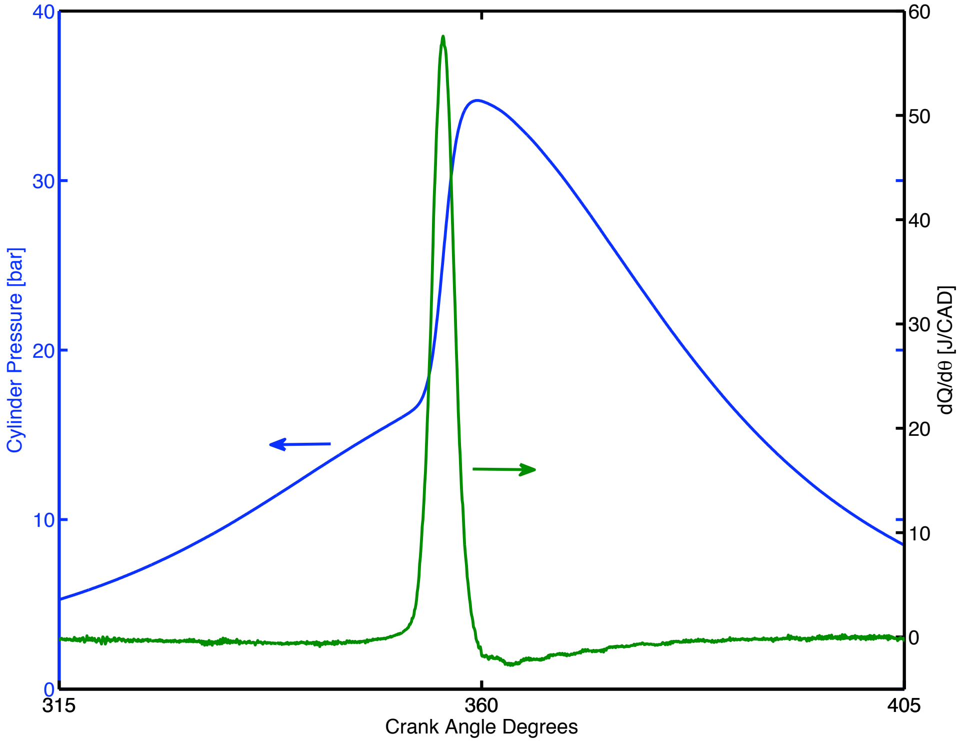

Figure 3.22: Cylinder pressure and corresponding apparent heat release rate for HCCI operating conditions with indolene fuel, T_{int} = 318 °C, $\phi = 0.57$.

are characteristic of blue emission that appears at local ignition sites over longer time intervals within the combustion chamber. It has been noted in the literature that at conditions close to misfire, there is a weaker relationship between chemiluminescence and heat release rate. The pump gasoline used supported leaner HCCI operation than indolene. Iso-octane showed a dramatic transition into misfire and exhibited many sparse ignition events at low equivalence ratios (dropping from 40 atm peak cylinder pressures at $\phi = 0.68$ to 18 atm peak cylinder pressures matching motoring engine conditions at $\phi = 0.61$). The results for iso-octane indicate misfire at low load has distinctly different ignition characteristics (with well resolved, localized ignition and propagation) compared to stable HCCI (with volumetric ignition). Ignition imaging suggests local hot zones result in preferential ignition sites for all of the fuels and equivalence ratios studied.

Indolene and gasoline reproduced similar ignition phenomena, whereas iso-octane was markedly different. This is somewhat unexpected as iso-octane is considered a chemical surrogate for gasoline and under HCCI conditions, where kinetics are rate limiting, more similarities in ignition behavior might be expected. This study also demonstrates the value of ignition imaging when applying HCCI or other low temperature combustion control strategies, as a means to identify flow field or thermal features, such as non-uniformities or hot spots, which can significantly augment or hinder ignition control and engine performance.

CHAPTER IV

Spark-Assisted HCCI

4.1 Introduction

The baseline performance of the single cylinder optical research engine was established and expected HCCI ignition and combustion behavior was discovered for a series of fuels in Chapter III. With this background, indolene fuel was selected for subsequent spark assisted HCCI studies presented in Chapter IV. Indolene exhibited HCCI ignition and combustion behavior similar to the pump gasoline, and is recognized as a standard reference fuel in metal research engine studies [36, 17] and full vehicle engine calibration.

The investigation of the effects of spark assisted HCCI operation spanned several studies. The initial study involved adding conservative timing of spark ignition assist at 5° Before-Top-Dead-Center (BTDC) to very lean, high temperature conditions with indolene [2, 37]. Another series of experiments were conducted using orthogonal imaging through the cylinder wall to further characterize the ignition event and reaction front propagation [38]. Based on the success of the earlier study, additional experiments were conducted to explore the effects of spark assist on HCCI operation over a wider range of operating conditions with indolene fuel. These studies spanned a range of intake air temperatures, equivalence ratios, and spark advance timing.

The imaging data provided valuable insight into the nature of the ignition event, in terms of combustion phasing, reaction front propagation, resulting heat release profiles, and indicated mean effective pressure (IMEP). Finally, a more expansive parametric study of intake air temperatures, equivalence ratios, and spark advance timing was conducted to further characterize the nature of and effectiveness of spark assist in expanding HCCI operation to low load, lean operating conditions.

The following sections present the results of the mult-axis imaging, the spark assisted HCCI parametric study of typical single cycle ignition phenomena, and the results of multi-cycle engine performance metrics. Portions of the material in this chapter have been published in the proceedings of the 2006 and 2007 Fall Technical Conferences of the ASME Internal Combustion Engine Division [39, 38].

4.2 Experimental Approach

All experiments were conducted using the optical engine facility located at the University of Michigan. A detailed description of the facility was presented in Chapter II. The same batch of reference indolene fuel was used for all spark assisted HCCI experiments (analyzed at 87.12% by weight carbon, <0.05% oxygen, 12.88% hydrogen; H/C = 1.762; 97.4 RON, 88.3 MON, 92.9 AKI). Fuel was injected at 172 kPa (Siemens DEKA II dual conical jet injector). Each experiment was preceded by motoring the engine at 700 RPM via the dynamometer while preheated air was inducted into the cylinder until the target steady state intake air temperature was reached.

HCCI operation was initiated with fuel delivery only, with equivalence ratio controlled by fuel injection pulse width. Spark ignition timing was controlled by dictating the ECM driver's falling edge cutoff of 13.8 volts to the primary side of the Wells C839 ignition coil. The collapse of the primary side of the ignition coil windings induces a high voltage potential across the secondary side of the coil. The secondary side of the coil drives a Motorcraft AYRF22PG spark plug, with a platinum tipped ground electrode gapped at 0.050 inches (Fig. 4.1).

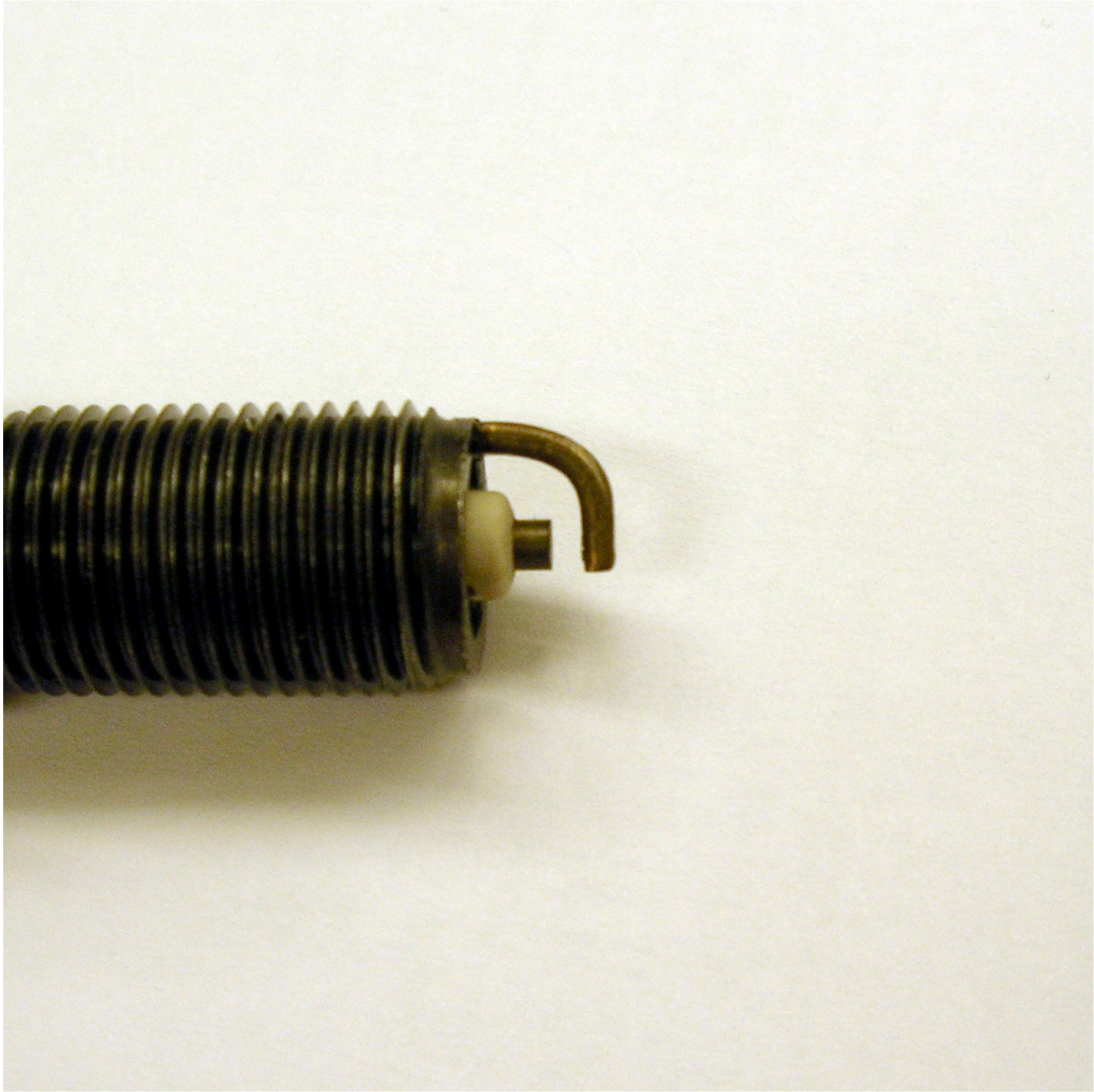

Figure 4.1: Spark plug electrode configuration.

Each experimental condition was typically performed in two stages:

- First, HCCI operation was initiated with fuel delivery only. No ignition spark was used to initiate firing and then transition to HCCI. After the engine fired in HCCI mode for approximately 5-10 seconds and the dynamometer stabilized the engine speed to 700 RPM, the data acquisition system was triggered to begin recording pressure and imaging data.
- After approximately 3-5 seconds of additional (recorded) HCCI operation, the ignition system was enabled to allow the engine to transition to spark assisted HCCI operation. Fuel delivery remained constant, and the dynamometer control system worked to maintain constant engine speed. Data was continually acquired during the transition and for another 3-5 seconds of spark assisted HCCI operation.

Pressure and imaging data were therefore collected for approximately 5-10 seconds of operation, capturing crank-angle resolved pressure and imaging data for about 30-60 consecutive firing cycles for each experiment. Each experiment was typically split about half HCCI / half spark assisted HCCI operation (see Figure 4.2). After each experiment, fuel and spark delivery were terminated. The dynamometer then held engine speed constant while the engine was continually fed preheated air. Imaging data required a download time of about 8 minutes between experiments, during which time the engine was allowed to return to steady state motoring conditions. Firing time periods were limited to a total of less than about 30 seconds to reduce thermal risk to the fused silica components. The engine was operated through the range of lean conditions listed in Table 4.1.

While most of the experiments were conducted with the camera configured to image through the piston window, a parallel investigative study was conducted with the camera set to record orthogonal imaging of the ignition and combustion event

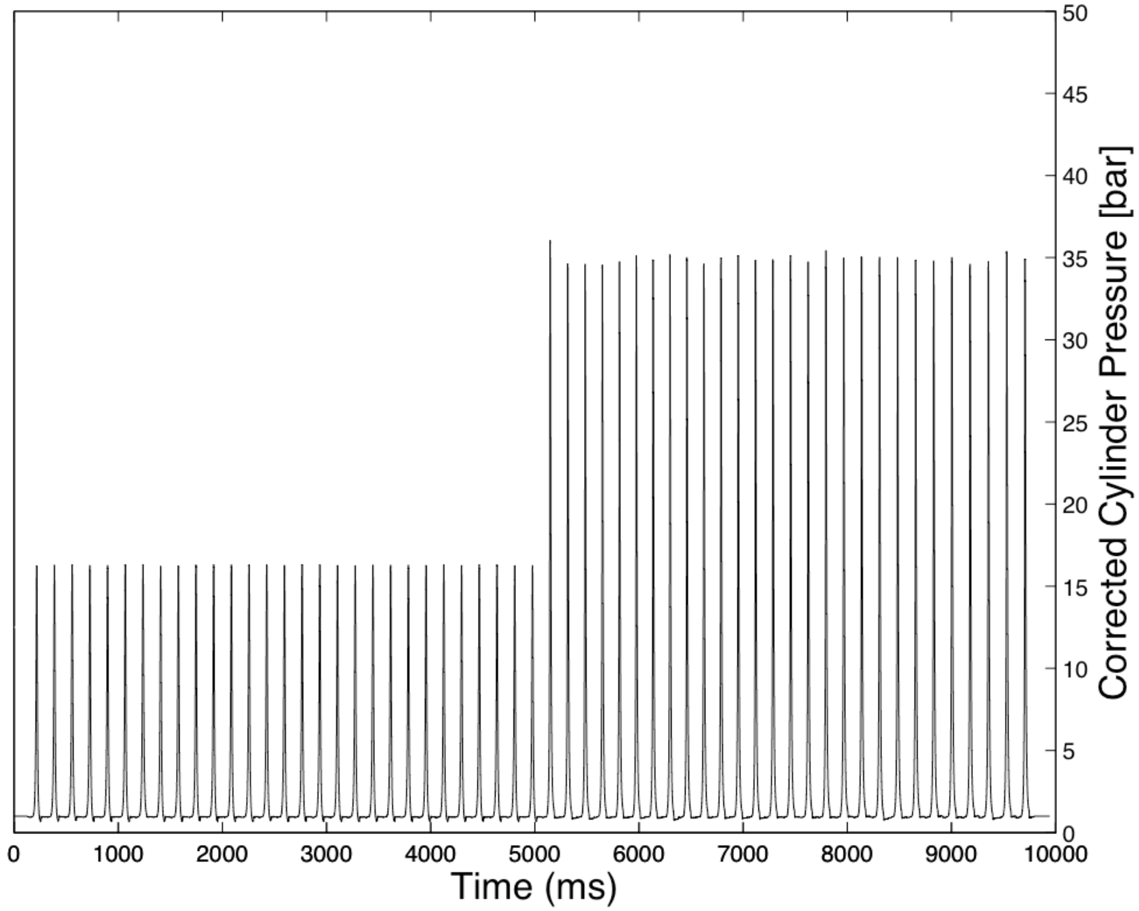

Figure 4.2: Corrected cylinder pressure for one experiment, showing the distinct transition when spark assist at 70 °BTDC is added to HCCI firing conditions at 5 seconds. Experimental conditions were $T_{int} = 271$ °C, $\phi = 0.62$ with indolene fuel.

Table 4.1: Experimental engine operating conditions studied in spark assisted HCCI mode. ”–” indicates HCCI operation and spark assist timing is noted in degrees Before-Top-Dead-Center (BTDC). All experiments in this table used indolene fuel. The ”Reference” column indicates where data from each experiment are presented in a figure.

Intake Air Temp. (°C)	ϕ	Spark Assist (°BTDC)	Imaging	Reference
271	0.56	–/ 20°	Piston View	
271	0.56	–/ 50°	Piston View	
271	0.56	–/ 70°	Piston View	
271	0.56	–/ 90°	Piston View	
271	0.52	–/ 20°	Piston View	Figure 4.16
270	0.62	–/ 20°	Piston View	Figure 4.18, 4.20
270	0.62	–/ 50°	Piston View	Figure 4.18, 4.19, 4.20
271	0.62	–/ 70°	Piston View	Figures 4.5, 4.2, 4.6, 4.8, 4.18, 4.20
271	0.62	–/ 90°	Piston View	Figure 4.18, 4.20
271	0.62	–	Side View	Figure 4.7
271	0.62	70°	Side View	Figure 4.9
281	0.56	–/ 20°	Piston View	
280	0.56	–/ 50°	Piston View	
281	0.56	–/ 70°	Piston View	
280	0.56	–/ 90°	Piston View	
281	0.47	–/ 20°	Piston View	Figures 4.11, 4.13, 4.14
271	0.45	–/ 10°	Piston View	
271	0.45	–/ 20°	Piston View	Figures 4.11, 4.13, 4.16, 4.12
271	0.45	–/ 30°	Piston View	
271	0.45	–/ 50°	Piston View	
271	0.45	–/ 70°	Piston View	
271	0.45	–/ 90°	Piston View	
256	0.46	–/ 20°	Piston View	Figures 4.11, 4.13
321	0.40	–/ 5°	Piston View	Figures 4.15, 4.17

[38]. This imaging study along the orthogonal axis to the piston was conducted with a similar experimental set-up and is depicted in the upper camera illustration in Figure 4.3. A shorter coolant-jacketed steel cylinder liner was used under a mating section of fused silica cylinder liner. The transparent portion of the cylinder allowed orthogonal viewing access from the cylinder head deck surface to 25 mm below the deck surface. Figure 4.4 depicts the orthogonal image view, as seen from the intake side of the cylinder. Another flat piston was also used with this engine configuration, with the piston ring pack lowered to prevent the piston rings from traversing the steel cylinder/fused silica cylinder transition. Although it was not used for imaging, the

piston held the same fused silica window to maintain similar piston heat transfer rates between experiments. The same color digital video camera was used as for the axial imaging with different C-mount extension tubes to adjust the focal length and depth. The camera was focused in a plane coinciding with the back side of the open intake valves, since the spark plug ground electrode is not visible (it protrudes to a depth 5 mm above the deck surface). The camera settings were fixed at 640 pixels wide x 480 pixels high at 3000 frames per second (fps) with 309 μs exposure time (the same frame rate and exposure as used in the piston view studies). The camera sensor array was calibrated according to the procedure outlined in Walton et al. [9].

4.3 Multi-Axis Imaging Results and Discussion

A series of experiments were conducted using orthogonal imaging through the cylinder wall to characterize the ignition event and reaction front propagation[38]. These experiments held intake conditions constant at T_{int} = 271 °C and $\phi = 0.62$. The experimental variable isolated in this study was the use of spark ignition. Prior experiments with this engine demonstrated that for these particular intake conditions, HCCI ignition is relatively weak (pressure traces show either no trace of heat release or very retarded, low heat release) [39]. Prior preliminary experiments with this engine also have also shown that for these particular intake conditions, the addition of spark-assist via the spark plug positively influences ignition. The fixed spark-assist timing of 70° BTDC was chosen for this study based on the earlier experiments which demonstrated this spark timing to have significant impact on charge ignition for these conditions.

Examples of typical pressure traces of HCCI and spark-assisted HCCI are shown in

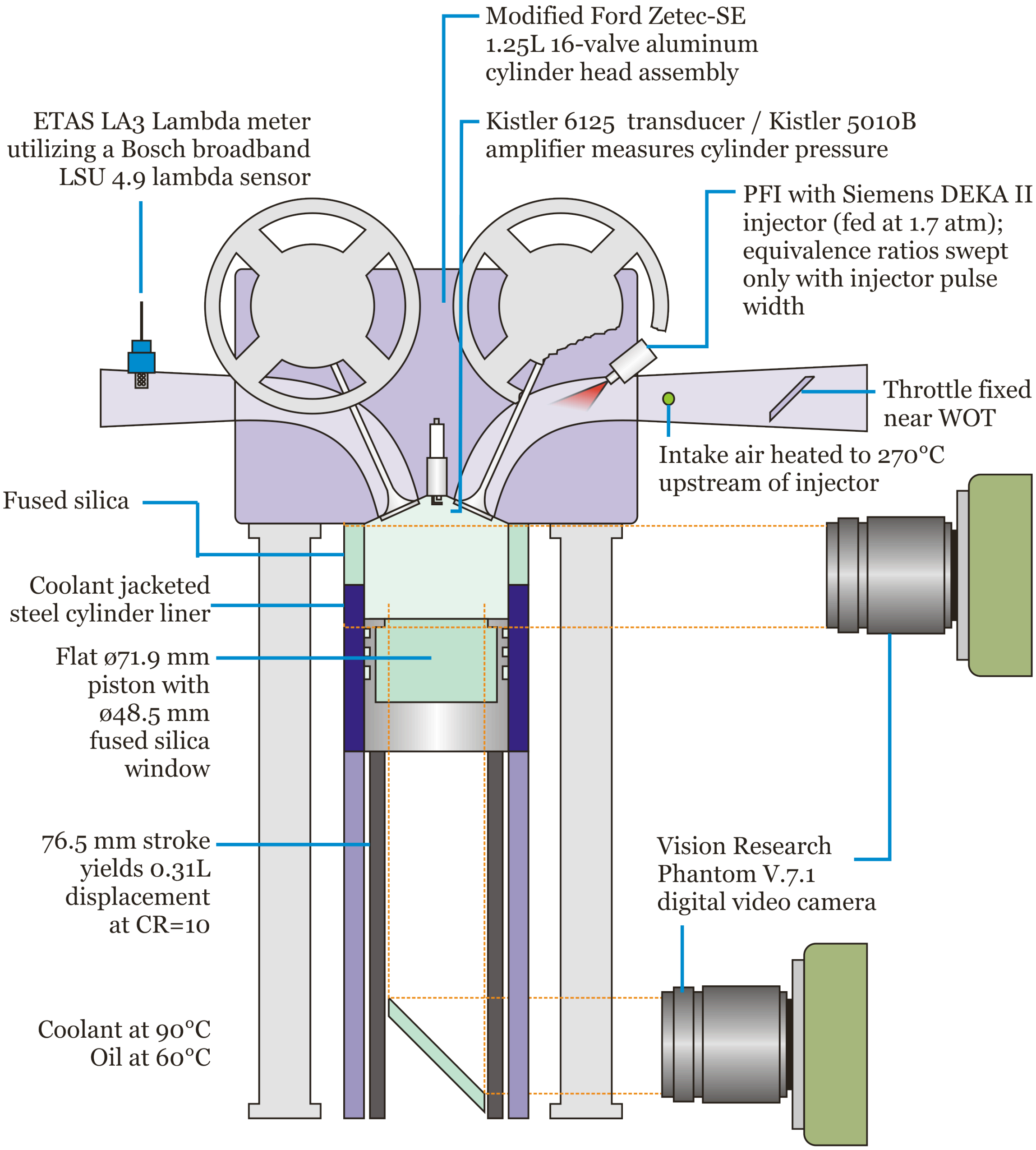

Figure 4.3: Schematic of the single-cylinder optical research engine showing the two axes of optical imaging used for spark assisted HCCI investigation. The upper camera position filmed orthogonal (cylinder) imaging. When placed in the lower position, the camera filmed piston view imaging. Only one camera was used in these studies.

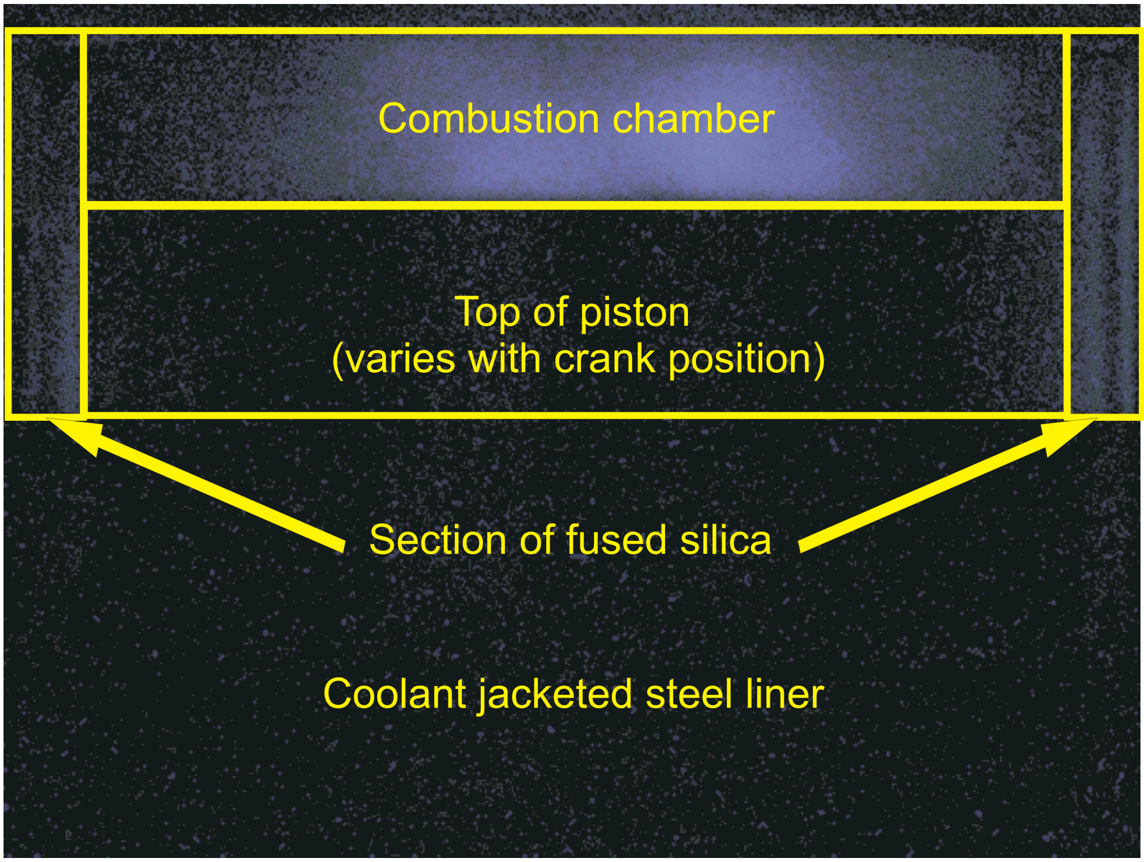

Figure 4.4: Orientation of the orthogonal imaged frames with respect to the cylinder geometry, indicating the optical access through the fused silica cylinder liner extending 25mm below the cylinder head deck surface. The camera viewing the intake side of the cylinder.

Figure 4.5. The pressure traces are superimposed for comparison, both synchronized at Top-Dead-Center (TDC) and showing 360° of crank rotation. HCCI pressure traces showed some cycle-to-cycle variation, but all HCCI pressure traces showed weak ignition. Some traces resembled motoring traces (with no fuel) and did not reveal apparent heat release. Other HCCI traces, like that shown in Figure 4.5, exhibited retarded, low heat release in the expansion stroke (with the example showing a second peak in pressure due to combustion at 26.7° After-Top-Dead-Center (ATDC)). Spark-assisted HCCI pressure traces were much more uniform, showing moderate rates of heat release and consistently advanced ignition timing, always occurring prior to TDC on the compression stroke, like the peak shown in Figure 4.5, which has maximum cylinder pressure at 5.9° BTDC.

Figure 4.6 depicts a typical imaging sequence of the axial view of HCCI combustion for these engine operating conditions. As noted earlier, each imaging view spans a 333 μs interval, including a 309 μs exposure time, resulting in an imaging spacing of approximately 1.4 Crank-Angle-Degrees (CAD). The relative color and intensity of the images in Figure 4.6 have been adjusted for viewing clarity. The imaging sequence shows an initial reaction zone originating near the top of the image, at the edge of the cylinder on the exhaust valve side. This compression ignition zone grows radially inward, bounded by the cylinder wall. The unbounded growth rate based on the imaging sequence is approximately 2 m/s. A second compression ignition zone appears after 1.7 ms (7 CAD). Both reaction zones converge and grow, traversing less than half the combustion chamber area. The light emission then fades. The pressure trace corresponding to these images (not shown) resembles a motoring trace, with almost no apparent heat release indicated.

Figure 4.7 depicts a typical imaging sequence of the orthogonal view of HCCI

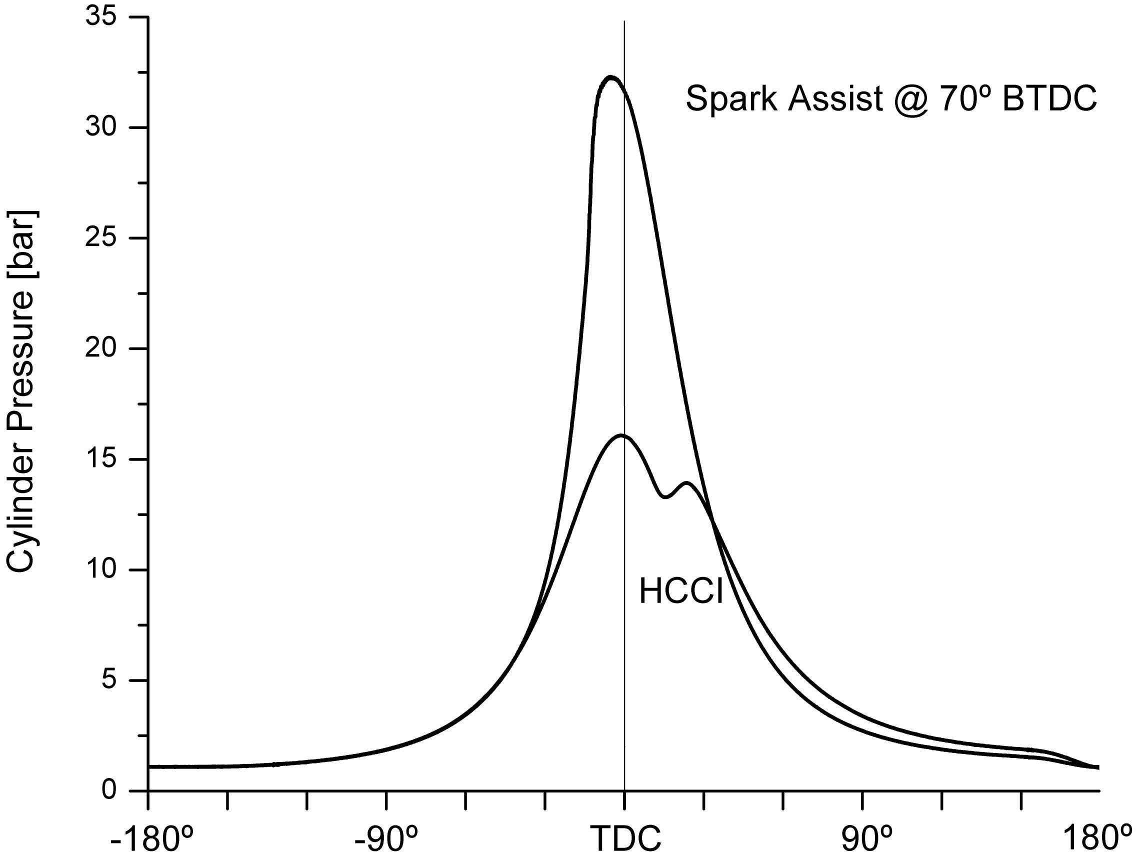

Figure 4.5: Typical pressure histories for HCCI and spark assisted HCCI with identical intake conditions at $T_{int} = 271$ °C, $\phi = 0.62$, with indolene fuel. The data from two experiments are superimposed for comparison. These pressure traces correspond to the side view imaging shown in Figures 4.7 and 4.9.

combustion for these running conditions. The imaging sequence correlates with the HCCI pressure trace shown in Figure 4.5. While imaged at the same 3000 fps rate as all experiments in this study, every fifth image is presented here for clarity. The first visible blue emission begins at 12.1° ATDC, appearing in three areas near the cylinder head deck surface. Recall, the combustion chamber area within the cylinder head is obstructed with this imaging view. As the piston moves through its expansion stroke, the reaction fronts converge and fill the exposed volume of the combustion chamber with nearly uniform, weak blue emission. Note the peak blue intensity in the imaging sequence at 26.2° ATDC coincides with the combustion peak shown in the HCCI pressure trace in Figure 4.5. Radial reaction front growth rate is not apparent from these images, and linear growth along the piston axis appears to be bounded by the piston expansion rate. The blue emission fades quickly by 60° ATDC.

Figure 4.8 depicts a typical axial view imaging sequence of HCCI with spark-assist at 70° BTDC. The images have been gain and color adjusted to expose the plasma front initiated at the spark plug, appearing as the ignition coil is collapsed; the spark initiation appears as the faint blue emission near the center of the first frame of Figure 4.8. Every fifth image is presented in this series. The reaction front initially grows radially at a rate of approximately 3-5 m/s. The reaction front grows radially towards the cylinder walls, filling the entire chamber by 42° BTDC. The light emission becomes more intense during compression, becoming white and peaking in intensity near 21° BTDC. Blue emission fades quickly after TDC and is no longer visible by 48° ATDC.

Figure 4.9 depicts a typical orthogonal view imaging sequence of HCCI with spark-assist at 70° BTDC. This imaging sequence matches the spark-assisted HCCI pressure trace shown in Figure 4.5. Again, every fifth image is presented here. Figure 4.9

begins with the compression stroke, showing the first visible blue emission appearing near the cylinder head deck surface near the center at 49.6° BTDC. Recall this imaging view hides the combustion chamber area within the cylinder head, so the spark plug is not visible. The bottom edge of the spark plug ground electrode is approximately 5mm above deck surface. The imaging sequence shows the single reaction front from the spark plug grows radially outward. The initial reaction front radial growth rate is approximately 2-4 m/s, and the front reaches the outward edge of the cylinder walls by 13.9° BTDC. The reaction front from the spark plug initially grows axially towards the piston at an approximate rate of 4-5 m/s, but the front is quickly bounded by the advancing piston surface. The blue emission becomes very intense prior to TDC, but the piston occludes nearly the entire view at TDC. The images in Figure 4.9 show the decay of blue emission as the piston proceeds through the expansion stroke.

The imaging data show that characterizing the origin of the reaction front, the number of initiation sites and corresponding direction, and growth rates are possible with both axial and orthogonal imaging. Specifically, the axial view images indicate that ignition initiates at multiple points about 10° ATDC in the case of HCCI. The combination of the axial and orthogonal view images show that the weak propagation that occurs after ignition is not localized and occurs throughout the combustion chamber. As noted earlier, the initial ignition sites grow radially at around 2 m/s and propagate axially at the rate of piston expansion. Previous work has shown the initial ignition sites are located in preferential zones in this engine (Figure 3.21) [39]. Secondary sites may develop and contribute to more fuel charge consumption; however, the entire fuel charge is not consumed, and combustion continues to occur during the expansion stroke. At these intake conditions, the bulk charge does not ignite in desirable HCCI form.

For the spark-assisted conditions, the plasma formed at the spark plug produced a reaction front which traveled downward to meet the advancing piston and radially outward to consume the fuel charge. The orthogonal view images show that the reaction front propagates at approximately the same rate (2-5 m/s) in the axial and radial directions and that the reaction front initiated by the plasma is approximately spherical in shape.

While spark-assist advanced overall ignition timing and produced much larger apparent heat release (as demonstrated by the pressure data), spark-assist did not trigger compression ignition of the bulk charge for these conditions. This is in contrast to prior experiments conducted with this engine at different operating conditions where spark-assist resulted in a small radial reaction front which grew for a short period of time, triggering advanced compression ignition of other sites which instead rapidly consumed the bulk charge. The triggering behavior was observed for slightly warmer intake air conditions at the same equivalence ratio and for less lean equivalence ratios at the same intake temperature. The results of this work suggest a gradual transition takes place, depending on intake conditions and equivalence ratio where the nature of spark-assist ignition phenomena changes.

4.4 Spark-Assisted HCCI Parametric Study Imaging Results and Discussion

The previous series of experiments, discussed in Section 4.3, used both orthogonal imaging through the cylinder wall and to piston window to further characterize the spark assisted HCCI ignition event and reaction front propagation. The subsequent more expansive parametric study utilized only piston window imaging (with the coolant-jacketed steel cylinder liner). These studies varied intake air temperature, equivalence ratio, and spark advance timing to further characterize the nature of and effectiveness of spark assist in expanding HCCI operation to low load, lean operating conditions. Figure 4.10 depicts the parametric space expanded during the course of the experiments. The significance of the colored regions in Figure 4.10 will be discussed later. As previously indicated, each typical experiment consisted of collecting crank angle (i.e. time resolved) imaging and pressure data in a two-step process, beginning with HCCI operation, then adding spark assist. For example, consider a series of experiments with $T_{int} = 271$ °C and $\phi = 0.45$. One experiment, "A" began as HCCI, then transitioned to spark assist at 20° BTDC. Experiment "B" also began as HCCI, then transitioned to spark assist at 50° BTDC; other experiments followed similarly. Table 4.1 provides a summary of the conditions studied and Figure 4.2 presents typical pressure data that would be acquired when transitioning from unassisted HCCI to spark assisted HCCI. The detailed results are presented and discussed below.

4.4.1 Spark-Assist Advance Timing Effects

For each fixed intake temperature and equivalence ratio, spark assist ignition timing was varied. An example of the resulting behavior is shown in Figure 4.11, in the form of cylinder pressure time histories over 360 CAD superimposed from three experiments. In Figure 4.11, intake air temperature was held at 270-271 °C and fuel delivery was held to ϕ = 0.45-0.47. The HCCI pressure trace resembles a motoring engine trace, with a peak pressure of approximately 17 bar just before TDC. No apparent heat release is captured via the pressure transducer. The imaging reveals very weak HCCI combustion during the expansion stroke, typically with one or two compression ignition sites slowly expanding to consume a portion of fuel before diminishing. These HCCI combustion events appear even weaker than those shown in Figure 3.4 (for which $T_{int} = 317$ °C, $\phi = 0.44$), consistent with the lower temperatures. Adding spark assist at 20° BTDC results in a pressure histories which, while they varied, showed modest heat release peaking after TDC, as seen in Figure 4.11. Figure 4.12 shows the imaging sequence corresponding to the 20° BTDC pressure trace. The image sequence shows blue emission developing initially around the spark plug electrodes. The emission around the spark plug expands slowly radially outward. The propagation front consumes nearly all of the fuel charge before a secondary compression ignition site forms near the edge of the piston window (see the bottom panel of Figure 4.12). Further imaging stills (not shown) indicate the reaction fronts move radially outward until chemiluminescence fades later in the expansion stroke. Figure 4.11 also shows a typical pressure history for spark assist timing of 70° BTDC. This pressure trace shows the effect of fairly advanced spark assist timing, resulting in large apparent heat release prior to TDC (and slight knocking noise at the pressure peak). While not shown in Figure 4.11, advancing spark assist timing to 90° BTDC had a slight negative effect, resulting in occasional misfire.

In general, for the range of conditions studied, advancing spark assist timing resulted in increased apparent heat release with increasing peak cylinder pressures up to a point. After this point, further increase resulted in occasional misfire. Up to the inflection point, advancing spark assist timing also advanced combustion phasing. The inflection point occurred at approximately 70° BTDC for $\phi = 0.44$, and decreased slightly to 50° BTDC for slightly less lean conditions. This behavior is illustrated in Figure 4.10 as red shading under each experimental condition with increasing intensity of color indicating the timing of the spark assist that corresponds to the inflection point. Note, there is a coupled effect of spark assist ignition timing with intake temperature, which is discussed next.

4.4.2 Intake Temperature Effects

Intake air temperature was varied over a relatively narrow window (approximately 25 °C) for this study, due to the extreme sensitivity of the system to intake air temperature. Typical results for three air intake temperatures are presented in Figure 4.13, showing superimposed cylinder pressure time histories over 360 CAD. The experiments held fuel delivery to $\phi = 0.45$-0.47 and spark assist ignition advance at 20° BTDC. The pressure history, for 257 °C, closely resembled a motoring trace, with little apparent heat release. Imaging revealed very weak blue emission beginning at the spark plug, which established a weak reaction front which radially advanced to consume some of the fuel charge. The second pressure history for 271 °C showed modest heat release peaking after TDC. This image sequence was presented previously as Fig. 4.12 and showed blue emission initially developed around the spark plug electrodes and expanded slowly radially outward. The propagation front consumed nearly all of the fuel charge before a secondary compression ignition site formed near the edge of the piston window. The third pressure history for 281 °C showed even more apparent heat release. The images corresponding to this pressure time history are shown in Figure 4.14, and also showed local emission formed initially around the spark plug and expanded radially outward. The propagation front consumed part of the fuel charge before multiple compression ignition sites formed near 5 o'clock and 9 o'clock in the 17th frame. These compression ignition sites quickly advanced to consume the remainder of the fuel charge. Note that the peak cylinder pressure increased to about 27 bar (over about 21 bar for the 271 °C case), and the pressure peak occurred slightly earlier (about 5 CAD) of the peak pressure of the 271 °C case during the expansion stroke.

In general, for the range of conditions studied, increasing intake temperature resulted in increased apparent heat release with increasing peak cylinder pressures. This behavior is illustrated in Figure 4.10 as the shading bar on the left side of the figure, which graduates from green at the bottom (indicating weaker combustion) to orange at the top (indicating stronger combustion). This behavior exists for both HCCI and spark assisted HCCI conditions. The range of effectiveness of spark assisted HCCI; however, exists over a narrow range of intake temperatures.

There is a coupled effect between intake temperature and equivalence ratio on the effectiveness of spark assist on HCCI. For higher intake temperatures and less lean conditions, where HCCI combustion is robust, spark assist has little influence on combustion phasing and power. For higher intake temperatures and leaner conditions, spark assist has some influence. An example of this condition is shown in Figure 4.15. This figure shows the results of indolene HCCI experiments (310-320 °C intake temperature), with the addition of data for spark assist at 5 ° BTDC for an even leaner condition of $\phi = 0.4$. For lower intake temperatures, and leaner conditions, spark assist has little influence (even with advanced spark timing, as was tested, but not presented here).

4.4.3 Equivalence Ratio Effects

Equivalence ratio was varied over the course of the parametric study, from $\phi = 0.62$ to 0.45. Figure 4.16 illustrates one experimental series, showing cylinder pressure history over 360 CAD superimposed from two experiments with fixed spark assist timing at 20° BTDC and intake air temperature at 270-271 °C. The pressure history shown for $\phi = 0.45$ showed modest heat release peaking after TDC. As discussed previously for their conditions, this image sequence (Fig. 4.12) shows blue emission initially developed around the spark plug electrodes and expanded slowly radially outward. The second pressure time history for $\phi = 0.52$ showed higher heat release. Peak cylinder pressure increased to approximately 31 bar. Even though both experiments had spark assist at 20° BTDC, the less lean condition showed more heat release during the end of the compression stroke, which accelerated combustion.

In general, for the range of conditions studied, increasing equivalence ratio resulted in increased apparent heat release with increasing peak cylinder pressures. This behavior is illustrated in Figure 4.10 as the shading bar on the top of the figure, which graduates from faded to stronger red (indicating stronger combustion). This behavior matches the general behavior of indolene fuel as studied in HCCI operation and discussed in Chapter III. Varying equivalence ratio has a much weaker effect than either intake temperature or spark assist advance timing. However, given a fixed intake temperature and spark advance timing, increasing equivalence ratio slightly advances combustion phasing, which has a dramatic effect on peak cylinder pressure if phasing advances prior to Top-Dead-Center (TDC).

4.4.4 Reaction Front Propagation Regimes

The chemiluminescence imaging results from the spark assisted HCCI parametric study of intake air temperature, ϕ, and spark assist advance timing revealed differences in the nature of the combustion events. All ignition events began with plasma discharge at the spark plug electrodes which produced blue emission, indicating the formation of a reaction zone. From that point, however, two ignition propagation regimes were found to exist.

One ignition propagation regime is typified by an initial reaction zone formed around the spark plug, which quickly accelerated the formation of subsequent compression ignition sites that consumed the fuel charge. An example of this behavior, referred to as Regime 1, appears in Figure 4.17. This image came from the pressure time history shown in Figure 4.15, with $T_{int} = 321$ °C, $\phi = 0.40$, and spark assist at 5° BTDC. The imaging sequence showed the spark plug fired in the first image, followed by blue emission from the radial reaction zone formed around the spark plug. This reaction zone expanded for about 7 CAD. By the 6^{th} image, only 1.4 CAD later, a secondary compression ignition site appeared at the 9 o'clock position. This secondary compression ignition site nearly instantaneously covered about the same area as was covered by the slowly growing spark ignition reaction zone. In the next image, another secondary compression ignition site appeared at the 3 o'clock position. At this point in time, emission from both of the compression ignition reaction zones covered a significant portion of the piston viewing area; the spark ignition reaction zone, however, remained small. The secondary compression ignition sites very quickly filled the piston window with blue emission as the fuel charge was consumed. As is typical with Regime 1 ignition propagation, the reaction initiated by the spark plug accelerated the formation of secondary compression ignition sites.

In previous University of Michigan rapid compression facility (UM RCF) studies of weak and strong ignition regimes [8], it was determined that the primary effect of discrete ignition sites on the remaining unreacted charge was to increase the pressure of the test gases in the combustion chamber; thereby increasing the temperature of the mixture. This also appears to be the case with the HCCI events that are described as Regime 1. The reaction initiated at the spark plug serves to increase the overall temperature of the test gas mixtures, thus accelerating autoignition in the regions already identified in the unassisted HCCI studies (see Chapter 3) as regions of preferential ignition (i.e. the hotter locations within the combustion chambers).

The second ignition propagation regime is typified by consumption of the fuel charge by radial reaction front propagation from the spark plug. An example of this behavior, referred to as Regime 2, appears as Figure 4.12. This image sequence came from the pressure time history shown in Figure 4.13 with T_{int} = 271 °C, ϕ = 0.45, and spark assist at 20° BTDC. The imaging sequence showed the spark plug fired in the first image, followed by blue emission which grew radially outward at about 1-2 m/s. The lowest panel in the image series shows that after 5 ms (over 21 CAD), a secondary compression ignition site appeared at the 8 o'clock location. The compression ignition reaction front grew radially outward at about the same rate, eventually meeting the spark ignition reaction front. As is typical with Regime 2 ignition propagation, the fuel charge was predominately consumed by the relatively slowly expanding reaction front emanating from the spark plug. While this exampled showed some autoignition induced by the spark plug reaction front, other imaging sequences showed no development of secondary compression ignition sites, and the fuel charge was consumed by the spark-initiated reaction front only.

These two ignition regimes were not binary, and ignition fronts bridging the two types were observed. One such example appears as Figure 4.14. This image sequence came from the pressure time history shown in Figure 4.13 with T_{int} = 281 °C, ϕ = 0.47, and spark assist at 20° BTDC. The imaging sequence showed the spark plug fired in the first image, followed by blue emission which grew radially outward at about 2-3 m/s. The 16^{th} image in the series shows that after about 53 ms (over 22 CAD), a secondary compression ignition site appeared at the 9 o'clock location.

Unlike the imaging for the Regime 2 example discussed above, the secondary compression ignition sites then rapidly developed to consume the fuel charge. The time frame for this secondary compression ignition site development is much slower than the Regime 1 example discussed above.

In general, Regime 1 (where autoignition dominated) was observed at higher intake temperatures. Regime 2 (where spark plug initiated reaction front propagation dominated) was observed at lower intake temperatures. In the previous UM RCF studies of iso-octane ignition [8], the ignition regimes were found to be a strong function of the fuel mole fraction; not temperature. Reaction fronts (as opposed to homogeneous autoignition) formed preferentially at higher fuel mole fractions. Here, the data for equivalence ratio (and thereby fuel mole fraction) are convolved with changes in the charge temperature, as discussed earlier in Chapter 3. Delineation between Regime 1 and Regime 2 as a function of ϕ are consequently less clear.

4.5 Engine Combustion Performance Metrics

The previous sections discussed the parametric studies of varied intake air temperature, equivalence ratio, and spark advance timing, and characterized the nature and effectiveness of spark assist in expanding HCCI operation to low load, lean operating conditions. This discussion would be incomplete without further consideration of how spark assisted HCCI operation into expanded low load operating conditions translates to other engine combustion performance metrics. The ability of the engine to operate in an expanded low load, lean region does not inherently mean this is beneficial. As a consequence, consideration was given here to combustion stability, knock and useful power output.

Figure 4.18 shows pressure time histories for sequential firing cycles under identical intake conditions (T_{int} = 270-271 °C, $\phi = 0.62$). Each experiment was transitioned from HCCI into spark assisted HCCI about 4-5 seconds into the experiment, with different spark assist advance timing. The spark assist timing of 20° BTDC shows a marked response to spark assist for the first cycle at which it was presented; then engine immediately goes into an apparently unstable mode. Spark advance timing of 50° and 70° BTDC both show greater response (in terms of peak pressures) to spark assist and much more stable operation (with peak cylinder pressure standard deviations of 0.6 at 50° and 0.3 at 70° advance timing compared to 3.6 for 20° and 6.8 for 90° advance timing). Spark advance timing of 90° BTDC results in strong response to the spark, but with significant misfire cycles.

Engine knock is another significant consideration for successful HCCI operation. Figure 4.19 presents a comparison of the rate of pressure rise for spark assisted HCCI operation and baseline unassisted HCCI operation. The figure includes all of the sequential firing cycles for conditions of T_{int} = 270 °C, $\phi = 0.62$, and where the spark assist timing is set at 50° BTDC. The spark assist dP/dt data correspond to the pressure data presented in Fig. 4.18. Note the HCCI data are virtually identical to engine motoring conditions, with no appreciable heat release indicated by the pressure transducer. Although there is some variability in the phasing (or timing of the point in the cycle where the maximum in pressure is observed), the rates of pressure rise for the spark-assisted HCCI are all well below the general criterion of a maximum of dP/dt less than 50 bar/ms ($5\text{x}10^4$ bar/s). Note that phasing is not considered a significant concern in this work, as this study focused on feasibility and sensitivity not optimization.

Figure 4.20 presents the average net (720 CAD) indicated mean effective pressures

(IMEP) for HCCI versus spark assist for the same data sets presented in Figure 4.18. The standard deviations in IMEP for each firing cycle are indicated as error bars. The HCCI operation is virtually identical to the engine motoring data at these conditions. Since the 50° and 70° BTDC spark assist HCCI operation both yield significant pressure rise on the compression stroke, net IMEP is slightly lower for these cases than for the more retarded 20° BTDC spark assist advance timing.

As an indication of the significance of the IMEP values relative to actual engine operation, Figure 4.21 presents the brake mean effective pressure (BMEP) versus engine speed, reproduced from Santoso et al. [3] for a mid-size vehicle (Ford Taurus). This plot shows second-by-second operating points on the engine map for the U.S. Federal Testing Procedure (FTP) Urban Fuel Economy Driving Cycle. Santoso et al. superimposed the HCCI operating boundary according to Zhao et al. [4] on the FTP cycle data. According to Zhao et al., the lower boundary of HCCI operation near 1.5 bar BMEP is limited by misfire. Consider that only 40% of the operating points are within the HCCI operating regime (versus 75% for the EPA Highway Fuel Economy Cycle) and that mode transitions are not frequent [3]. Figures 4.20 and 4.18 indicate that stable HCCI operation with an IMEP of just over 2 bar could be delivered with spark assist (e.g. with a timing of 50° BTDC at $\phi = 0.62$). Given a target IMEP of just under 2.5 bar for 700-1000 RPM (recall 700 RPM was maintained for all of the optical engine experiments), Figure 4.21 shows large potential to operate an engine in this spark assisted HCCI mode, as opposed to traditional throttled SI engine operation with $\phi = 1$. This example clearly shows spark assisted HCCI operation has the potential to cover a significantly larger portion of the FTP Urban Driving Cycle than unassisted HCCI.

4.6 Summary and Conclusions

The spark-assisted HCCI study covered a wide range of engine operating conditions and the resulting data covered a broad spectrum of combustion parameters, including time-resolved multi-axis imaging of the ignition and combustion phenomena and engine performance metrics. The results presented in this chapter included detailed discussion of typical single-cycle events, as well as consideration of multi-cycle data. The results clearly document the effect spark assist can have on extending HCCI low-load operation at realistic engine powers. The characteristics of various modes of ignition have been documented in terms of conditions leading to autoignition and conditions leading to reaction front propagation. Both regimes yielded spatially resolved phenomena that indicate how inhomogeneous the initial in-cylinder conditions are at these low loads. Such information is vital to our understanding of low temperature combustion and how to design successful strategies to extend HCCI operation.

The imaging data present new information on how ignition is initiated and how combustion proceeds at typical low temperature engine operating conditions when spark assist is used. These data bridge our understanding of combustion fundamentals on ignition regimes from the idealized conditions found in chemical reactors, such as RCFs, to practical combustion devices. It is important to note that existing HCCI modeling strategies do not capture and predict the behavior documented in this work. Additionally, the results set direction for how spark assist can be used to extend high load operation and to reduce cycle-to-cycle variation in HCCI behavior.

Figure 4.6: Typical piston view image sequence for weak HCCI combustion. $T_{int} = 271$ °C, $\phi = 0.62$, with indolene fuel.

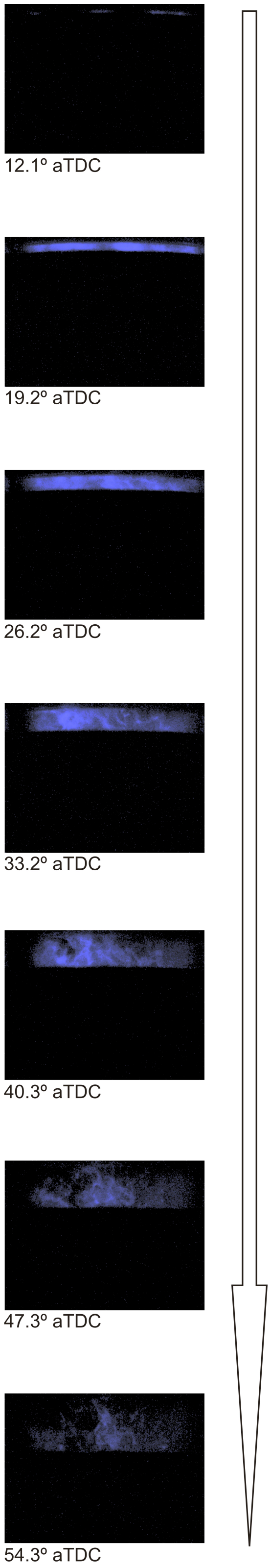

Figure 4.7: Typical orthogonal (side) view image sequence of HCCI combustion. T_{int} = 271 °C, ϕ = 0.62, with indolene fuel. Every fifth image is presented in the sequence.

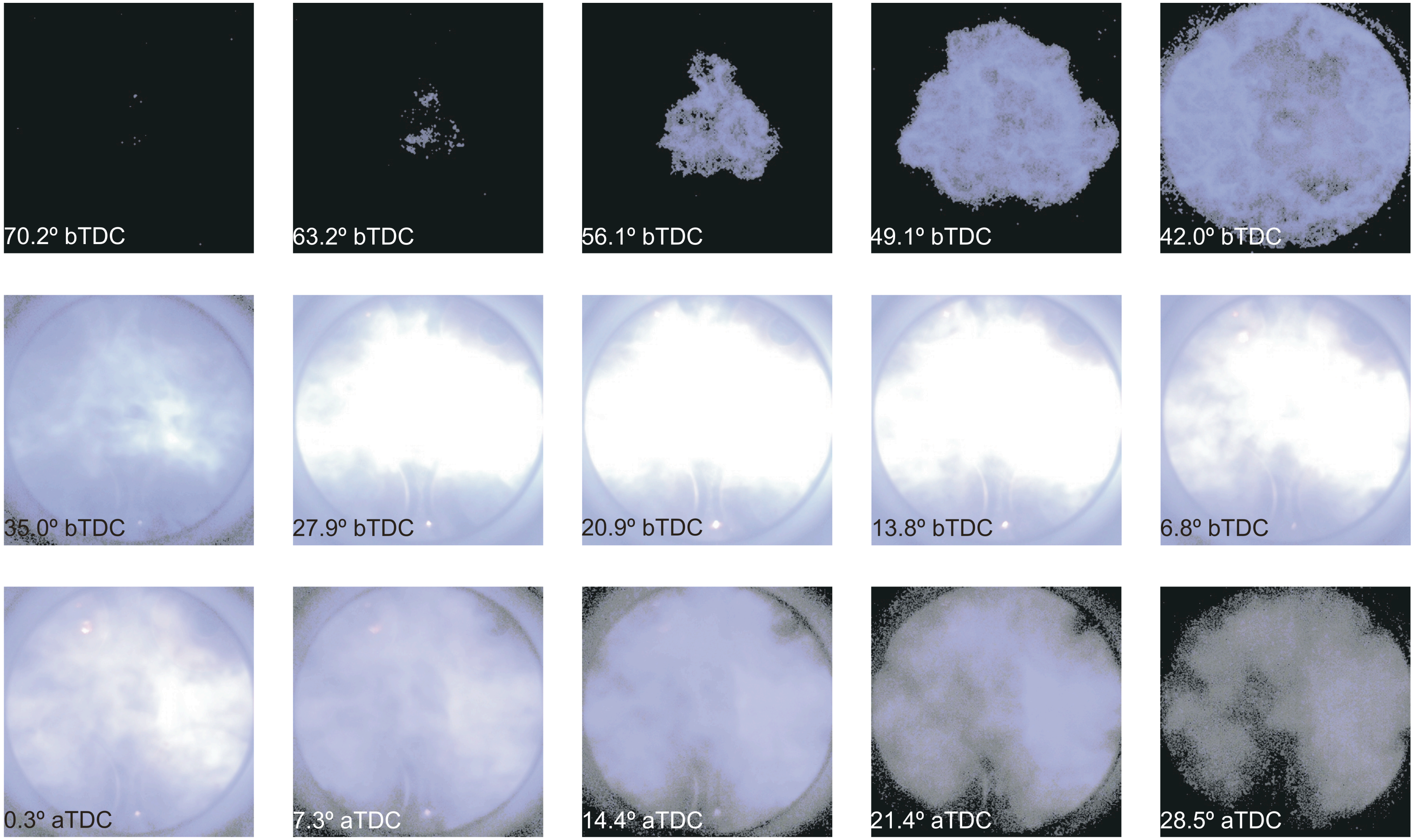

Figure 4.8: Typical piston view image sequence sequence for HCCI with spark assist. T_{int} = 271 °C, ϕ = 0.62, spark assist at 70 °BTDC, with indolene fuel. Every fifth image is shown in the sequence.

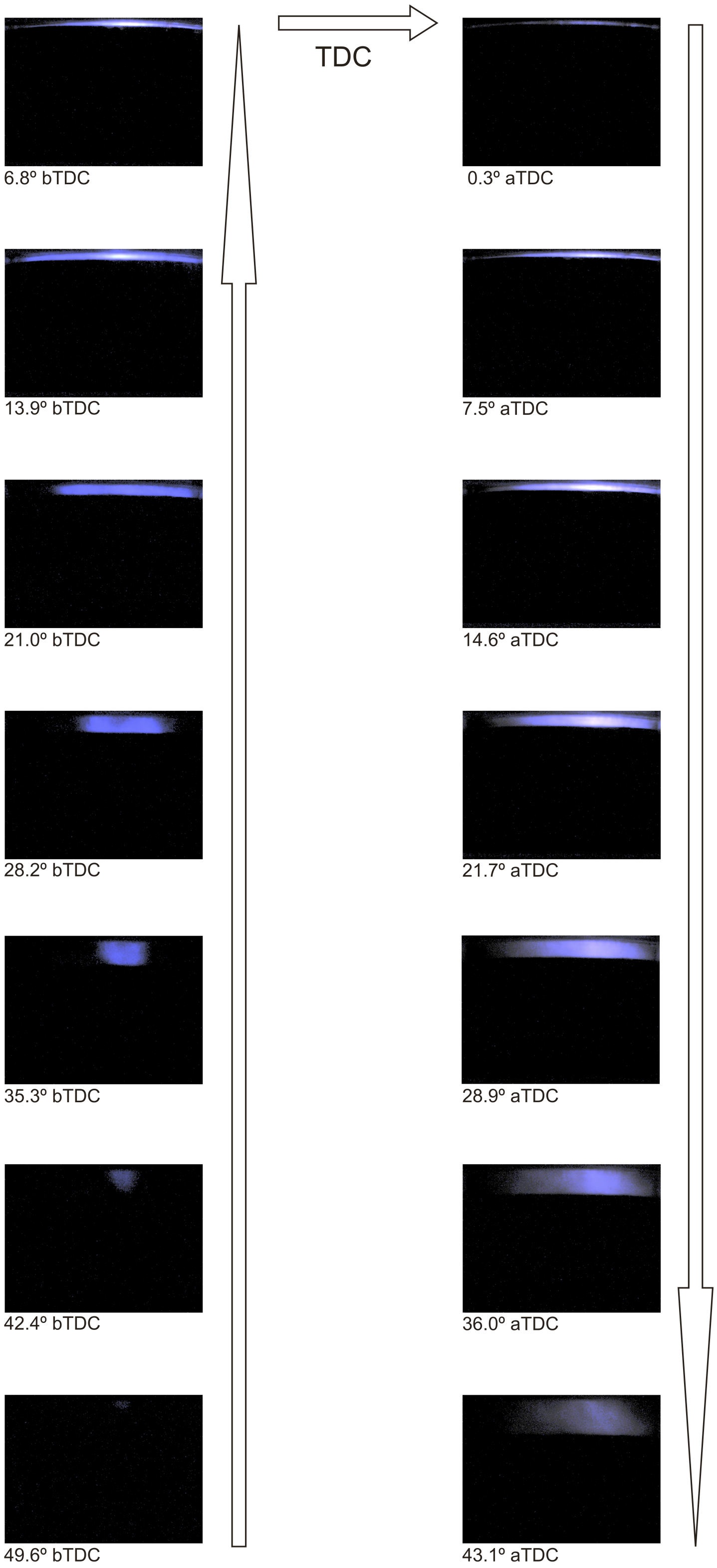

Figure 4.9: Typical orthogonal (side) view image sequence of spark assisted HCCI combustion. T_{int} = 271 °C, $\phi = 0.62$, spark assist at 70° BTDC, with indolene fuel. Every fifth image is shown in the sequence.

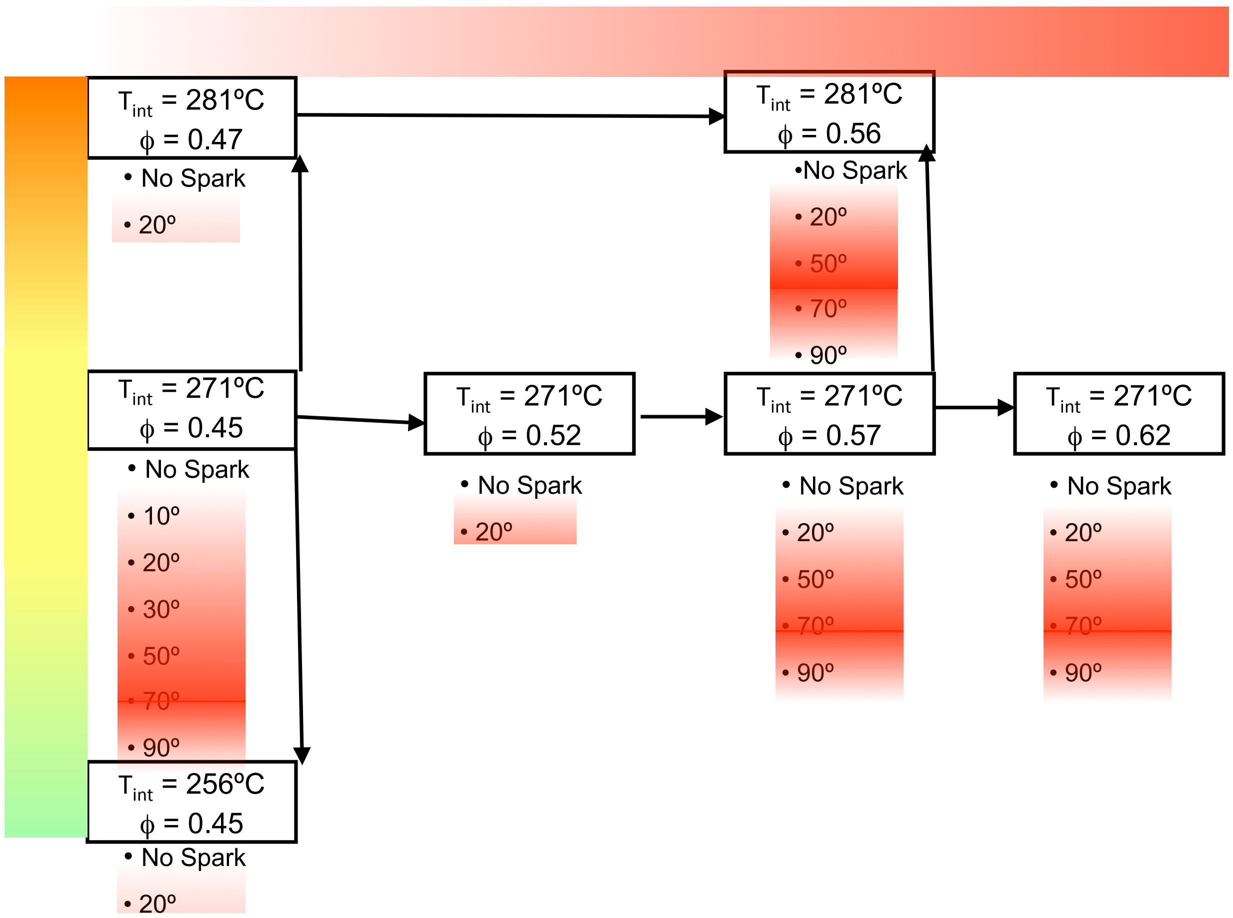

Figure 4.10: Parametric space of intake air temperature, equivalence ratios, and spark advance timing evaluated for spark assisted HCCI.

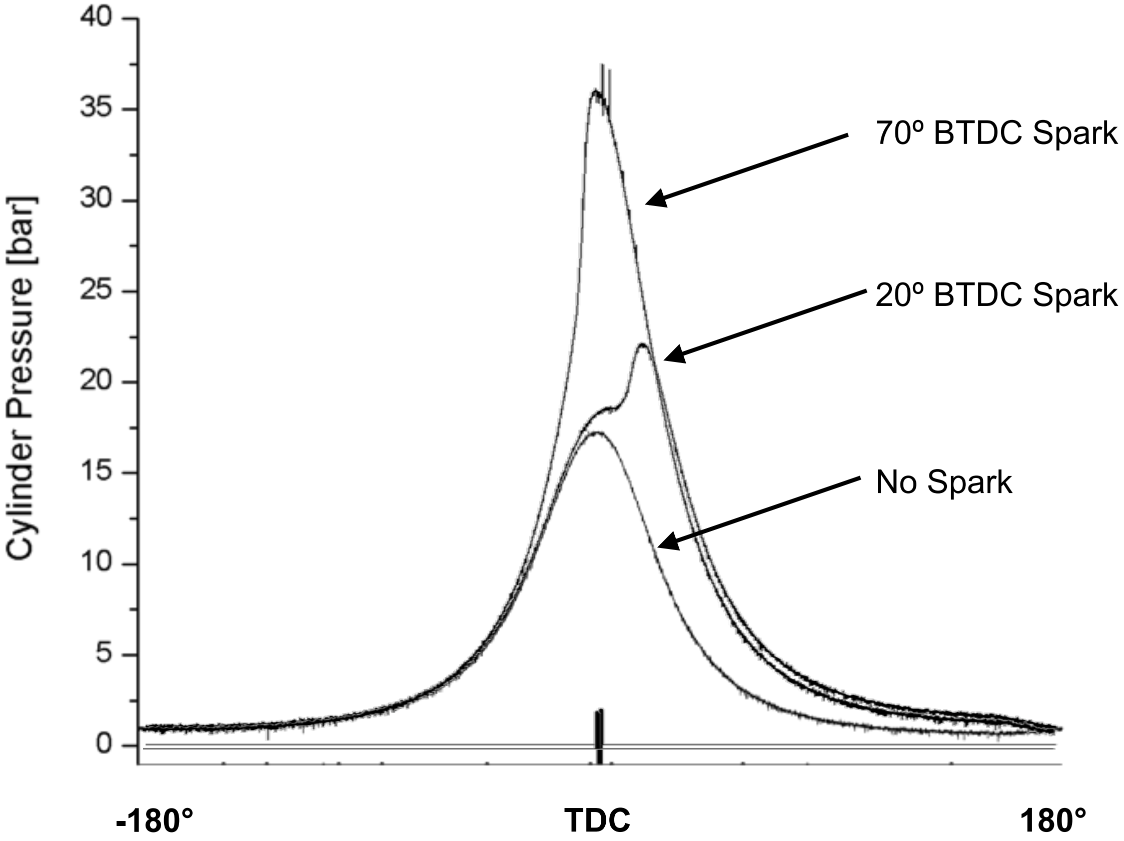

Figure 4.11: Typical cylinder pressure time histories for various spark assist advance timing, superimposed for comparison. T_{int} = 270-271 °C, $\phi = 0.45$-0.47, with indolene fuel.

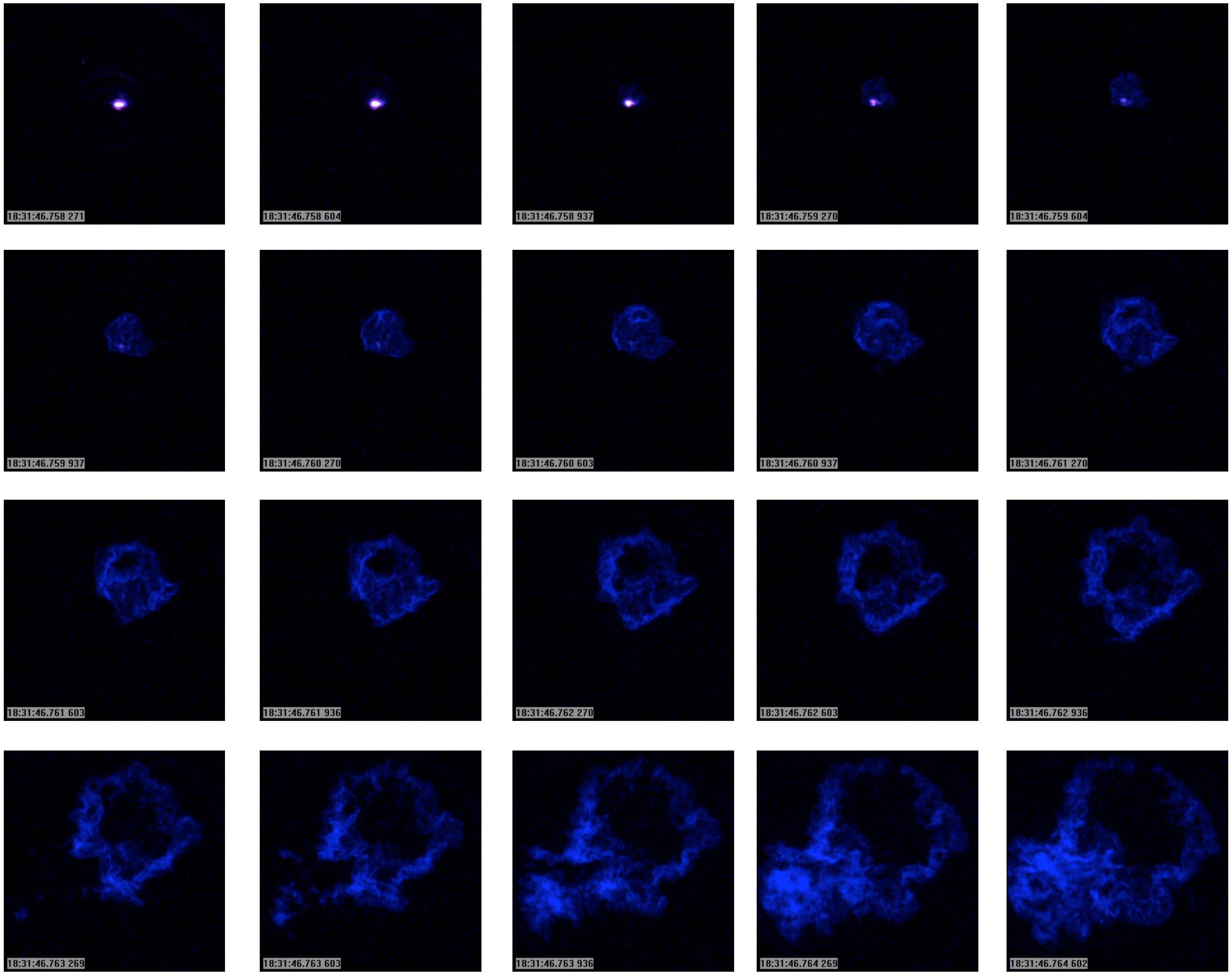

Figure 4.12: Typical imaging sequence for spark assisted HCCI propagation for $T_{int} = 271$ °C, $\phi = 0.45$, spark assist at 20 ° BTDC, with indolene fuel.

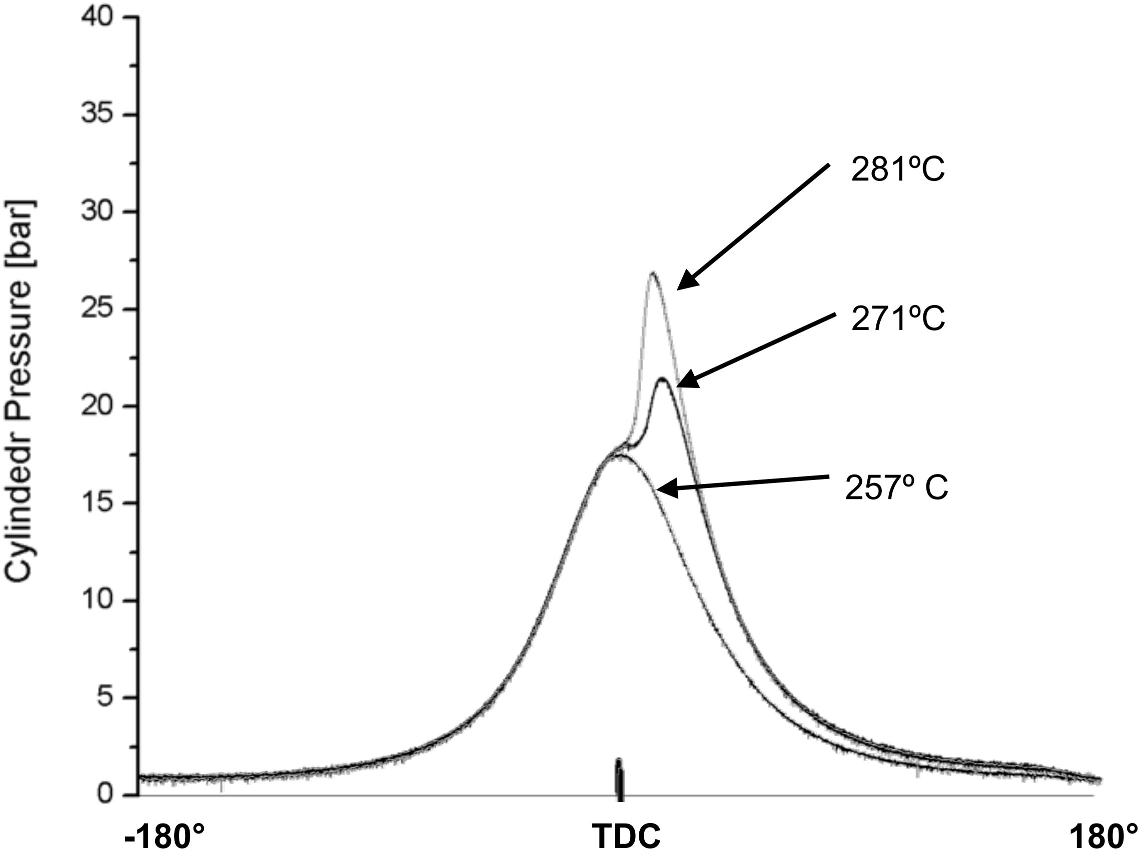

Figure 4.13: Typical cylinder pressure time histories for various intake temperatures, superimposed for comparison. $\phi = 0.45$-47, spark assist at 20° BTDC, with indolene fuel.

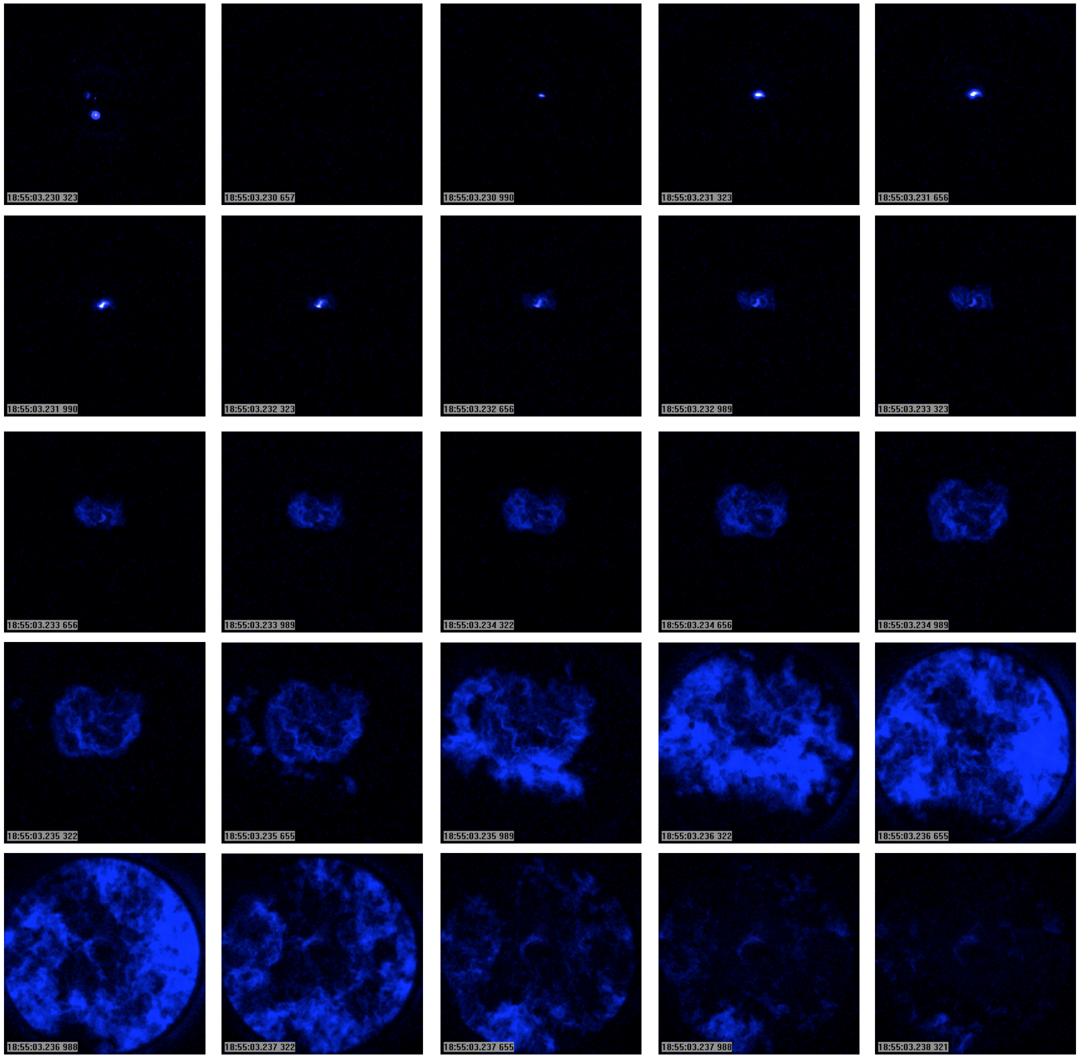

Figure 4.14: Typical imaging sequence for spark assisted HCCI propagation for $T_{int} = 281$ °C, $\phi = 0.47$, spark assist at 20° BTDC, with indolene fuel.

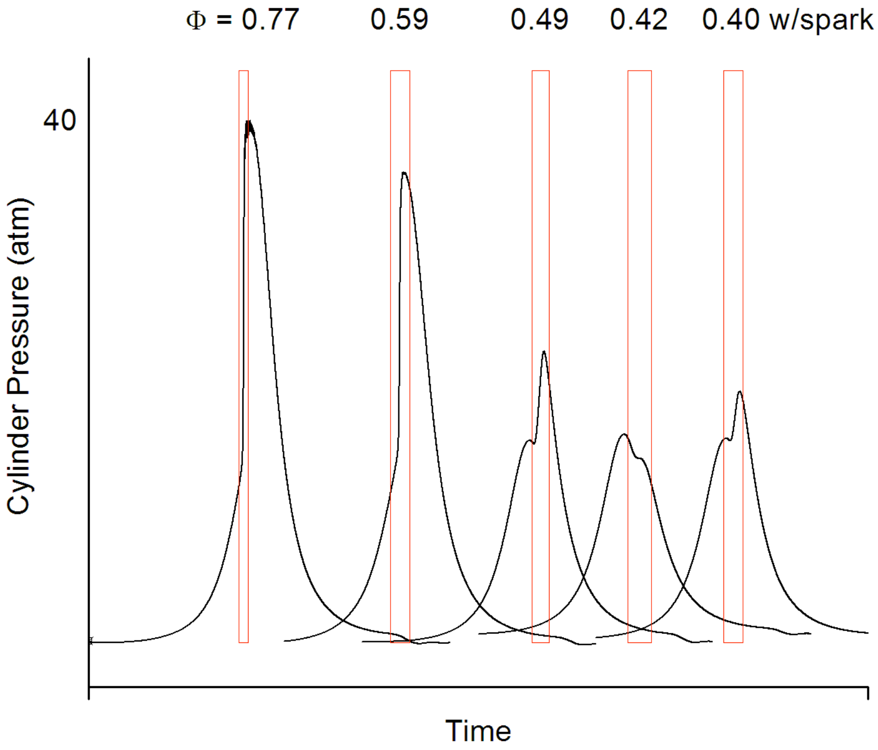

Figure 4.15: Typical pressure time histories for engine conditions with indolene fuel; T_{int} = approx. 310-320 °C. The data are superimposed for clarity. The conditions for $\phi = 0.77$, 0.59, 0.49, and 0.42 are data presented in another study [2]. A lean condition of $\phi = 0.40$ is shown with spark ignition assist added at 5° BTDC. The boxed areas coincide with imaging results shown in Zigler, et al. [2].

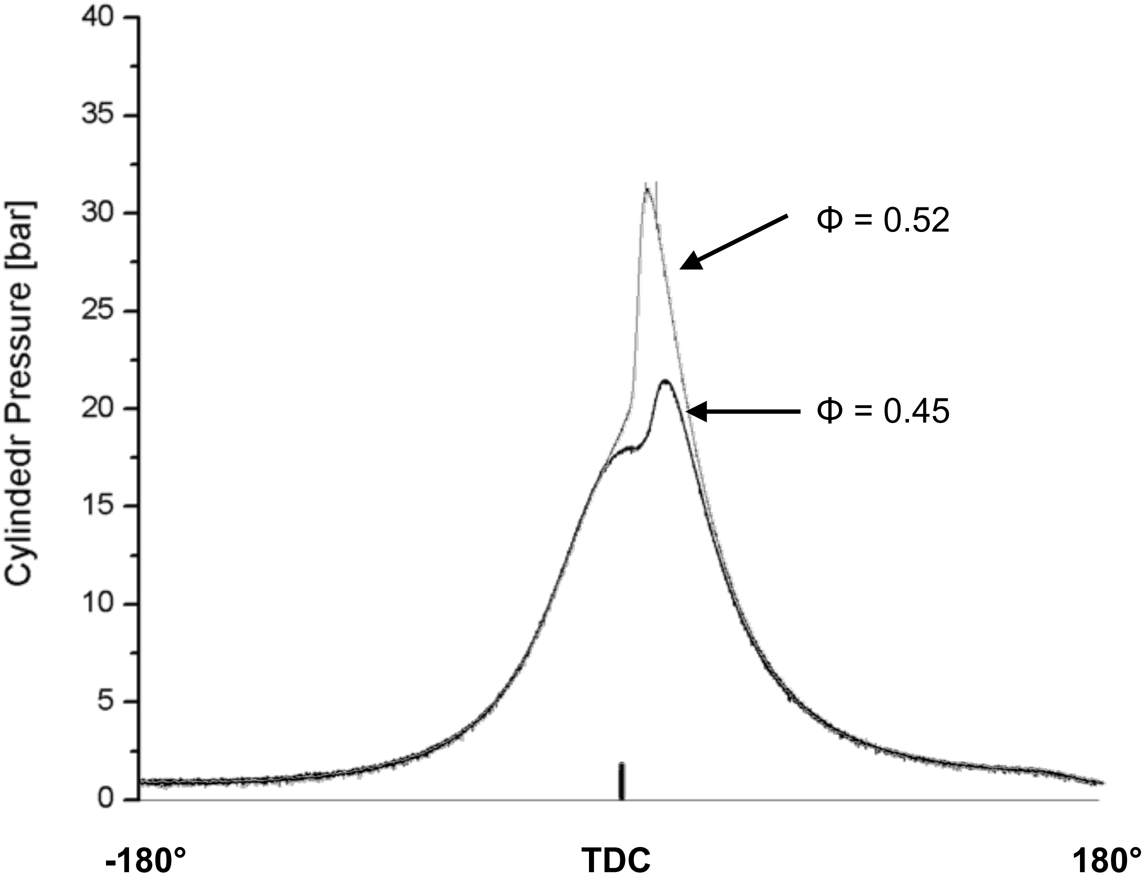

Figure 4.16: Typical cylinder pressure time histories for various equivalence ratios, superimposed for comparison. T_{int} = 271 °C, spark assist at 20° BTDC, with indolene fuel.

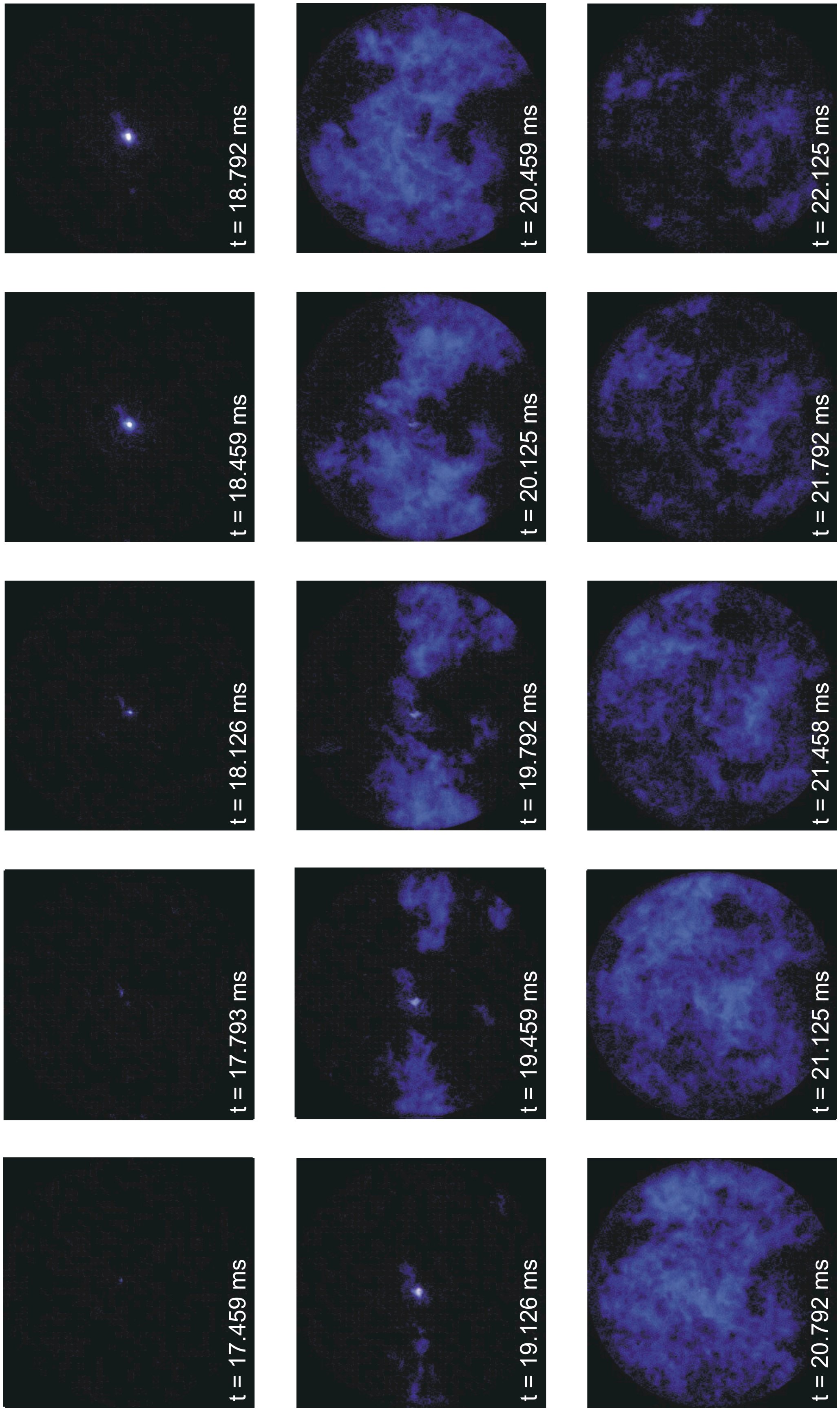

Figure 4.17: Typical imaging sequence for spark assisted HCCI propagation for T_{int} = 321 °C, $\phi = 0.40$, spark assist at 5° BTDC, with indolene fuel.

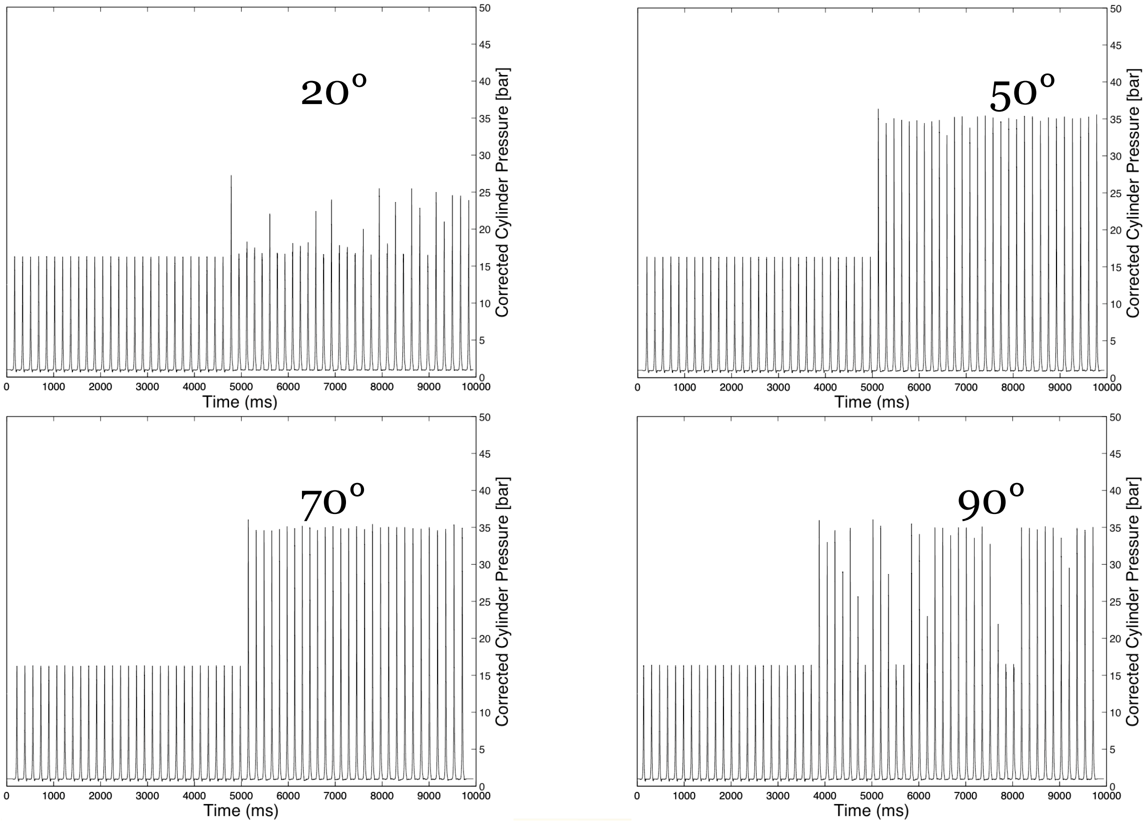

Figure 4.18: Pressure time histories for multiple sequential firing cycles under identical intake conditions of T_{int} = 270-271 °C, $\phi = 0.62$, with indolene fuel. Each experiment is transitioned from HCCI into spark assisted HCCI about 4-5 seconds into the experiment. Each experiment has a different spark assist advance timing, as indicated, including 20°, 50°, 70°, and 90° BTDC.

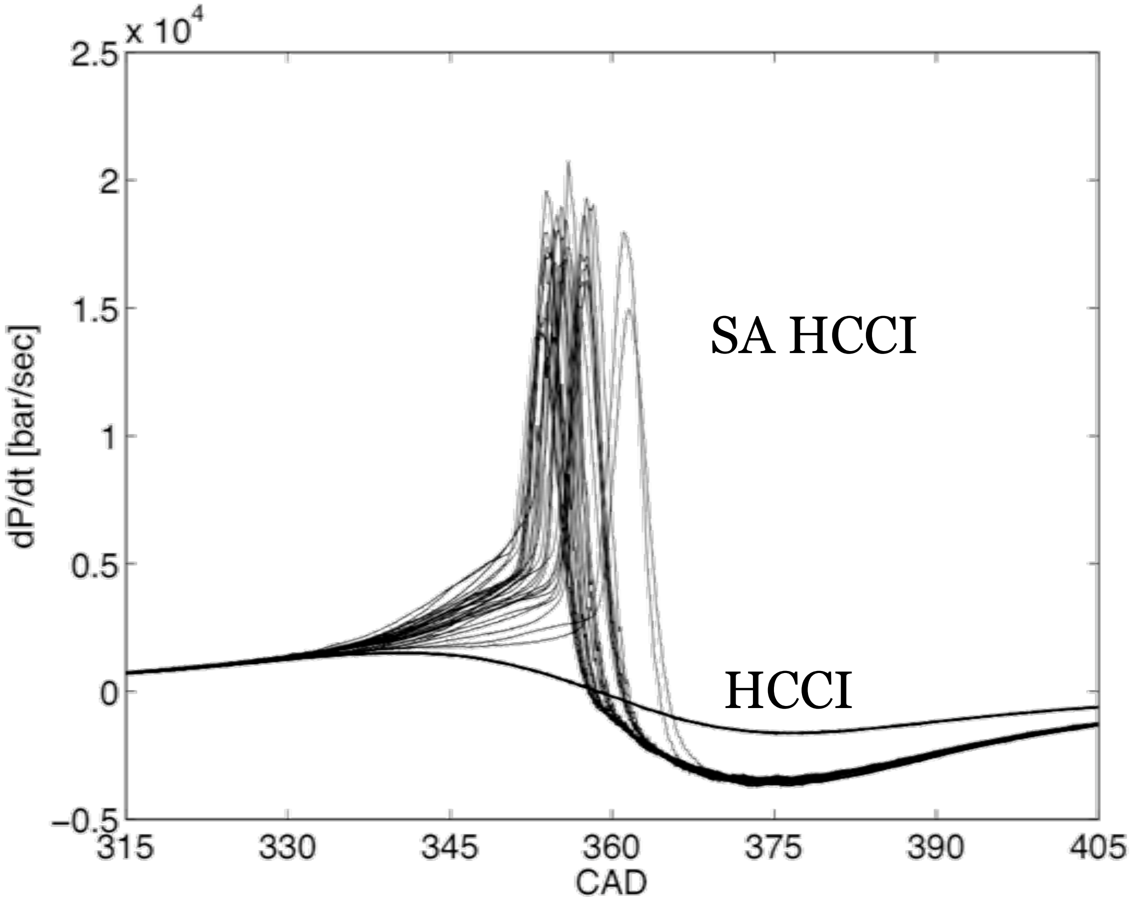

Figure 4.19: Comparison of the rate of pressure rise [bar/ms] for HCCI and spark assisted HCCI engine operation. Firing conditions are T_{int} = 270 °C and $\phi = 0.62$, with indolene fuel. The spark assist is timed at 50° BTDC.

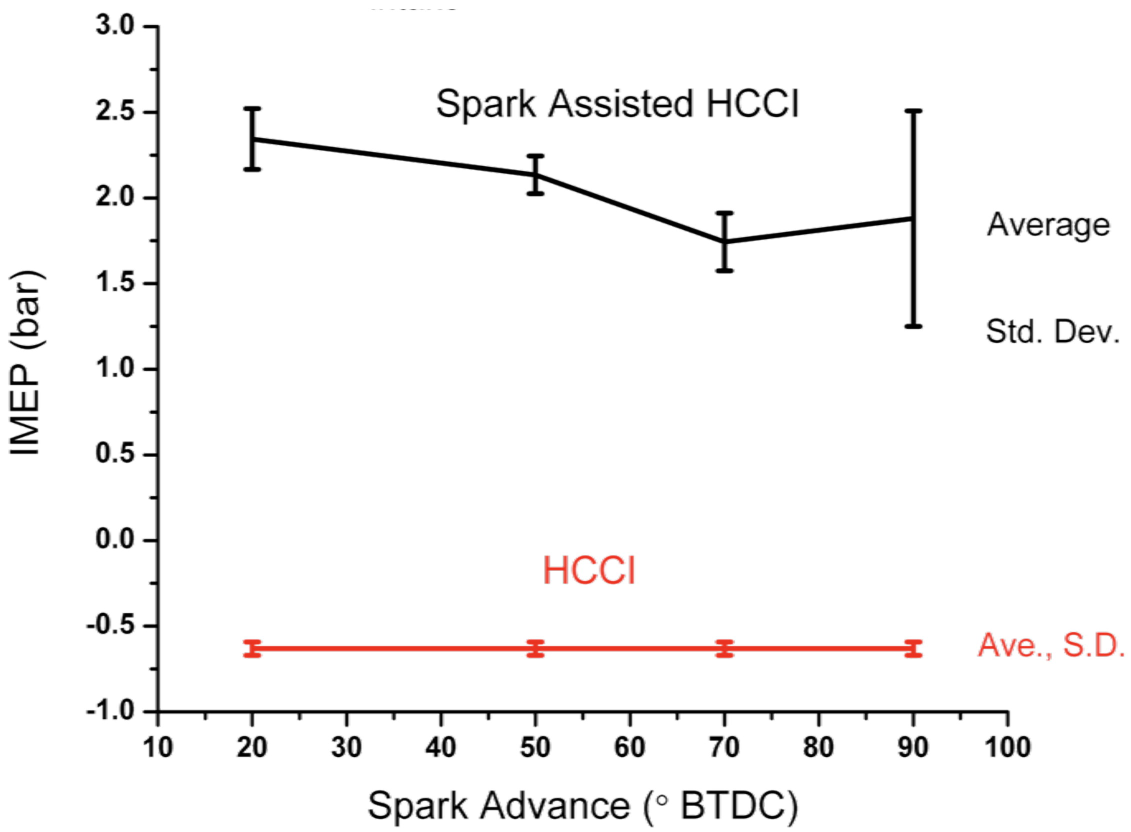

Figure 4.20: Plot of average net indicated mean effective pressure (IMEP) for HCCI versus spark assist at 20°, 50°, 70°, and 90° BTDC advance timing for $T_{int} = 270$ °C and $\phi = 0.62$, with indolene fuel. The error bars represent the standard deviation in IMEP for each engine operating condition. The HCCI operation is virtually identical to engine motoring data.

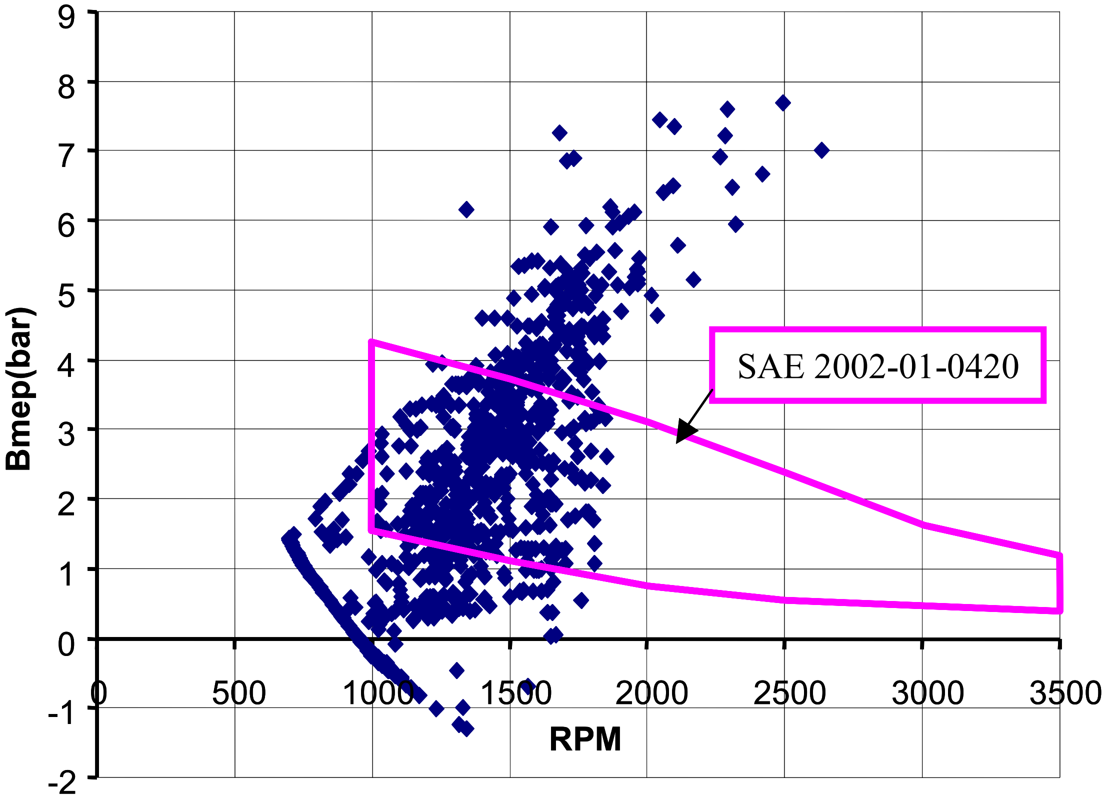

Figure 4.21: Plot of brake mean effective pressure (BMEP) versus engine speed, reproduced from Santoso et al. [3]. The plot shows the engine map for the U.S. Federal Testing Procedure (FTP) Urban Fuel Economy Driving Cycle for a mid-size vehicle. Santoso et al. superimposed the HCCI operating boundary according to Zhao et al. [4].

CHAPTER V

Conclusions and Recommendations for Future Work

5.1 Conclusions

Chapters III and IV each contained summaries and conclusions of the information presented therein. The major findings of this dissertation research are consolidated here. This research study prompted the development of a new single-cylinder optical engine research facility at the University of Michigan. The excellent optical access provided by this research engine combined with high-speed digital imaging offered critical insight into the fuel ignition behavior in a production-based combustion chamber when operated in an advanced low temperature combustion mode. The testbed allowed unique experiments, bridging low temperature combustion ignition studies to other devices such as the more idealized University of Michigan Rapid Compression Facility and full metal test engines.

The major findings of this research are:

1. The time-resolved imaging and pressure data clearly show that high heat release rates in HCCI combustion correlate to intense blue emission which occurs simultaneously throughout the volume of the combustion chamber. Lower rates of heat release are characteristic of blue emission that appears at local ignition sites

over longer time intervals within the combustion chamber. While the correlation between imaging and pressure data are not unexpected, the chemiluminescence imaging provided reaction information for very lean, low load conditions and misfire events which are below the threshold of pressure transducer measurements. Additionally, the imaging data show that while ignition is nearly homogeneous at strong HCCI conditions , at weak HCCI conditions reaction appears to propagate in well-defined reaction fronts.

2. Indolene and gasoline produced similar ignition and combustion phenomena, whereas iso-octane was markedly different. For example, the pump gasoline supported leaner HCCI operation than indolene. Iso-octane showed a dramatic transition into misfire and exhibited many sparse ignition events at low equivalence ratios (dropping from 40 bar peak cylinder pressures at $\phi = 0.68$ to peak cylinder pressure matching motoring engine conditions at $\phi = 0.61$). This was unexpected as iso-octane is considered a chemical surrogate for gasoline and under HCCI conditions, where kinetics are rate limiting, more similarities in ignition behavior were expected. Current theory could not have predicted the sensitivity nor magnitude of the iso-octane ignition and combustion behavior for lean mixtures in the optical research engine.

3. Ignition imaging show local hot zones result in preferential ignition sites for all of the fuels and equivalence ratios studied. This study demonstrates the value of ignition imaging when applying HCCI or other low temperature combustion control strategies, as a means to identify flow field or thermal features (such as non-uniformities or hot spots) which can significantly augment or hinder ignition control and engine performance.

4. Spark-assist has been demonstrated to stabilize HCCI combustion and to extend

lean operating limits. Spark assist clearly extends low load HCCI operation within acceptable engine operating metrics, such as rate of pressure rise and IMEP.

5. The imaging data show two distinct ignition regimes exist for spark assisted HCCI. One regime is typified by an initial local reaction zone formed around the spark plug, which accelerates subsequent compression ignition sites that consume the fuel charge. A second regime is typified by consumption of the fuel charge by radial reaction front propagation from the spark plug. The imaging data indicate the differences between the combustion events of these two regimes may impact emissions, which is not apparent from pressure transducer data.
6. Regions of high sensitivity of HCCI operation to spark assist are bounded by low and high preheat conditions. Within the temperature bounds, the effectiveness of spark assisted HCCI is a strong function of the equivalence ratio and spark timing. These studies show how spark assist advance timing can quickly be used (within a cycle) as a control parameter to increase IMEP for low load, lean conditions.

5.2 Recommendations for Future Work

The results of this work set many new research directions to expand our understanding of the fundamental chemical and physical mechanisms important during in-cylinder homogeneous charge combustion ignition and combustion and to further enable HCCI for practical applications. Although the focus of this work was on low load operation, the results of the parametric study can be applied to high load operation as well. For example, spark assist at high load will have similar limitations based on the thermal fields present in-cylinder. Thus, an important area for the next studies should include examining thermal charge stratification in conjunction with spark assist as a means to expand high load engine operation. Another area of considerable importance is in the application of spark assist in dynamic engine studies. Rapid transients may also benefit from spark assist in terms of fuel economy and stability.

One potential drawback of spark assisted HCCI operation is increased emissions, such as NO_x, due to the spark plasma and resulting combusiton. The impact of spark assist on HCCI NO_x and other exhaust gas emissions should be quantified. Additionally, this work used fixed spark plug energies. There are numerous studies in the literature examining the effects of spark plug properties on in-cylinder ignition. These studies can guide further research to improve the range and degree of control that can be achieved using spark assisted HCCI.

The results of the fuels studies demonstrated a large range of ignition behavior for three conventional reference fuels. The pressure to increase the use of biofuels in the transportation sector strongly motivates future work to examine the ignition properties of biofuels and biofuel blends with traditional fossil fuels at HCCI conditions.

APPENDICES

APPENDIX A

Optical Research Engine

A.1 Single Cylinder Research Engine Short Block Assembly

The optical research engine utilizes an FEV single cylinder research engine assembly foundation. Prof. Harold Schock (Michigan State Univeristy) generously provided a copy of the FEV user's manual for an identical assembly. This user's manual is included with the Optical Research Engine documentation.

A.2 Ford 1.25L Cylinder Head Assembly

The optical research engine is built around a Ford Zetec-SE 1.25 L engine configuration. This engine was originally built in Valencia, Spain for the 1997 Ford Fiesta (European). A modified production cylinder head is used, employing one of the four cylinders available. The aluminum cylinder head features fixed double-overhead cams timing 4 valves (twin ⌀26.1 mm intake, twin ⌀22.1 mm exhaust) around a centrally mounted spark plug. The cylinder head assembly was left intact as originally modified by Ford for use in the optical research engine assembly. A CD copy of the Ford of Europe service manual for a 1997 Ford Fiesta is included with the Optical

Research Engine documentation. This service manual includes cylinder head service procedures and assembly torques should the cylinder head assembly ever require repair.

A.3 Optical Engine Piston and Cylinder Assemblies

A.3.1 Piston and Rings

Ford supplied the optical research engine with two types of pistons: high ring-pack and low-ring pack. The high ring-pack piston is used for all experiments with a full cylinder liner, either coolant-jacketed or fused silica. The low ring-pack piston is used for all experiments with the partial fused silica cylinder liner, which prevents the piston rings from traversing the interface between the partial fused silica and partial coolant-jacketed cylinder liner assembly.

The same piston rings are used for either piston style. A twin narrow ring pair is used in the top ring land. A single ring is used in the second ring land (same width as the top ring land). Both the top ring pair and single second ring are loaded by a stainless steel ring expander placed inboard of the Torlon rings. A single tall Torlon ring is used in the bottom rider ring location (location of oil control rings of a conventional piston ring pack).

Both piston styles accept the same windows, which are either fused silica or aluminum.

A.3.2 Cylinder Assemblies

Three types of cylinder liners were supplied by Ford.

- coolant-jacketed full cylinder liner
- partial length coolant-jacketed cylinder liner which is used with partial upper (1 inch tall) fused silica cylinder liner
- fused silica full cylinder liner

APPENDIX B

Dynamometer and Supporting Facility

B.1 Dynamometer

The engine is driven by an Electro-Mechanical Associates Micro-Dyn 35 hydraulic dynamometer (built jointly with UM). Typical experiments held the engine speed constant at 700 RPM. The hydraulic dynamometer has an automatic control system to maintain set speed by compensating between providing a motoring load and absorbing net power output. The dynamometer uses a 25 HP electric motor driving a hydraulic pump. The hydraulic pump, in turn, drives a hydraulic motor connected to the engine flywheel. The hydraulic control system throttles the hydraulic motor signal to output the desired engine speed. The dynamometer uses a stand-alone computer to control the system. The dynamometer is cooled by a chilled water cooling system, fed by the laboratory building facilities. Chilled water temperature is typically held between 45-50 °F; this keeps dynamometer hydraulic fluid temperatures low. The dynamometer hydraulic components are generally held just slightly over 100 °F.

The dynamometer control system also drives a stepper motor which was originally tied to intake throttle plate. The use of this stepper motor was discontinued in the present work when high intake temperatures were necessary for certain HCCI operating conditions. The high intake temperatures caused the stepper motor to fail, and it has not been replaced at the present time.

B.2 Lubrication System

The lubrication system is comprised of a three stage belt-driven external oil pump. Two stages of the pump are scavenging stages. The scavenging feeds collect oil from the dry sump, into which the lower engine assembly and cylinder head drains. The scavenging pumps transfer oil to the storage tank. The tank has a temperature dial gauge and a resistive heater, which is used only on system warm-up to help bring initial oil temperature up to 60 °C. The tank has an oil level sight gauge, anti-aeration baffles, a system drain, and a vent line leading to a separate oil/air separator venting to atmosphere. The oil/air separator has a drain at the bottom, which should be periodically checked and emptied (but the system works well and has never required draining to date). The reservoir tank has a return line to the third stage of the oil pump, which pressurizes oil for the engine. Pressurized oil is passed in a T-junction to a pressure accumulator (with manual valve), and onto a filter assembly. The oil is then fed to the lower end of engine and up to the cylinder head assembly. Oil pressure gauges are located downstream of the filter and at the feed to the cylinder head assembly. Oil pressure is typically held at 40 psi minimum. Mobil−1 10W−30 synthetic oil is used. A vacuum pump is used to draw slight sub-atmospheric pressure on the crankcase to prevent the engine from pumping oil past the piston rings on the primary piston. Oil passed through these rings will splash onto the imaging mirror assembly.

The pressure accumulator is used to prime the lubrication system upon engine start with the dynamometer, to protect the bearing surfaces. The manual valve is opened just as the dynamometer begins to spin the engine. The valve is left open while the engine runs, and dampens oil pressure pulsations from the pump. The valve is closed just before the dynamometer is shut down to capture pressurized oil for the next start cycle. Air pressure on the top side of the oil pressure accumulator should not require adjustment. The lubrication system does not have active chilled water cooling, as this has not been required up to date. A box fan has been used to provide convective cooling from the oil reservoir tank, and this has been sufficient to date. If the oil temperature is allowed to go much beyond 60 °C, the oil thins to the point where the scavenging pumps cannot effectively drain the engine sump at 700 RPM motoring speeds. Oil may then accumulate in the sump, be aerated by the crank, and eventually be pulled by the crankcase vacuum pump. A sight window on the engine sump allows the oil level to be monitored. If oil level begins to increase, the engine can be motored at a slightly faster speed until the scavenging pumps clear the sump. This has only been a problem with low engine speeds and hot oil.

B.3 Coolant System

The coolant system is comprised of a 240V 3−phase AC centrifugal pump flowing a 50% green Prestone coolant, 50% distilled water mixture through the lower engine assembly, up through the jacketed cylinder liner (when used) and the cylinder head assembly, up through a sight glass indicator to the reservoir tank. The reservoir tank has a 240V 3−phase AC Chromalox resistive immersion heater, thermometer, pressure gauge, and pressure relief cap flowing to a reservoir bottle. The reservoir tank returns to the circulating pump. A system drain is located at the pump. The coolant system heater has a dial temperature setting it it, with a marker for a typical 90 °C coolant setting. The coolant system does not have active cooling capability, but this has not been necessary to date. The system radiates and convects enough heat loss to dissipate combustion energy losses and still maintain a fairly constant coolant temperature.

B.4 Fuel Handling System

Fuel is fed to the fuel injector rail by a dead-headed pressure delivery system. Fuel pressure is delivered by a hydraulic accumulator (Tobul EBR20−60−S/021701), which uses a Viton bladder pressurized by nitrogen. The Viton bladder is replaceable. Fuel is added to the system via a safety can and filter, via a vacuum pump applied to the gas side of the accumulator bladder. Fuel pressure is generally held at 25 psi (1.7 atm) for the present work, controlled by the regulator on the nitrogen gas cylinder. Fuel is fed to the Siemens DEKA II center-feed dual conical jet injector at rail pressure. A dial pressure gauge is mounted downstream of the hydraulic accumulator and feed filter, upstream of the fuel rail entry. The fuel injector rail has a Ford production pressure regulator on the downstream end. This fuel rail was originally a return-type fuel system in Ford's production application; it originally used vacuum reference. The vacuum reference is disabled, which results in the regulator diaphragm and spring lifting off at about 40 psi. Higher fuel pressures open the pressure regulator, so a safety catch bottle is used to catch expelled fuel. This feature is useful when purging the fuel system for fuel changeovers.

B.5 Spark and Fuel Controller

A Magnatek Engine Control Module (ECM) spark and fuel injection controller is integrated with the dynamometer. Fuel equivalence ratio was controlled by varying the fuel injector driver pulse width duration, holding fuel rail pressure constant. The ECM controls both fuel injection timing (with respect to TDC of the compression stroke) and duration. The fuel injection timing signal recorded by the rising edge of the 5V DC signal to the fuel injector driver circuit. The ECM is capable of driving a second fuel injector (protecting for the option of adding another fuel injector to the system, such as one much further upstream in the intake).

The ECM also controls spark ignition timing by controlling the driver voltage to the primary windings on the ignition coil. Spark ignition timing is recorded as the falling edge of the 5V DC signal to the ignition coil driver. Collapse of current driving the primary windings induces a high voltage in the secondary coil, energizing the spark plug. The ignition system uses a Wells DR100 control module and a Wells C839 ignition coil.

The ECM was built with the option of burst firing for a programmed length of time (not set cycles), allowing fuel and spark to be toggled on and off for extended running without damaging the optical components. This feature was not used in the present work. Spark ignition was toggled on and off for spark-assisted HCCI via a switch spliced into the coil primary winding circuit.

A CD copy of the ECM software is included with the Optical Engine Facility documentation.

B.6 Intake and Exhaust

The intake manifold has an auxiliary resistive tape heater wrapped around it, upstream of the fuel injector and downstream of the throttle body. This heater is controlled by a Variac, set at the maximum setting allowed for the heater. The intake manifold also incorporates a 1.4 kW heater installed upstream of the throttle body (added after the throttle body was originally installed in the facility). This heater is also controlled by a Variac, which is adjusted to provide various intake air temperatures. A K−type thermocouple is installed in the intake manifold about 1 inch upstream of the fuel injector. An Omega mass air meter was installed upstream of the 1.4 kW heater, but was not utilized in the present work. A HEPA filter is fitted upstream of the mass air meter to protect it. The intake system was originally planned to have a large expansion chamber fitted upstream, but this feature was not completed in the present work.

The exhaust manifold contains several ports, including an exhaust K−type thermocouple, a port for the lambda meter's Bosch O_2 sensor, and extra sampling ports. A fixed orifice was fitted to the end of the exhaust manifold to help reduce the sub−atmospheric pressure draw from the facility exhaust duct system (required from a laboratory safety standpoint). The exhaust system was also originally planned to have a large expansion chamber fitted downstream, but this feature was not completed in the present work.

APPENDIX C

Data Acquisition

Data acquisition was performed using a National Instruments Compact Data Acquisition (cDAQ). This Universal Serial Bus based system recorded temperature readings at the beginning of each experiment, then recorded all digital and analog channels at 100 kHz, using a LabView software code. More details regarding the cDAQ system and LabView code are included in Appendix C.

C.1 cDAQ System

The National Instruments compact data acquisition system (cDAQ) is shared with the Rapid Compression Facility (RCF). The RCF and optical engine facility cannot be recorded simultaneously, but they are set up independently and do not require swapping out cables to record data. The cDAQ system records both analog and digital signals, as programmed via LabView. The following table defines optical engine cDAQ input / output recorded and configured for LabView:

C.2 LabView

Steve Walton wrote the LabView code used with the cDAQ for the optical engine research facility. The most recent version of the software is file ”Brad - DAQ -

cDAQ Slot	Device	Signal	Channel	Card Assignments	Signal Cable
Slot 2	9206 Differential Analog	Cylinder Pressure	0	AI0= +, AI8= −	blue / blue
Slot 2	9206 Differential Analog	Intake Pressure	1	AI1= +, AI9= −	red / blue / red
Slot 2	9206 Differential Analog	Lambda Meter	2	AI2= +, AI10= −	red / blue / yellow
Slot 2	9206 Differential Analog	EMPTY	3	AI3= +, AI11= −	red / blue / orange
Slot 3	9401 Digital Input	CAD	0	N/A	red / red / red
Slot 3	9401 Digital Input	TDC	1	N/A	red / red / orange
Slot 3	9401 Digital Input	Fuel Injector Driver	2	N/A	red / red / yellow
Slot 3	9401 Digital Input	Ignition Coil Primary	3	N/A	red / red / green
Slot 3	9401 Digital Input	Camera Trigger	4	N/A	white / yellow / green
Slot 4	9401 Digital Output	CAD	2	N/A	red / red / white
Slot 4	9401 Digital Output	CAD	2	N/A	white / yellow / green
Slot 6	9211 Thermocouple	Ambient	0	N/A	yellow thermocouple
Slot 6	9211 Thermocouple	Intake Air	1	N/A	red / white / green
Slot 6	9211 Thermocouple	Coolant Into Cyl. Head	2	N/A	red / white / blue
Slot 6	9211 Thermocouple	Oil In	3	N/A	red / white / orange

109.vi". The code captures the thermocouple data once, at the beginning, for each recorded session. All other analog and digital input data is recorded at 60 kHz for the duration input in LabView. Most experiments for the present work were recorded for 5 or 10 seconds.

C.3 Pressure Transducers

Cylinder pressure is measured using a piezoelectric transducer (Kistler 6125A, serial 644106) and charge amplifier (Kistler 5010B).

Intake pressure is measured with an absolute pressure sensor in a water cooled fitting (Kistler 4045A2, serial 1496849 with Kistler 4618 amplifier). The water cooled fitting is fed the chilled water system, which is necessary for the intake pressure sensor to protect it against high intake temperatures. As documented in the Matlab data processing code, an offset was later applied to the intake pressure measurements. The subtraction of 8% in the intake pressure is due to the intake pressure transducer / amplifier combination reading reading 8% high at approximately 1 bar when compared to the Kistler 4045A5 used in the Rapid Compression Facility (RCF), a barometer used in Jim Wiswall's experiments, and both Varian transducers from the RCF sampling room conditions. While this error was not verified over the entire range of the optical engine intake pressure sensor, all engine intake conditions are at about 1 bar, so an 8% reduction is used. It is believed the Kistler A4045A2 sensor may have damaged at some point in the past.

Pressure data were not filtered prior to recording.

C.4 Lambda Meter

Equivalence ratio is measured in the exhaust manifold using an ETAS LA4 lambda meter utilizing a Bosch broadband LSU 4.9 lambda sensor. The lambda meter calculates equivalence ratio based on the O_2 content of the exhaust stream, given the following inputs:

- fuel H/C ratio
- fuel O/C ratio
- fuel H_2O component
- stoichiometric air / fuel mass ratio

Since the lambda meter falsely reads excess exhaust O_2 due to incomplete combustion and misfire as a mixture leaner than actual, some procedural development was required. For each intake temperature, a series of experiments were conducted to map out the relationship between fuel pulse width and the ETAS LA4 lambda meter's interpretation of equivalence ratio. For lean mixtures which resulted in incomplete combustion in HCCI mode, advanced spark ignition was used to provide more complete combustion in these trials. The equivalence ratio for that more complete combustion condition was then used as a reference for that particular fuel pulse width / intake temperature combination. This procedure helped correct readings for most lean mixtures. Corrections for very lean conditions were estimated by interpolation from other conditions.

The lambda meter must be programmed for each fuel used; instructions are given in the ETAS Lambda Meter LA4 instruction manual (included in the Optical Engine Facility reference file). The following programming settings were used:

Fuel	H/C ratio	stoich A/F mass ratio	H_2O component	O/C ratio
Indolene	1.762	14.41	0	0
Iso-octane	2.25	15.10	0	0
Gasoline	1.85	14.53	0	0

The lambda meter is powered from a Pyramid PS-14KX 13.8V, 12A DC regulated power supply. The lambda meter should not be powered up unless the engine is already motoring and flowing air past the sensor (to help with regulation of the sensor internal heater). The lambda meter output is a 0-15V DC analog signal to the cDAQ (clipped at 8V DC).

C.5 High-Speed Digital Camera

The combustion chamber was imaged through the piston window using a high-speed color digital video camera (Vision Research Phantom v7.1, color). The camera is capable of 800 x 600 pixel spatial resolution, and reduced resolution frame rates up to 160 kHz. A fast 50 mm lens (f/0.95 Nikor TV lens) and C-mount extension tubes are used with the camera to adjust the focal length and to reduce the focal depth along the cylinder axis. A neutral-density filter was installed onto the Nikor lens to protect it. A Lexan sheet was also placed between the optical engine piston−axis mirror and the Nikor lens to help protect the lens from damage.

In this study, the camera was focused at a plane coinciding with the spark plug ground electrode for all piston window imaging experiments. The camera settings were generally fixed at 320 x 320 pixels for piston window imaging (or 640 pixels wide x 480 pixels high for orthogonal cylinder liner imaging) at 3000 frames per second (fps) with 309 μs exposure time. The camera sensor array was calibrated according to the procedure outlined in Walton et al. [9].

The imaging study along the orthogonal axis to the piston was conducted with a similar experimental set-up. A shorter coolant-jacketed steel cylinder liner was used under a mating section of fused silica cylinder liner. The transparent portion of the cylinder allowed orthogonal viewing access from the cylinder head deck surface to 25 mm below the deck surface. Another flat piston was also used with this engine configuration, with the piston ring pack lowered to prevent the piston rings from traversing the steel cylinder/fused silica cylinder transition. Although it was not used for imaging, the piston held the same fused silica window to maintain similar piston heat transfer rates between experiments. The same color digital video camera was used as for the axial imaging with different C-mount extension tubes to adjust the focal length and depth. The camera was focused in a plane coinciding with the back side of the open intake valves, since the spark plug ground electrode is not visible (it protrudes to a depth 5 mm above the deck surface). The camera settings were fixed at 640 pixels wide x 480 pixels high at 3000 frames per second (fps) with 309 μs exposure time (the same frame rate and exposure as used in the piston view studies). The camera sensor array was also calibrated according to the procedure outlined in Walton et al. [9].

All imaging data were processed using Vision Phantom v607 (3823.stg) software.

C.6 Crank Angle Encoder

Crank angle is encoded with a BEI encoder at 360 signal cycles per revolution, with a secondary channel output signaling TDC. The BEI encoder was supplied along with the optical engine by Ford. It is model number:

H20EB−37−F12−SS−360−ABZC−26LS31−SCS24−5V−S and serial number X0043762. The encoder outputs a digital square wave at 360 cycles per crank revolution. Each output cycle contains a 5V DC full square wave profile, split high and low half-way through the cycle. This effectively provides 0.5 CAD resolution encoding. The encoder also outputs a short 5V DC digital narrow square "spike" at TDC, which is used for a reference marker for most data post-processing. The encoder is clamped onto the engine crankshaft at the front of the engine. Alignment of the encoder to engine TDC is critical, and was set using a specialized electronic calibration device loaned by Dr. Steve Wooldridge from Ford Motor Company. This device must be used again if the encoder is ever disassembled from the engine crankshaft. To set engine TDC, a an adjustable reference tool is inserted in place of the spark plug to determine mechanical piston top dead center (within the tolerance of crank bearings, piston pin clearance, etc.). This tool is included with the Optical Engine Facility toolkit.

C.7 Thermometry

Omega K-type thermocouples are installed to monitor the following:

- fuel temperature upstream of the fuel rail
- dynamometer hydraulic motor surface temperature
- coolant temperature going into the FEV lower engine assembly
- coolant temperature entering the cylinder head (cDAQ)
- coolant temperature exiting the cylinder head
- oil temperature going into the FEV lower engine assembly (cDAQ)
- oil temperature going to the cylinder head
- intake air temperature (cDAQ)

- exhaust air temperature

APPENDIX D

Data Processing

D.1 MATLAB code for processing experimental data

```
% This program is used to process the cDAQ data from the optical engine
% Written by Bradley T. Zigler, bzigler@umich.edu, 2007/10/11
% Adapted from code "readfile_prelim.m" which was
% written by Stephen M. Walton, smwalton@umich.edu, 2007/01/12
% Modified by Kyeongmin Kim, kyekim@umich.edu, 2007/12
% Modified by Bradley T. Zigler, bzigler@umich.edu, 2008/01/28
% Modified by Stepehn M. Walton and Bradley T. Zigler, 2008/02/06-8
% Modified by Bradley T. Zigler, February 2008
% Modified by Kyeongmin Kim, 2008/03/14 to calculate IMEP
% Modified by Bradley T. Zigler, 2008/04/06 for Mike Hoppe and Smitesh
% Bakrania sensor testing
% Modified by Bradley T. Zigler, 2008/05/02 to combine with Kyeongmin's
% 2008/03/04 version to include IMEP calculations and all plotting
%
%%%%%%%%%%%%%%%%%%%%%%%%%%%%%%%%%%%%%%%%%%%%%%%%%%%%%%%%%
%%%%%%%%%% engine_data_analysis_2008_05_03.m %%%%%%%%%%%%
%%%%%%%%%%%%%%%%%%%%%%%%%%%%%%%%%%%%%%%%%%%%%%%%%%%%%%%%%
clear all;
clc


%%%%%%%%%%%%%%%%%%%%%%%%%%%%%%%%%%%%%%%%%%%%%%%%%%%%%%%%%%%%%%%%%%%%%%%%%%%
%%%%%%   SET Filename, Charge Pressure, Amp Value       %%%%%%%%%%%%%%%%%%%
%%%%%% Change the following filename to input the desired raw data file
inputfilename = sprintf('2008_04_27_15_01_Engine.dat');
AMP = 50; %Measurement Unit reading off amplifier
Calibration = 1.081; %Calibration constant for Cyl P transducer
Scale = 1.08; %Scale should match calibration to 3 sig figs to output psi
%%%%%%%%%%%%%%%%%%%%%%%%%%%%%%%%%%%%%%%%%%%%%%%%%%%%%%%%%%%%%%%%%%%%%%%%%%%
Cycle_no_cut = 1;  % Set this value to cut data into "A" and "B" segments,
                    % at beginning of Spark Assist
                    % Determine this number from pressure trace or if
                    % necessary, imaging (where spark is seen)
                    % This is used in calculating statistics, visually
                    % distinguishing plots, and creating output files of
                    % pressure data for use outside this code

cycle_pick = 5;  % This is the individual cycle which will be plotted for P

%%%%%% Define the column variables %%%%%%%%%%%%%%%%%%%%%%%%%%%%%%%%%%%%%%%%
cDAQ = dlmread(inputfilename);
Room_Temperature=cDAQ(1,1); %Degrees Celsius
Intake_Temperature=cDAQ(2,1); %Degrees Celsius
Coolant_Temperature=cDAQ(3,1); %Degrees Celsius
Oil_Temperature=cDAQ(4,1); %Degrees Celsius
cDAQ = cDAQ(5:size(cDAQ),:); %Cut off temperature rows
[l w]=size(cDAQ); %Find size of array
```

```
Cyl_P_voltage=cDAQ(:,1); %Voltage from Cyl Pres amplifier
Cyl_P_voltage=smooth(Cyl_P_voltage,29,'moving');
Int_P_voltage=cDAQ(:,2); % Voltage from Int Pres amplifier
Int_P_voltage=smooth(Int_P_voltage,29,'moving');
Lambda_voltage=cDAQ(:,3); %Voltage from lambda meter
Dummy=cDAQ(:,4); %Unused cDAQ column
CAD_encoder=cDAQ(:,5); %CAD encoder digital signal
TDC_encoder=cDAQ(:,6)/2; %TDC encoder digital signal (rising edge)
Fuel_signal=cDAQ(:,7)/4; %Fuel injector driver digital (rising edge)
Spark_signal=cDAQ(:,8)/8; %Coil driver signal (falling edge)
Camera_Trigger=cDAQ(:,9)/16; %Digital output signal (rising edge)
% Test_Time is based on 60 kHZ sampling rate
Test_Time=(0:(1/60):(l-1)*(1/60))'; %Converts row spacing to milliseconds

%%%%%%%%%%   ADJUST FOR AMPLIFIER VALUE       %%%%%%%%%%%%%%%%%%%%%%%%%%%%%
Cyl_P_uncorrected = Cyl_P_voltage*AMP*Scale/Calibration*0.06895; %Bar
% 0.06895 bar / psi
%%%%%%%%%%%%%%%%%%
% The subtraction of 8% in the intake pressure is due to the intake
% pressure transducer (Kistler 4045A2, serial 1496849, Kistler amp 4618A0).
% This sensor/amp reads 8% high at ~1 bar when compared to Steve's 4045A5,
% Jim's barometer, and both Varian transducers from the RCF sampling room
% conditions.  I have not checked the error over the entire range, but all
% engine intake conditions are at about 1 bar, so an 8% reduction is used.
%%%%%%%%%%%%%%%%%%
Int_P = Int_P_voltage * 2/10 *0.92; %0-2 bar range @ 0-10 volts
%%%%       PLOT RAW DATA      %%%%%%%%%%%%%%%%%%%%%%%%%%%%%%%%%%%%%%%%%%%%
figure(1)
[AX,plot1,plot2] = plotyy(Test_Time,Camera_Trigger,...
                             Test_Time,Cyl_P_uncorrected,'plot');
title(inputfilename,'Interpreter','none');
xlabel('Time (ms)');
set(plot1,'Color','r');
set(get(AX(1),'Ylabel'),'String','Camera Trigger [digital]','Color','r');
set(AX(1),'YLim',[-.5 1.5]);
set(AX(1),'YTick',[-10:.5:-11],'Ycolor','r');
set(plot2,'Color','b');
set(get(AX(2),'Ylabel'),'String','Uncorrected Cylinder Pressure [bar]','Color','b');
set(AX(2),'YLim',[-5 max(Cyl_P_uncorrected*1.25)]);
set(AX(2),'YTick',[-5:5:max(Cyl_P_uncorrected*1.25)],'Ycolor','b');

%Count number of TDC marker, from rising edge of signal
% for loop used to find size of array needed to track location of TDC
% markers
CAD=ones(l,1);
TDC_no=0;
for j=1:l-1
    if TDC_encoder(j)<TDC_encoder(j+1)
        TDC_no=TDC_no+1;
    end
end

%Mark row number of TDC marker
TDC_marker=zeros(TDC_no,1);
TDC_no=0;
for j=1:l-1   % j is the index of the data file
    if TDC_encoder(j)<TDC_encoder(j+1)  % looks for rising edge of TDC_encoder (digital)
        TDC_no=TDC_no+1; % TDC_no is the index of TDC_marker
        TDC_marker(TDC_no,1)=j+1;  %TDC_marker is a vector showing the indicies where rising edges are
        CAD(j+1)=360;  % assigns CAD = 360 only at TDC markers, all else are ones
    end
end

%Count number of cycles by checking pressure at TDC markers and comparing
%to pressure at following TDC, determining whether TDC is exhaust or firing
% for loop used to find size of array needed to track location (row number) of TDC
% markers of cycle start and end
Cycle_no=0;
for j=1:TDC_no-2;
    if Cyl_P_uncorrected(TDC_marker(j))<Cyl_P_uncorrected(TDC_marker(j+1))...
            && Cyl_P_uncorrected(TDC_marker(j+1))>Cyl_P_uncorrected(TDC_marker(j+2))
        Cycle_no=Cycle_no+1;
    end
end

%Mark row number of beginning of each cycle to track location (row number) of TDC
% markers of cycle start and end
Cycle_marker=zeros(Cycle_no+1,1);
Cycle_no=0;
for j=1:TDC_no-2;
```

```
    if Cyl_P_uncorrected(TDC_marker(j))<Cyl_P_uncorrected(TDC_marker(j+1))...
            && Cyl_P_uncorrected(TDC_marker(j+1))>Cyl_P_uncorrected(TDC_marker(j+2))
        Cycle_no=Cycle_no+1;
        Cycle_marker(Cycle_no,1)=TDC_marker(j); %Bound beginning of cycle
        Cycle_marker(Cycle_no+1,1)=TDC_marker(j+2); %Bound end of cycle
    end
end

%Set the CAD = 0 at the beginning of each cycle
for j=1:Cycle_no+1;
    CAD(Cycle_marker(j))=0;
end

%Calculate CAD
for j=TDC_marker(1):TDC_marker(TDC_no);
    for k=1:TDC_no-1;
        if j>TDC_marker(k) && j<TDC_marker(k+1) %Look between TDC markers
            CAD(j)=CAD(j-1)+360/(TDC_marker(k+1)-TDC_marker(k)); %Set CAD based on time
                                                                 %between TDC markers spread over 360 degrees
        end
    end
end

%Create empty vector set for corrected cylinder pressure
Cyl_P_corrected=ones(1,1);
for i=1:Cycle_no; %Loop through all cycles
    for j=Cycle_marker(i):Cycle_marker(i+1); %Look within individual cycle
        if CAD(j)<=180 && CAD(j+1)>180; %Look for BDC to determine where to take offset
            k=j; %Define BDC at intake
        end
    end
    for j=Cycle_marker(i):Cycle_marker(i+1); %Define and apply offest within individual cycle
        Cyl_P_corrected(j)=Int_P(k)-Cyl_P_uncorrected(k)+...
            (Int_P(k+1)-Int_P(k)-Cyl_P_uncorrected(k+1)+...
            Cyl_P_uncorrected(k))*(180-CAD(k))/(CAD(k+1)-CAD(k))+...
            Cyl_P_uncorrected(j);  %The center portion of this equation does an average between
                                   %two data points, since the exact 180
                                   %degrees (BDC) point falls between them.
                                   % This portion of the calculation really
                                   % makes no difference (because of the
                                   % running average being used), but is
                                   % good practice.
    end
end




% for j=1:TDC_no;
%     if TDC_marker(j)==Cycle_marker(Cycle_no);
%         Cycle_end=TDC_marker(j+2);
%     end
% end


%Calculate dP/dt [bar/s]
Dpdt=zeros(1,1); %Create column vector, fill with zeros
for j=Cycle_marker(1):Cycle_marker(Cycle_no+1);
    Dpdt(j)=(Cyl_P_corrected(j+1)-Cyl_P_corrected(j))*60*1000; %Using 60 kHz sampling
end



%Input information used in apparent heat release calculation
Bore = 71.9;                        %Bore [mm]
Stroke = 76.5;                      %Stroke [mm]
CR = 10;                            %Compression Ratio (assumed CR, based on Ford production published CR)
Con_Rod_R = 4;                      %Ratio of connecting rod to crank radius (assumption, based on Heywood)
                                    % this value is typically between 3-4
                                    % for small-medium SI engines
Gamma = 1.35;                       %Ratio of specific heats, assumed based on Heywood
                                    % will revise code to calculate gamma
                                    % based on fuel & equivalence ratio

a=Stroke/2;                         %Crank Radius [mm]
Con_Rod_length=a*Con_Rod_R;         %Connecting Rod length[mm]
Disp_Vol=pi/4*Bore^2*Stroke/1e6;    %Displacement Volume[Liter]
Clear_Vol=Disp_Vol/(CR-1);          %Clearance Volume[Liter]

%Distance between the crank axis and the piston pin axis
```

```
s=a*cosd(CAD)+sqrt(Con_Rod_length^2-a^2*(sind(CAD)).^2);
%Cylinder Volume[L]
Cyl_Vol=Clear_Vol+pi*Bore^2/4*(Con_Rod_length+a-s)/1e6;

%Calculate dV/dt[Liter/s]
DVdt=zeros(l,1);
for j=Cycle_marker(1):Cycle_marker(Cycle_no+1);
    DVdt(j)=(Cyl_Vol(j+1)-Cyl_Vol(j))*60*1000;
end

%Apparent Heat Release rate[bar*Liter/s]=>[kW]
% Conversion from [bar*Liter/s] to [kW] requires *100 to get into [W], then
% divide by 1000 to get into [kW]
Dqdt=(Gamma/(Gamma-1)*Cyl_P_corrected.*DVdt+1/(Gamma-1)*Cyl_Vol.*Dpdt)*100/1000;



%Calculate Apparent Heat Release Rate as function of crank angle
%Calculate dP/dtheta [bar/CAD]
Dpdtheta=zeros(l,1); %Create column vector, fill with zeros
for j=Cycle_marker(1):Cycle_marker(Cycle_no+1);
    Dpdtheta(j)=(Cyl_P_corrected(j+1)-Cyl_P_corrected(j))/(CAD(j+1)-CAD(j));
end



%Calculate dV/dtheta[Liter/CAD]
DVdtheta=zeros(l,1);
for j=Cycle_marker(1):Cycle_marker(Cycle_no+1);
    DVdtheta(j)=(Cyl_Vol(j+1)-Cyl_Vol(j))/(CAD(j+1)-CAD(j));
end

%Heat Release rate[J/CAD]
% Conversion from [bar*Liter/s] to [kW] requires *100 to get into [J/CAD]
Dqdtheta=(Gamma/(Gamma-1)*Cyl_P_corrected.*DVdtheta+1/(Gamma-1)*Cyl_Vol.*Dpdtheta)*100;

% %Separate corrected cylinder pressure related data into series "A" and "B"
% Cyl_P_corrected_A = Cyl_P_corrected(1:Cycle_marker(Cycle_no_cut));
% Cyl_P_corrected_B = Cyl_P_corrected(Cycle_marker(Cycle_no_cut)+1:length(Cyl_P_corrected));
% CAD_A = CAD(1:Cycle_marker(Cycle_no_cut));
% CAD_B = CAD(Cycle_marker(Cycle_no_cut)+1:length(Cyl_P_corrected));
% Dpdt_A = Dpdt(1:Cycle_marker(Cycle_no_cut));
% Dpdt_B = Dpdt(Cycle_marker(Cycle_no_cut)+1:length(Cyl_P_corrected));
% Dqdt_A = Dqdt(1:Cycle_marker(Cycle_no_cut));
% Dqdt_B = Dqdt(Cycle_marker(Cycle_no_cut)+1:length(Cyl_P_corrected));
% Dpdtheta_A = Dpdtheta(1:Cycle_marker(Cycle_no_cut));
% Dpdtheta_B = Dpdtheta(Cycle_marker(Cycle_no_cut)+1:length(Cyl_P_corrected));
% Dqdtheta_A = Dqdtheta(1:Cycle_marker(Cycle_no_cut));
% Dqdtheta_B =
% Dqdtheta(Cycle_marker(Cycle_no_cut)+1:length(Cyl_P_corrected));

%%%%%%%%%%%%%%%%%%%%%%%%%%%%%%%%%%%%%%%%%%%%%%%%%%%%%%%%%%%%%%%%%%%%%%%%%%%%%%%
%%%%%%%%%%% Calculate statistics
%%%%%%%%%%% %%%%%%%%%%%%%%%%%%%%%%%%%%%%%%%%%%%%%%%%%%%%%%%%%%%%%%%%%%%%%%%%%%%

%Initializing array for the following values
output_A = zeros(Cycle_no_cut+3,12);
% Column 1 = cycle number
% Column 2 = max corrected cylinder pressure
% Column 3 = CAD location of max corrected cylinder pressure
% Column 4 = max dP/dt
% Column 5 = CAD location of max dP/dt
% Column 6 = max dQ/dt
% Column 7 = CAD location of max dQ/dt
% Column 8 = max dP/dtheta
% Column 9 = CAD location of max dP/dtheta
% Column 10 = max dQ/dtheta
% Column 11 = CAD location of max dQ/dtheta
% Column 12 = IMEP
for j=1:Cycle_no_cut-1;
    % Sequence through each cycle
    output_A(j,1)=j;
    Ind_Work=0;
    % Find maximum corrected cylinder pressure for each cycle
    % When max pressure is found, also record CAD location
    for k=Cycle_marker(j):Cycle_marker(j+1);
        % Sequencing from beginning TDC to end TDC by array index (stepping
        % in ones)
        if output_A(j,2)<Cyl_P_corrected(k);
            output_A(j,2)=Cyl_P_corrected(k);
```

```
            output_A(j,3)=CAD(k);
        end
        % Find maximum dP/dt, looking only from TDC +/- 50 CAD
        % When max dP/dt is found, also record CAD location
        if CAD(k)>=310 && CAD(k)<=410;
            if output_A(j,4)<Dpdt(k);
                output_A(j,4)=Dpdt(k);
                output_A(j,5)=CAD(k);
            end
        end
        % Find maximum dP/dtheta, looking only from TDC +/- 50 CAD
        % When max dP/dtheta is found, also record CAD location
        if CAD(k)>=310 && CAD(k)<=410;
            if output_A(j,8)<Dpdtheta(k);
                output_A(j,8)=Dpdtheta(k);
                output_A(j,9)=CAD(k);
            end
        end
        % Find maximum dQ/dt, looking only from TDC +/- 100 CAD
        % When max dQ/dt is found, also record CAD location
        if CAD(k)>=260 && CAD(k)<=460;
            if output_A(j,6)<Dqdt(k);
                output_A(j,6)=Dqdt(k);
                output_A(j,7)=CAD(k);
            end
        end
        % Find maximum dQ/dtheta, looking only from TDC +/- 100 CAD
        % When max dQ/dtheta is found, also record CAD location
        if CAD(k)>=260 && CAD(k)<=460;
            if output_A(j,10)<Dqdtheta(k);
                output_A(j,10)=Dqdtheta(k);
                output_A(j,11)=CAD(k);
            end
        end
        % Calculate indicated work [bar * Liter]by integrating cylinder pressure
        Ind_Work=Ind_Work+Cyl_P_corrected(k)*(Cyl_Vol(k+1)-Cyl_Vol(k));
    end
    % Calculate IMEP [bar]
    output_A(j,12)=Ind_Work/Disp_Vol;
end

% Calculate statistics for max P, max dP/dt, max dQ/dt, max dP/dtheta, max dQ/dtheta over entire data set
% also calculate statistics for CAD locations of these paratmeters
for j=2:12;
    output_A(Cycle_no_cut+1,j)=mean(output_A(1:Cycle_no_cut-1,j));
    output_A(Cycle_no_cut+2,j)=std(output_A(1:Cycle_no_cut-1,j));
    output_A(Cycle_no_cut+3,j)=output_A(Cycle_no_cut+2,j)/output_A(Cycle_no_cut+1,j);
end

%Initializing array for the following values
output_B = zeros((length(Cycle_marker)-Cycle_no_cut+4),12);
% Column 1 = cycle number
% Column 2 = max corrected cylinder pressure
% Column 3 = CAD location of max corrected cylinder pressure
% Column 4 = max dP/dt
% Column 5 = CAD location of max dP/dt
% Column 6 = max dQ/dt
% Column 7 = CAD location of max dQ/dt
% Column 8 = max dP/dtheta
% Column 9 = CAD location of max dP/dtheta
% Column 10 = max dQ/dtheta
% Column 11 = CAD location of max dQ/dtheta
% Column 12 = IMEP
for j=Cycle_no_cut:Cycle_no;
    % Sequence through each cycle
    output_B(j-Cycle_no_cut+1,1)=j;
    Ind_Work=0;
    % Find maximum corrected cylinder pressure for each cycle
    % When max pressure is found, also record CAD location
    for k=Cycle_marker(j):Cycle_marker(j+1);
        % Sequencing from beginning TDC to end TDC by array index (stepping
        % in ones)
        if output_B(j-Cycle_no_cut+1,2)<Cyl_P_corrected(k);
            output_B(j-Cycle_no_cut+1,2)=Cyl_P_corrected(k);
            output_B(j-Cycle_no_cut+1,3)=CAD(k);
        end
        % Find maximum dP/dt, looking only from TDC +/- 50 CAD
        % When max dP/dt is found, also record CAD location
        if CAD(k)>=310 && CAD(k)<=410;
            if output_B(j-Cycle_no_cut+1,4)<Dpdt(k);
```

```
                output_B(j-Cycle_no_cut+1,4)=Dpdt(k);
                output_B(j-Cycle_no_cut+1,5)=CAD(k);
            end
        end
        % Find maximum dP/dtheta, looking only from TDC +/- 50 CAD
        % When max dP/dtheta is found, also record CAD location
        if CAD(k)>=310 && CAD(k)<=410;
            if output_B(j-Cycle_no_cut+1,8)<Dpdtheta(k);
                output_B(j-Cycle_no_cut+1,8)=Dpdtheta(k);
                output_B(j-Cycle_no_cut+1,9)=CAD(k);
            end
        end
        % Find maximum dQ/dt, looking only from TDC +/- 100 CAD
        % When max dQ/dt is found, also record CAD location
        if CAD(k)>=260 && CAD(k)<=460;
            if output_B(j-Cycle_no_cut+1,6)<Dqdt(k);
                output_B(j-Cycle_no_cut+1,6)=Dqdt(k);
                output_B(j-Cycle_no_cut+1,7)=CAD(k);
            end
        end
        % Find maximum dQ/dtheta, looking only from TDC +/- 100 CAD
        % When max dQ/dtheta is found, also record CAD location
        if CAD(k)>=260 && CAD(k)<=460;
            if output_B(j-Cycle_no_cut+1,10)<Dqdtheta(k);
                output_B(j-Cycle_no_cut+1,10)=Dqdtheta(k);
                output_B(j-Cycle_no_cut+1,11)=CAD(k);
            end
        end
        % Calculate indicated work [bar * Liter]by integrating cylinder pressure
        Ind_Work=Ind_Work+Cyl_P_corrected(k)*(Cyl_Vol(k+1)-Cyl_Vol(k));
    end
    % Calculate IMEP [bar]
    output_B(j-Cycle_no_cut+1,12)=Ind_Work/Disp_Vol;
end

% Calculate statistics for max P, max dP/dt, max dQ/dt, max dP/dtheta, max dQ/dtheta over entire data set
% also calculate statistics for CAD locations of these paratmeters
for j=2:12;
    output_B(length(Cycle_marker)-Cycle_no_cut+2,j)=mean(output_B(1:length(Cycle_marker)-Cycle_no_cut,j));
    output_B(length(Cycle_marker)-Cycle_no_cut+3,j)=std(output_B(1:length(Cycle_marker)-Cycle_no_cut,j));
    output_B(length(Cycle_marker)-Cycle_no_cut+4,j)=output_B(length(Cycle_marker)-Cycle_no_cut+3,j)...
    .../output_B(length(Cycle_marker)-Cycle_no_cut+2,j);
end


%%%%%%%%%%%%%%%%%%     FIGURE 2
%%%%%%%%%%%%%%%%%%     %%%%%%%%%%%%%%%%%%%%%%%%%%%%%%%%%%%%%%%%%%%%%%%%%%%%
%%%%%%%%%%%%%%%%%%     %%%%%%%%%%%%%%%%%%%%%%%%%%%%%%%%%%%%%%%%%%%%%%%%%%%%

% Plot of corrected cylinder pressure
figure(2)
%subplot(321)
[AX,plot1,plot2] = plotyy(Test_Time,Camera_Trigger,...
                             Test_Time,Cyl_P_corrected,'plot');
%title(inputfilename,'Interpreter','none','fontsize',12,'fontweight','b');
xlabel('Time (ms)');
set(plot1,'Color','white');
set(get(AX(1),'Ylabel'),'String',' ','Color','r');
set(AX(1),'YLim',[-.5 1.5]);
set(AX(1),'YTick',[-10:.5:-11],'Ycolor','r');
set(plot2,'Color','black');
set(get(AX(2),'Ylabel'),'String','Corrected Cylinder Pressure [bar]','Color','black');
set(AX(2),'YLim',[0 50]);
set(AX(2),'YTick',[-10:5:100],'Ycolor','black');
%text(Test_Time(Cycle_marker(Cycle_no_cut)),-.1,['|'],'fontsize',36);
hold on

% Plot of corrected cylinder pressure
%subplot(322)
figure(3)
for k=cycle_pick
    plot(CAD(Cycle_marker(k):(Cycle_marker(k+1)-1)),...
    Cyl_P_corrected(Cycle_marker(k):(Cycle_marker(k+1)-1)),'-','MarkerSize',1,'Color','b')
hold on
end
% for k=Cycle_no_cut:Cycle_no
%     plot(CAD(Cycle_marker(k):(Cycle_marker(k+1)-1)),...
%     Cyl_P_corrected(Cycle_marker(k):(Cycle_marker(k+1)-1)),'-','MarkerSize',1,'Color','r')
% hold on
% end
```

```
%title(inputfilename,'Interpreter','none');
xlabel('CAD');
set(gca,'XLim',[0 720]);
set(gca,'XTick',[0:90:720]);
ylabel('Corrected Cylinder Pressure [bar]');
set(gca,'YLim',[0 50]);
set(gca,'YTick',[-100:5:100]);
% text(45,.90*45,['P_m_a_x A'],'fontsize',8);
% text(45,.80*45,['avg = ',num2str(output_A(Cycle_no_cut+1,2))],'fontsize',8);
% text(45,.70*45,['std = ',num2str(output_A(Cycle_no_cut+2,2))],'fontsize',8);
% text(45,.60*45,['cov = ',num2str(output_A(Cycle_no_cut+3,2))],'fontsize',8);
% text(540,.90*45,['P_m_a_x B'],'fontsize',8);
% text(540,.80*45,['avg = ',num2str(output_B(length(Cycle_marker)-Cycle_no_cut+1,2))],'fontsize',8);
% text(540,.70*45,['std = ',num2str(output_B(length(Cycle_marker)-Cycle_no_cut+2,2))],'fontsize',8);
% text(540,.60*45,['cov = ',num2str(output_B(length(Cycle_marker)-Cycle_no_cut+3,2))],'fontsize',8);
hold on

% Plot of dP/dt
%subplot(323)
figure(4)
for k=1:Cycle_no_cut
    plot(CAD(Cycle_marker(k):(Cycle_marker(k+1)-1)),...
    Dpdt(Cycle_marker(k):(Cycle_marker(k+1)-1)),'-','MarkerSize',1,'Color','b')
hold on
end
for k=Cycle_no_cut:Cycle_no
    plot(CAD(Cycle_marker(k):(Cycle_marker(k+1)-1)),...
    Dpdt(Cycle_marker(k):(Cycle_marker(k+1)-1)),'-','MarkerSize',1,'Color','r')
hold on
end
%title(inputfilename,'Interpreter','none');
xlabel('CAD');
set(gca,'XLim',[315 405]);
set(gca,'XTick',[0:15:720]);
ylabel('dP/dt [bar/sec]');
set(gca,'YLim',[-5e3 25e3]);
set(gca,'ytick',[-5e3:5e3:25e3])
%text(320,.90*25000,['dP/dt A'],'fontsize',8);
%text(320,.80*25000,['avg = ',num2str(output_A(Cycle_no_cut+1,4))],'fontsize',8);
%text(320,.70*25000,['std = ',num2str(output_A(Cycle_no_cut+2,4))],'fontsize',8);
%text(320,.60*25000,['cov = ',num2str(output_A(Cycle_no_cut+3,4))],'fontsize',8);
%text(380,.90*25000,['dP/dt B'],'fontsize',8);
%text(380,.80*25000,['avg = ',num2str(output_B(length(Cycle_marker)-Cycle_no_cut+1,4))],'fontsize',8);
%text(380,.70*25000,['std = ',num2str(output_B(length(Cycle_marker)-Cycle_no_cut+2,4))],'fontsize',8);
%text(380,.60*25000,['cov = ',num2str(output_B(length(Cycle_marker)-Cycle_no_cut+3,4))],'fontsize',8);
hold on

% Plot of dQ/dt
%subplot(324)
figure(5)
for k=1:Cycle_no_cut
    plot(CAD(Cycle_marker(k):(Cycle_marker(k+1)-1)),...
    Dqdt(Cycle_marker(k):(Cycle_marker(k+1)-1)),'-','MarkerSize',1,'Color','b')
hold on
end
for k=Cycle_no_cut:Cycle_no
    plot(CAD(Cycle_marker(k):(Cycle_marker(k+1)-1)),...
    Dqdt(Cycle_marker(k):(Cycle_marker(k+1)-1)),'-','MarkerSize',1,'Color','r')
hold on
end
%title(inputfilename,'Interpreter','none');
xlabel('CAD');
set(gca,'XLim',[315 405]);
set(gca,'XTick',[0:15:720]);
ylabel('dQ/dt [kJ/sec]');
set(gca,'YLim',[-25 175]);
set(gca,'ytick',([-50:25:200]))
text(320,.90*175,['dQ/dt'],'fontsize',8);
text(320,.80*175,['avg = ',num2str(output_A(Cycle_no_cut+1,6))],'fontsize',8);
text(320,.70*175,['std = ',num2str(output_A(Cycle_no_cut+2,6))],'fontsize',8);
text(320,.60*175,['cov = ',num2str(output_A(Cycle_no_cut+3,6))],'fontsize',8);
text(380,.90*175,['dQ/dt B'],'fontsize',8);
text(380,.80*175,['avg = ',num2str(output_B(length(Cycle_marker)-Cycle_no_cut+1,6))],'fontsize',8);
text(380,.70*175,['std = ',num2str(output_B(length(Cycle_marker)-Cycle_no_cut+2,6))],'fontsize',8);
text(380,.60*175,['cov = ',num2str(output_B(length(Cycle_marker)-Cycle_no_cut+3,6))],'fontsize',8);
hold on

% Plot of dP/dtheta
%subplot(325)
figure(6)
```

```
for k=1:Cycle_no_cut
    plot(CAD(Cycle_marker(k):(Cycle_marker(k+1)-1)),...
    Dpdtheta(Cycle_marker(k):(Cycle_marker(k+1)-1)),'-','MarkerSize',1,'Color','b')
hold on
end
for k=Cycle_no_cut:Cycle_no
    plot(CAD(Cycle_marker(k):(Cycle_marker(k+1)-1)),...
    Dpdtheta(Cycle_marker(k):(Cycle_marker(k+1)-1)),'-','MarkerSize',1,'Color','r')
hold on
end
%title(inputfilename,'Interpreter','none');
xlabel('CAD');
set(gca,'XLim',[315 405]);
set(gca,'XTick',[0:15:720]);
ylabel('dP/d\theta [bar/CAD]');
set(gca,'YLim',[-1 5]);
set(gca,'ytick',([-5:1:5]))
text(320,.90*5,['dP/d\theta A'],'fontsize',8);
text(320,.80*5,['avg = ',num2str(output_A(Cycle_no_cut+1,8))],'fontsize',8);
text(320,.70*5,['std = ',num2str(output_A(Cycle_no_cut+2,8))],'fontsize',8);
text(320,.60*5,['cov = ',num2str(output_A(Cycle_no_cut+3,8))],'fontsize',8);
text(380,.90*5,['dP/d\theta B'],'fontsize',8);
text(380,.80*5,['avg = ',num2str(output_B(length(Cycle_marker)-Cycle_no_cut+1,8))],'fontsize',8);
text(380,.70*5,['std = ',num2str(output_B(length(Cycle_marker)-Cycle_no_cut+2,8))],'fontsize',8);
text(380,.60*5,['cov = ',num2str(output_B(length(Cycle_marker)-Cycle_no_cut+3,8))],'fontsize',8);
hold on

% Plot of dQ/dtheta
%subplot(326)
figure(7)
for k=1:Cycle_no_cut
    plot(CAD(Cycle_marker(k):(Cycle_marker(k+1)-1)),...
    Dqdtheta(Cycle_marker(k):(Cycle_marker(k+1)-1)),'-','MarkerSize',1,'Color','b')
hold on
end
for k=Cycle_no_cut:Cycle_no
    plot(CAD(Cycle_marker(k):(Cycle_marker(k+1)-1)),...
    Dqdtheta(Cycle_marker(k):(Cycle_marker(k+1)-1)),'-','MarkerSize',1,'Color','r')
hold on
end
%title(inputfilename,'Interpreter','none');
xlabel('CAD');
set(gca,'XLim',[315 405]);
set(gca,'XTick',[0:15:720]);
ylabel('dQ/d\theta [J/CAD]');
set(gca,'YLim',[-5 40]);
set(gca,'ytick',([-10:5:50]))
text(320,.90*40,['dQ/d\theta'],'fontsize',8);
text(320,.80*40,['avg = ',num2str(output_A(Cycle_no_cut+1,10))],'fontsize',8);
text(320,.70*40,['std = ',num2str(output_A(Cycle_no_cut+2,10))],'fontsize',8);
text(320,.60*40,['cov = ',num2str(output_A(Cycle_no_cut+3,10))],'fontsize',8);
text(380,.90*40,['dQ/d\theta B'],'fontsize',8);
text(380,.80*40,['avg = ',num2str(output_B(length(Cycle_marker)-Cycle_no_cut+1,10))],'fontsize',8);
text(380,.70*40,['std = ',num2str(output_B(length(Cycle_marker)-Cycle_no_cut+2,10))],'fontsize',8);
text(380,.60*40,['cov = ',num2str(output_B(length(Cycle_marker)-Cycle_no_cut+3,10))],'fontsize',8);
hold on

% Plot of corrected cylinder pressure
%subplot(322)
figure(8)
% for k=cycle_pick
%     plot(CAD(Cycle_marker(k):(Cycle_marker(k+1)-1)),...
%     Cyl_P_corrected(Cycle_marker(k):(Cycle_marker(k+1)-1)),'-','MarkerSize',1,'Color','b')
% hold on
% end
for k=Cycle_no_cut:Cycle_no
    plot(CAD(Cycle_marker(k):(Cycle_marker(k+1)-1)),...
    Cyl_P_corrected(Cycle_marker(k):(Cycle_marker(k+1)-1)),'-','MarkerSize',1,'Color','r')
hold on
end
title(inputfilename,'Interpreter','none');
xlabel('CAD');
set(gca,'XLim',[180 540]);
set(gca,'XTick',[180:90:540]);
ylabel('Corrected Cylinder Pressure [bar]');
set(gca,'YLim',[0 50]);
set(gca,'YTick',[-100:5:100]);
text(200,.90*45,['P_m_a_x A'],'fontsize',12);
text(200,.80*45,['avg = ',num2str(output_A(Cycle_no_cut+1,2))],'fontsize',12);
text(200,.70*45,['std = ',num2str(output_A(Cycle_no_cut+2,2))],'fontsize',12);
```

```
text(200,.60*45,['cov = ',num2str(output_A(Cycle_no_cut+3,2))],'fontsize',12);
text(450,.90*45,['P_m_a_x B'],'fontsize',12);
text(450,.80*45,['avg = ',num2str(output_B(length(Cycle_marker)-Cycle_no_cut+2,2))],'fontsize',12);
text(450,.70*45,['std = ',num2str(output_B(length(Cycle_marker)-Cycle_no_cut+3,2))],'fontsize',12);
text(450,.60*45,['cov = ',num2str(output_B(length(Cycle_marker)-Cycle_no_cut+4,2))],'fontsize',12);
hold off
```

D.2 MATLAB code for calculating $\gamma_u = \frac{c_{p,u}}{c_{v,u}}$ as f(T, ϕ)

```
% File name:  gammacalc_Brad_2008_05_03.m
% This program calculates gamma for a fuel/air mixture over a range of
% temperatures
% Adapted by Bradley T. Zigler, bzigler@umich.edu, from a code written for
% Rapid Compression Facility calculations by Xin He and Stephen Walton
% Last update by Brad Zigler, 3 May 2008
%
clear all;
clear;
clc
global Molar_isooctane Molar_O2 Molar_Ar Molar_N2 Molar_CO2...
       Molar_H2O Molar_CO Molar_C2H2 Molar_H2 Molar_nheptane...
       Molar_CH4 Molar_C2H4 Molar_CH3OH Molar_mb Molar_nbmeth...
       Molar_Gas1 Molar_Gas2

%three eqs here
k = 0;
for Temp = 26.85:10:726.85  %Temperature in Celsius
k = k+1;

i = 0;
for Phi = 0:.05:1
i = i+1;


total = 1;
%%%%%%%%% Input mixture properties here %%%%%%%%%%%%%%%%%%%%%%%%%%%%%%%%%%
i_mix   =   0.0;
iC8H18  =   Phi;
Gas1    =   0;
Gas2    =   0;
nC7H16  =   0;
C2H4    =   0;
C2H2    =   0;
CH4     =   0;
CH3OH   =   0;
mb      =   0;
nbmeth  =   0;
H2      =   0;
CO      =   0;
O2      =   12.5;       %Adjust this for equation balance (A/F(stoich)) for fuel used
N2      =   12.5*3.76;  %Adjust this for equation balance (A/F(stoich)) for fuel used
Ar      =   0;
CO2     =   0;
H2O     =   0;
%%%%% Input all experiment properties here %%%%%%%%%%%%%%%%%%%%%%%%%%%%%%
initial_fine   =  0.0;             %initial pressure (torr)
initial_coarse =  0.0;             %initial pressure (torr)
%%%%%%   Find Temperature after compression      %%%%%%%%%%%%%%%%%%%%%%%%%%
all=iC8H18+CO2+CO+Ar+H2O+O2+N2+C2H2+H2+nC7H16+CH4+C2H4+CH3OH+mb+nbmeth+Gas1+Gas2;
scale=1;
T0=273.15+Temp;
Molar_N2        =  (N2     /all*(total-initial_coarse)+initial_fine*0.79)/total*scale;
Molar_O2        =  (O2     /all*(total-initial_coarse)+initial_fine*0.21)/total*scale;
Molar_isooctane =  iC8H18  /all*(total-initial_coarse)/total*scale;
Molar_CO2       =  CO2     /all*(total-initial_coarse)/total*scale;
Molar_Ar        =  Ar      /all*(total-initial_coarse)/total*scale;
Molar_H2O       =  H2O     /all*(total-initial_coarse)/total*scale;
Molar_CO        =  CO      /all*(total-initial_coarse)/total*scale;
Molar_C2H2      =  C2H2    /all*(total-initial_coarse)/total*scale;
Molar_H2        =  H2      /all*(total-initial_coarse)/total*scale;
Molar_nheptane  =  nC7H16  /all*(total-initial_coarse)/total*scale;
Molar_CH4       =  CH4     /all*(total-initial_coarse)/total*scale;
Molar_C2H4      =  C2H4    /all*(total-initial_coarse)/total*scale;
```

```
Molar_CH3OH     =  CH3OH   /all*(total-initial_coarse)/total*scale;
Molar_mb        =  mb      /all*(total-initial_coarse)/total*scale;
Molar_nbmeth    =  nbmeth  /all*(total-initial_coarse)/total*scale;
Molar_Gas1      =  Gas1    /all*(total-initial_coarse)/total*scale;
Molar_Gas2      =  Gas2    /all*(total-initial_coarse)/total*scale;

P0=total*0.133322/6.894757;           %initial pressure (torr)

T=T0;
T_out(k) = T;
Phi_out(i) = Phi;
[gamma(k,i)]=gamma_all_Brad(T, Molar_isooctane, Molar_Ar, Molar_N2,...
                       Molar_O2, Molar_CO2, Molar_H2O, Molar_CO,...
                       Molar_C2H2, Molar_H2, Molar_nheptane,...
                       Molar_CH4, Molar_C2H4, Molar_CH3OH, Molar_mb,...
                       Molar_nbmeth, Molar_Gas1, Molar_Gas2);

end
end

[size1 size2] = size(gamma);
for j = 1:size2
figure(1)
hold on
plot(T_out(1,:),gamma(:,j))
end
hold off

%figure(2)
%plot(Phi_out,gamma(31,:))

%%%%%%%%%%%% Solving for T_eff_1 using P_eff_1 %%%%%%%%%%%%%%%%%%
% P_eff_1=P_eff_1_atm/.068046;
% P_old=P0;
% P_new=P0;
% x=0.001;
% i=1;
% T=T0;
% while (P_old<P_eff_1)&(P_new<P_eff_1)
%     P_old=P_new;
%     [gamma]=gamma_all_8(T, Molar_isooctane, Molar_Ar, Molar_N2,...
%                       Molar_O2, Molar_CO2, Molar_H2O, Molar_CO,...
%                       Molar_C2H2, Molar_H2, Molar_nheptane,...
%                       Molar_CH4, Molar_C2H4, Molar_CH3OH, Molar_mb,...
%                       Molar_nbmeth);
%     T=T*((i+x)/i)^(gamma-1);
%     P_new=P_old*((i+x)/i)^gamma;
%     i=i+x;
% end
% i=i-x;
% CR1=i+x;
% T_eff_1=T;
```

D.3 MATLAB subroutine for calculating $\gamma_u = \frac{c_{p,u}}{c_{v,u}}$

The following MATLAB code utilizes data from the NASA Thermodynamic Database [40]

```
function [gamma]=gamma_all_Brad(T, Molar_isooctane, Molar_Ar, Molar_N2,...
                      Molar_O2, Molar_CO2, Molar_H2O, Molar_CO,...
                      Molar_C2H2, Molar_H2, Molar_nheptane,...
                      Molar_CH4, Molar_C2H4, Molar_CH3OH, Molar_mb,...
                      Molar_nbmeth, Molar_Gas1, Molar_Gas2)

%%%%%%%%%%%% This is the Thermo Data from the JANNAF tables %%%%%%%%%%%%%%%
%%%%%%%%%%%%%%%%%%%%%%%%%%%%%%%%%%%%%%%%%%%%%%%%%%%%%%%%%%%%%%%%%%%%%%%%%%%%
%%%%%%%%%%%% Values of polynomials results in tables below are [Cp/R]
%%%%%%%%%%%% for each species %%%%%%%%%%%%
if(T>1000)
isooctane =  1.59899273E+1   +5.53184790E-2  *T  -1.95267072E-5  *T^2  +3.11779172E-9   *T^3  -1.85312577E-13  *T^4;
N2        =  2.95257626      +1.39690057E-3  *T  -4.92631691E-7  *T^2  +7.86010367E-11  *T^3  -4.60755321E-15  *T^4;
O2        =  3.66096083      +6.56365523E-4  *T  -1.41149485E-7  *T^2  +2.05797658E-11  *T^3  -1.29913248E-15  *T^4;
CO2       =  4.63659493      +2.74131991E-3  *T  -9.95828531E-7  *T^2  +1.60373011E-10  *T^3  -9.16103468E-15  *T^4;
H2O       =  2.67703787      +2.97318329E-3  *T  -7.73769690E-7  *T^2  +9.44336689E-11  *T^3  -4.26900959E-15  *T^4;
CO        =  3.04848583      +1.35172818E-3  *T  -4.85794075E-7  *T^2  +7.88536486E-11  *T^3  -4.69807489E-15  *T^4;
CH4       =  1.63552643      +1.00842795e-2  *T  -3.36916254e-6  *T^2  +5.34958667e-10  *T^3  -3.15518833e-14  *T^4;
C2H4      =  3.99182761E+00  +1.04833910E-02 *T  -3.71721385E-06 *T^2  +5.94628514E-10  *T^3  -3.53630526E-14  *T^4;
```

```
nheptane  =  2.22148969e+01  +3.47675750e-02 *T  -1.18407129e-05 *T^2  +1.83298478e-09  *T^3  -1.06130266e-13  *T^4;
CH3OH     =  0.04029061e+02  +0.09376593e-01 *T  -0.03050254e-04 *T^2  +0.04358793e-08  *T^3  -0.02224723e-12  *T^4;
mb        =  1.90094725e+01  +2.36503722e-02 *T  -8.22978452e-06 *T^2  +1.29246265e-09  *T^3  -7.55862836e-14  *T^4;
nbmeth    =  1.95422034e+01  +2.33601261e-02 *T  -8.16729241e-06 *T^2  +1.28676535e-09  *T^3  -7.54230804e-14  *T^4;
nbmeth    =  1.44556474e+00  +6.07605168e-02 *T  -3.65779067e-05 *T^2  +1.07102077e-08  *T^3  -1.22703399e-12  *T^4;
%Heywood source for Gasoline properties, polynomial given in
%[cal/gmol-K], which is converted below by front factor to [J/gmol-K]
Gas1 = (1/0.2388) * (-24.078 + 256.63*(T/1000) -201.68*(T/1000)^2 + 64.750*(T/1000)^3 + 0.5808/((T/1000)^2));
Gas2 = (1/0.2388) * (-22.501 + 227.99*(T/1000) -177.26*(T/1000)^2 + 56.048*(T/1000)^3 + 0.4845/((T/1000)^2));
else
isooctane =  8.15737338E-1   +7.32643959E-2  *T  +1.78300688E-5  *T^2  -6.93589620E-8   *T^3  +3.21629382E-11  *T^4;
%Heywood cp polynomial follows, but this polynomial is in [cal/mol-K],
%and needs to be compensated
%isooctane =  -0.55313        +181.62  *(T/1000)  -97.787  *(T/1000)^2  +20.402   *(T/1000)^3  -0.03095/((T/1000)^2);
N2        =  3.53100528      -1.23660987E-4  *T  -5.02999437E-7  *T^2  +2.43530612E-09  *T^3  -1.40881235E-12  *T^4;
O2        =  3.78245636      -2.99673415E-3  *T  +9.84730200E-6  *T^2  -9.68129508E-09  *T^3  +3.24372836E-12  *T^4;
CO2       =  2.35677352      +8.98459677E-3  *T  -7.12356269E-6  *T^2  +2.45919022E-09  *T^3  -1.43699548E-13  *T^4;
H2O       =  4.19864056      -2.03643410E-3  *T  +6.52040211E-6  *T^2  -5.48797062E-09  *T^3  +1.77197817E-12  *T^4;
CO        =  3.57953347      -6.10353680E-4  *T  +1.01681433E-6  *T^2  +9.07005884E-10  *T^3  -9.04424499E-13  *T^4;
CH4       =  5.14987613      -1.36709788e-2  *T  +4.91800599e-5  *T^2  -4.84743026e-8   *T^3  +1.66693956e-11  *T^4;
C2H4      =  3.95920148E+00  -7.57052247E-03 *T  +5.70990292E-05 *T^2  -6.91588753E-08  *T^3  +2.69884373E-11  *T^4;
nheptane  = -1.26836187e+00  +8.54355820e-02 *T  -5.25346786e-05 *T^2  +1.62945721e-08  *T^3  -2.02394925e-12  *T^4;
CH3OH     =  0.02660115e+02  +0.07341508e-01 *T  -0.07170051e-04 *T^2  -0.08793194e-07  *T^3  -0.02390570e-10  *T^4;
mb        =  3.16208825e+00  +5.52915358e-02 *T  -3.11610102e-05 *T^2  +8.42394129e-09  *T^3  -8.72222021e-13  *T^4;
nbmeth    =  1.44556474e+00  +6.07605168e-02 *T  -3.65779067e-05 *T^2  +1.07102077e-08  *T^3  -1.22703399e-12  *T^4;
%Heywood source for Gasoline properties, polynomial given in
%[cal/gmol-K], which is converted below by front factor to [J/gmol-K]
Gas1 = (1/0.2388) * (-24.078 + 256.63*(T/1000) -201.68*(T/1000)^2 + 64.750*(T/1000)^3 + 0.5808/((T/1000)^2));
Gas2 = (1/0.2388) * (-22.501 + 227.99*(T/1000) -177.26*(T/1000)^2 + 56.048*(T/1000)^3 + 0.4845/((T/1000)^2));
end
%%%%%%%%%%%%%%%%%%%%%%%%%%%%%%%%%%%%%%%%%%%%%%%%%%%%%%%%%%%%%%%%%%%%%%%%%%%
%Universal gas constant
R=8.31451;          %J/(mol-K)
Ar=2.5;

%%%%%%%%% Remember when adding species to add them here as well %%%%%%%%%%%
%%%%%%%%% as in the function call and the thermo data           %%%%%%%%%%%
Cp=(   isooctane  *  Molar_isooctane            +...
       N2         *  Molar_N2                   +...
       O2         *  Molar_O2                   +...
       Ar         *  Molar_Ar                   +...
       CO2        *  Molar_CO2                  +...
       H2O        *  Molar_H2O                  +...
       CO         *  Molar_CO                   +...
       nheptane   *  Molar_nheptane             +...
       CH4        *  Molar_CH4                  +...
       C2H4       *  Molar_C2H4                 +...
       CH3OH      *  Molar_CH3OH                +...
       mb         *  Molar_mb                   +...
       nbmeth     *  Molar_nbmeth               +...
    0)*R;

Cp=Cp+ Gas1      *  Molar_Gas1                 +...
       Gas2      *  Molar_Gas2                 ;
%%%%%%%%%%%%%%%%%%%%%%%%%%%%%%%%%%%%%%%%%%%%%%%%%%%%%%%%%%%%%%%%%%%%%%%%%%%
Cv=Cp-R;
gamma=Cp/Cv;
```

D.4 MATLAB code for calculating isentropic end of compression temperature

```
% File name:  Ziger_2008_05_03.m
% This program calculates End of Compression temperature and actual CR
% for engine data, given intake and EOC pressures, and sweeping intake
% charge temperature and equivalence ratio
% Adapted by Bradley T. Zigler, bzigler@umich.edu, from a code written for
% Rapid Compression Facility calculations by Xin He and Stephen Walton
% Last update by Brad Zigler, 3 May 2008
%
clear all;
clear;
clc
global Molar_isooctane Molar_O2 Molar_Ar Molar_N2 Molar_CO2...
       Molar_H2O Molar_CO Molar_C2H2 Molar_H2 Molar_nheptane...
       Molar_CH4 Molar_C2H4 Molar_CH3OH Molar_mb Molar_nbmeth...
```

```
       Molar_Gas1 Molar_Gas2

%three eqs here
k = 0;
for Temp = 100:20:300  %Temperature in Celsius
k = k+1;

z = 0;
for Phi = 0:.1:1
z = z+1;

%%%%%%   Input data here %%%%%%%%%%%%%%%%%%%%%%%%%%%%%%%%%%%%%%%%%%%%%%%%%%
% Temp = 320;         % Intake temperature in Celsius
P_intake  = 0.99;     % Pressure in cyl at BDC with open intake valve in bar
P_EOC_bar = 19;     % Pressure at end of of compression (or other time of interest) in bar
%%%%%%%%%%%%%%%%%%%%%%%%%%%%%%%%%%%%%%%%%%%%%%%%%%%%%%%%%%%%%%%%%%%%%%%%%%%
P_eff_1_atm= P_EOC_bar/1.01325;  % Pressure in cyl at EOC (or other time of interest)

%%%%%%%%% Input mixture properties here %%%%%%%%%%%%%%%%%%%%%%%%%%%%%%%%%%%
i_mix   =   0.0;
iC8H18  =   0;
Gas1    =   0;
Gas2    =   Phi;
nC7H16  =   0;
C2H4    =   0;
C2H2    =   0;
CH4     =   0;
CH3OH   =   0;
mb      =   0;
nbmeth  =   0;
H2      =   0;
CO      =   0;
O2      =   11.035;       % Adjust this for A/F(stoich) for fuel used
N2      =   11.035*3.76;  % Adjust this for A/F(stoich) for fuel used
Ar      =   0;
CO2     =   0;
H2O     =   0;

all=iC8H18+CO2+CO+Ar+H2O+O2+N2+C2H2+H2+nC7H16+CH4+C2H4+CH3OH+mb+nbmeth+Gas1+Gas2;

T0=273.15+Temp;

Molar_N2        =  N2      /all;
Molar_O2        =  O2      /all;
Molar_isooctane =  iC8H18  /all;
Molar_CO2       =  CO2     /all;
Molar_Ar        =  Ar      /all;
Molar_H2O       =  H2O     /all;
Molar_CO        =  CO      /all;
Molar_C2H2      =  C2H2    /all;
Molar_H2        =  H2      /all;
Molar_nheptane  =  nC7H16  /all;
Molar_CH4       =  CH4     /all;
Molar_C2H4      =  C2H4    /all;
Molar_CH3OH     =  CH3OH   /all;
Molar_mb        =  mb      /all;
Molar_nbmeth    =  nbmeth  /all;
Molar_Gas1      =  Gas1    /all;
Molar_Gas2      =  Gas2    /all;


%P0=total*0.133322/6.894757;           %initial pressure (torr)

P0= P_intake*14.5037738;  % Converts pressure from bar to psi

% T=T0;
% T_out(k) = T;
% Phi_out(z) = Phi;
% [gamma(k,z)]=gamma_all_Brad(T, Molar_isooctane, Molar_Ar, Molar_N2,...
%                        Molar_O2, Molar_CO2, Molar_H2O, Molar_CO,...
%                        Molar_C2H2, Molar_H2, Molar_nheptane,...
%                        Molar_CH4, Molar_C2H4, Molar_CH3OH, Molar_mb,...
%                        Molar_nbmeth, Molar_Gas1, Molar_Gas2);

%%%%%%%%%% Solving for T_eff_1 using P_eff_1 %%%%%%%%%%%%%%%%%%
P_eff_1=P_eff_1_atm/.068046;
P_old=P0;
P_new=P0;
x=0.001;
i=1;
```

```
T=T0;
while (P_old<P_eff_1)&(P_new<P_eff_1)
    P_old=P_new;
    [gamma]=gamma_all_Brad(T, Molar_isooctane, Molar_Ar, Molar_N2,...
                       Molar_O2, Molar_CO2, Molar_H2O, Molar_CO,...
                       Molar_C2H2, Molar_H2, Molar_nheptane,...
                       Molar_CH4, Molar_C2H4, Molar_CH3OH, Molar_mb,...
                       Molar_nbmeth, Molar_Gas1, Molar_Gas2);
    T=T*((i+x)/i)^(gamma-1);
    P_new=P_old*((i+x)/i)^gamma;
    i=i+x;
end
i=i-x;
[CR1(k,z)]=i+x;
T_eff_1=T;
[T_EOC(k,z)]=T_eff_1;

end
end


% [size1 size2] = size(gamma);
% for j = 1:size2
% figure(1)
% hold on
% plot(T_out(1,:),gamma(:,j))
% end
% hold off
```

BIBLIOGRAPHY

BIBLIOGRAPHY

[1] Vision Research, I. Spectral and Color Responses for Phantom Cameras, Revision 1.0.0 (2004).

[2] Zigler, B. T., Walton, S. M., He, X., Wiswall, J. T., Wooldridge, M. S. & Wooldridge, S. T. Crank-Angle Resolved Imaging of Homogeneous Charge Compression Ignition Phenomena in a Single-Cylinder Research Engine. *Proceedings of the 2006 Technical Meeting of the Central States Section of The Combustion Institute* (2006).

[3] Santoso, H., Matthews, J. & Cheng, W. Managing SI/HCCI Dual-Mode Engine Operation. *SAE* **2005-01-0162** (2005).

[4] Zhao, H., Li, J., Ma, T. & Ladommatos, N. Performance and Analysis of a 4-Stroke Multi-Cylinder Gasoline Engine with CAI Combustion. *SAE* **2002-01-0420** (2002).

[5] Epping, K., Aceves, S., Bechtold, R. & Dec, J. The potential of HCCI combustion for high efficiency and low emissions. *SAE* **2002-01-1923** (2002).

[6] Christensen, M., Einewall, P. & Johansson, B. Homogeneous charge compression ignition (HCCI) using iso-octane, ethanol and natural gas - a comparison to spark ignition operation. *SAE* **972874** (1997).

[7] He, X., Zigler, B. T., Walton, S. M., Wooldridge, M. S. & Atreya, A. A rapid compression facility study of OH time histories during iso-octane ignition. *Combustion and Flame* **145**, 552–570 (2006).

[8] Walton, S. M., He, X., Zigler, B. T., Wooldridge, M. S. & Atreya, A. An experimental investigation of iso-octane ignition phenomena. *Combustion and Flame* **150**, 246–262 (2007).

[9] Walton, S. M., He, X., Donovan, M. T., Zigler, B. T., Palmer, T. R., Wooldridge, M. S. & Atreya, A. High-speed digital imaging of iso-octane mixtures at homogeneous charge compression ignition operating conditions. In *The Central States Meeting of The Combustion Institute* (2004).

[10] Walton, S. M., He, X., Zigler, B. T., Wooldridge, M. S. & Atreya, A. Demonstration of distinct imaging regimes using high-speed digital imaging of iso-octane mixtures. In *Proceedings of the Fourth Joint Meeting of the U.S. Sections of The Combustion Institute* (2005).

[11] Kaiser, E., Maricq, M., Xu, N. & Yang, J. Detailed hydrocarbon species and particulate emissions from a HCCI engine as a function of air-fuel ratio. *SAE* **2005-01-3749** (2005).

[12] Kaiser, E., Yang, J., Culp, T., Xu, N. & Maricq, M. Homogeneous charge compression ignition engine-out emission-does flame propagation occur in homogeneous charge compression ignition? *International Journal of Engine Research* **3**, 185–195 (2002).

[13] Weinrotter, M. *et al.* Optical diagnostics of laser-induced and spark plug-assisted HCCI combustion. *SAE* **2005-01-0129** (2005).

[14] Hyvonen, J., Haraldsson, G. & Johansson, B. Operating conditions using spark assisted HCCI combustion during combustion mode transfer to SI in a multi-cylinder VCR-HCCI engine. *SAE* **2005-01-0109** (2005).

[15] Berntsson, A. & Denbratt, I. Spark assisted HCCI combustion using a stratified hydrogen charge. *SAE* **2005-24-039** (2005).

[16] Wang, Z., Wang, J. X., Shuai, S. J. & Ma, Q. J. Effects of spark ignition and stratified charge on gasoline HCCI combustion with direct injection. *SAE* **2005-01-0137** (2005).

[17] Wagner, R., Edwards, K., Daw, C., Green, J. & Bunting, B. On the nature of cyclic dispersion in spark assisted HCCI combustion. *SAE* **2006-01-0418** (2006).

[18] Natarajan, V. K. *Spark-assisted compression ignition: an experimental investigation into how spark ignition advances combustion phasing in gasoline HCCI engines.* Ph.D. thesis, University of Michigan (2006).

[19] Agrell, F., Angstrom, H. E., Eriksson, B., Wikander, J. & Linderyd, J. Transient control of HCCI-combustion by aid of variable valve timing through the use of an engine state corrected CA50-controller combined with an in-cylinder state estimator estimating lambda. *SAE* **2005-01-2128** (2005).

[20] Haraldsson, G., Hyvonen, J., Tunestal, P. & Johansson, B. HCCI combustion phasing with closed-loop combustion control using variable compression ratio in a multi-cylinder engine. *SAE* **2003-01-1830** (2003).

[21] Christensen, M., Hultqvist, J. & Johansson, B. Demonstrating the multi-fuel capability of a homogeneous charge compression ignition engine with variable compression ratio. *SAE* **1999-01-3679** (1999).

[22] Yoshizawa, K., Teraji, A., Miyakubo, H., Yamaguchi, K. & Urushihara, T. Study of high load operation limit expansion for gasoline compression ignition engines. *ASME Journal of Engineering for Gas Turbines and Power* **128**, 377 (2006).

[23] Sunnaborg, D. Design specifications summary for the Sandia National Laboratories optical engine. *Sandia National Laboratories* (1997).

[24] Gaydon, A. *The Spectroscopy of Flames* (Chapman and Hall, 1957).

[25] Pearse, R. W. B. & Gaydon, A. G. *The Identificaiton of Molecular Spectra* (John Wiley and Sons, 1950).

[26] Yoshida, A., Narisawa, M., Tsuji, H. & Hirose, T. Chemiluminesence emission of C2, CH and OH radicals from opposed jet burner flames. *JSME Int.J.* **38**, 222–229 (1995).

[27] Walsh, K. T., Long, M. B., Tanoff, M. A. & Smooke, M. D. Experimental and computational study of CH, CH*, and OH* in an axisymmetric laminar diffusion flame. *Symposium (International) on Combustion* **1**, 615–623 (1998).

[28] Brunt, M. F. J. & Pond, C. R. Evaluation of Techniques for Absolute Cylinder Pressure Correction. *SAE* **970036** (1997).

[29] Randolph, A. L. Methods of Processing Cylinder-Pressure Transducer Signals to Maximize Data Accuracy. *SAE* **900170** (1990).

[30] Zigler, B. T., Walton, S. M., Assanis, D., Perez, E., Wooldridge, M. S. & Wooldridge, S. T. An imaging study of compression ignition phenomena of iso-octane, indolene, and gasoline fuels in a single-cylinder research engine. *ASME Journal of Engineering for Gas Turbines and Power* **130** (2008).

[31] Heywood, J. *Internal Combustion Engine Fundamentals* (McGraw-Hill, 1988).

[32] United States Government Printing Office Code of Federal Regulations, Title 40. *Part 86 - Control of Emissions from New and In-Use Highway Vehicles and Engines* **16**, 312–314 (2002).

[33] He, X., Donovan, M. T., Zigler, B. T., Palmer, T. R., Walton, S. M., Wooldridge, M. S. & Atreya, A. An experimental and modeling study of iso-octane ignition delay times under homogeneous charge compression ignition conditions. *Combustion and Flame* **142**, 266–275 (2005).

[34] Hultqvist, A., Christensen, M., Johansson, B., Franke, A., Richter, M. & Alden, M. A study of the Homogeneous Charge Compression Ignition Combustion Process by Chemiluminescence Imaging. *SAE* **1999-01-3680** (1999).

[35] Persson, H., Hildingsson, L., Hultqvist, A., Johansson, B. & Ruebel, J. Investigation of Boundary Layer Behaviour in HCCI Combustion Using Chemiluminescence Imaging. *SAE* **2005-01-3729** (2005).

[36] Bunting, B. Combustion, control, and fuel effects in a spark assisted HCCI engine equipped with variable valve timing. *SAE* **2006-01-0872** (2006).

[37] Zigler, B. T., Walton, S. M., Assanis, D., Perez, E. & Wooldridge, M. S. Crank-angle resolved imaging of HCCI phenomena in a single-cylinder research engine (2006). The Combustion Institute 31st International Symposium on Combustion - Poster Session.

[38] Zigler, Z. T., Walton, S. M., Karwat, D. M., Assanis, D., Wooldridge, M. S. & Wooldridge, S. T. A multi-axis imaging study of spark-assisted homogeneous charge compression ignition phenomena in a single-cylinder research engine. *Proceedings of the 2007 Fall Technical Conference of the ASME Internal Combusiton Engine Division* 395 (2008).

[39] Zigler, B. T., Walton, S. M., Assanis, D., Perez, E., Wooldridge, M. S. & Wooldridge, S. T. A comparison of imaging of compression igntion phenomena of Iso-octane, indolene, and gasoline fuels in a single-cylinder research engine. *ASME Internal Combustion Engine Division 2006 Fall Technical Conference* **2006**, 17 (2006).

[40] McBride, B., Gordon, S. & Reno, M. NASA Thermodynamic Database. NASA Technical Memorandum, NASA (1993).